



저작자표시-비영리-변경금지 2.0 대한민국

이용자는 아래의 조건을 따르는 경우에 한하여 자유롭게

- 이 저작물을 복제, 배포, 전송, 전시, 공연 및 방송할 수 있습니다.

다음과 같은 조건을 따라야 합니다:



저작자표시. 귀하는 원저작자를 표시하여야 합니다.



비영리. 귀하는 이 저작물을 영리 목적으로 이용할 수 없습니다.



변경금지. 귀하는 이 저작물을 개작, 변형 또는 가공할 수 없습니다.

- 귀하는, 이 저작물의 재이용이나 배포의 경우, 이 저작물에 적용된 이용허락조건을 명확하게 나타내어야 합니다.
- 저작권자로부터 별도의 허가를 받으면 이러한 조건들은 적용되지 않습니다.

저작권법에 따른 이용자의 권리는 위의 내용에 의하여 영향을 받지 않습니다.

이것은 [이용허락규약\(Legal Code\)](#)을 이해하기 쉽게 요약한 것입니다.

[Disclaimer](#)

이학박사 학위논문

**Hexagonal boron nitride based hybrid
nanomaterials for flexible electronic and
optoelectronic devices**

육방정 질화붕소 기반의 하이브리드 나노소재 및
이를 이용한 유연한 전자소자 및 광전소자 응용

2018 년 8 월

서울대학교 대학원

물리천문학부

오 흥 석

Doctoral thesis

**Hexagonal boron nitride based hybrid
nanomaterials for flexible electronic and
optoelectronic devices**

August 2018

Hongseok Oh

Department of Physics and Astronomy,

Seoul National University

Hexagonal boron nitride based hybrid
nanomaterials for flexible electronic and
optoelectronic devices

육방정 질화붕소 기반의 하이브리드 나노소재 및
이를 이용한 유연한 전자소자 및 광전소자 응용

지도교수 이 규 철

이 논문을 이학박사학위논문으로 제출함

2018년 7월

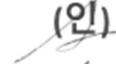
서울대학교 대학원

물리·천문학부

오 홍 석

오홍석의 박사학위논문을 인준함

2018년 7월

위	원	장	이	탁	희	(인) 	
부	위	원	장	이	규	철	(인) 
위		원	홍	승	훈	(인) 	
위		원	김	기	훈	(인) 	
위		원	홍	영	준	(인) 	

Abstract

Hexagonal boron nitride based hybrid nanomaterials for flexible electronic and optoelectronic devices

Hongseok Oh

Department of Physics and Astronomy

Seoul National University

Hexagonal boron nitride (h-BN) is an attractive insulating two-dimensional (2D) nanomaterial with excellent physical properties such as high thermal conductivity, high mechanical strength, and great thermal/chemical stability. Recently, 2D nanomaterial-based hybrid material system are receiving a lot of interests for fabricating next-generation electronic and optoelectronic devices with additional functionalities such as flexibility or transferability. However, the lack of insulating properties in the 2D nanomaterial have raised multiple issues, requiring sophisticated device structures. Consequently, h-BN can be an ideal platform for the novel hybrid material system, when integrated with conventional semiconductor nano/microstructures. Nevertheless, the h-BN based hybrid nanomaterial system has not yet been investigated in detail. In this dissertation, systematic studies on the growth, characterization and device applications of hybrid nanomaterials based on

h-BN are discussed.

Large-scale, epitaxial h-BN few-layer films was synthesized on Ni(111) single crystal substrates using atmospheric pressure chemical vapor deposition (APCVD) with ammonia-borane single precursor. The grown films were transferred to arbitrary substrates via an electrochemical delamination technique, and the remaining Ni(111) substrates were repeatedly re-used. Various physical characterizations confirmed that the grown films exhibited typical characteristics of hexagonal boron nitride layers over the entire area. Furthermore, the heteroepitaxial relationship between h-BN and Ni(111), as well as the overall crystallinity of the film have been thoroughly investigated using synchrotron radiation x-ray diffraction (SR-XRD) analysis and transmission electron microscopy (TEM) based techniques.

Next, the mechanism and the microstructural properties of heteroepitaxial growth on h-BN layers have been thoroughly studied. First, the heteroepitaxy of zinc oxide (ZnO) nanostructures on h-BN was investigated. The van der Waals (vdW) surface feature of the h-BN, due to free of dangling bonds, typically results in low density random nucleation–growth in the epitaxy. The difficulty in control of nucleation sites was resolved by artificially formed atomic ledges prepared on h-BN substrates, which promoted preferential vdW nucleation–growth of ZnO specifically along the designed ledges. Electron microscopy revealed crystallographically domain-aligned incommensurate vdW heteroepitaxial

relationships, even though the ZnO/h-BN is highly lattice mismatched. The first-principles theoretical calculations exhibited the weakly bound, noncovalent binding feature of ZnO/h-BN heterostructure. Furthermore, shape- and morphology-controlled epitaxy of ZnO nanostructures on h-BN was demonstrated. The study was then extended to the ZnO nanostructures on large-scale epitaxial h-BN layers. Large-scale ZnO nanostructure grown on the epitaxial h-BN exhibited similar properties to the ZnO on mechanically exfoliated h-BN, an ordered orientation over long-range.

In addition to the nanostructures, structural properties of gallium nitride (GaN) thin-films grown on h-BN was investigated as well. The heteroepitaxial relationship between GaN and h-BN lead to the growth of single crystalline GaN thin-films over the entire area. Especially, the defect structure was analyzed by two-beam dark field (DF) imaging. Screw-type dislocations was dominantly observed, different to the GaN thin-films on the conventional substrates. The density of the threading dislocations was found to be comparable to those of other GaN thin-films grown on 2D nanomaterials or Si(111) substrates.

The functional device application of the h-BN was demonstrated by fabrication of the flexible ultra violet (UV) sensor. The photocurrent of the ZnO nanostructures on h-BN was first studied on the mechanically exfoliated h-BN. The flexible UV sensor was then fabricated using the large-scale ZnO/h-BN heterostructures patterned as a microdisk array, followed by the mechanical transfer

onto flexible substrates thanks to the weak interlayer bonding of h-BN. The fabricated flexible UV sensors exhibited excellent performance such as a low dark current, a high on-off ratio and short response/recovery times, even under highly bent conditions.

Finally, bottom-up integration of a 2D based hybrid semiconductor nanostructure for flexible electronics was investigated. Here ZnO nanotubes on graphene film was used to fabricate the vertical field-effect transistors (VFET). It should be noted that the study can be readily integrated with the h-BN layers. Due to the high quality of the single crystal ZnO nanotubes and the unique one-dimensional (1D) device structure, the fabricated VFET exhibited excellent electrical characteristics. For example, it had a small subthreshold swing of 110 mV/dec, a high I_{\max}/I_{\min} ratio of 10^6 and a transconductance of 170 nS/ μm . The electrical characteristics of the nanotube VFETs were validated using three-dimensional transport simulations. Furthermore, the nanotube VFETs fabricated on graphene films could be easily transferred onto flexible plastic substrates. The resulting components were reliable, exhibited high performance, and did not degrade significantly during testing.

Key-words: hexagonal boron nitride; nanostructure; flexible; optoelectronics; electronics

Student number: 2011-20409

Table of Contents

ABSTRACT	I
LIST OF FIGURES	X
LIST OF TABLES	XX
1. INTRODUCTION	1
1.1. Motivation: Potentials of hexagonal boron nitride (h-BN) based hybrid nanomaterials for flexible and wearable device applications	1
1.2. Objective and approach	4
1.3. Outline	7
2. LITERATURE REVIEW	9
2.1. Growths of large scale, single crystalline h-BN layers and related materials	9
2.2. Growths of inorganic nanostructures/thin films on h-BN layers or related materials.....	15
2.2.1. Growth of semiconductor nanostructures on graphene layers	15
2.2.2. Growth of inorganic materials on h-BN layers.....	21
2.2.3. Functional optoelectronic devices using 1D-2D hybrid nanomaterials	25
3. EXPERIMENTAL METHODS.....	29
3.1. Chemical vapor deposition (CVD)	29

3.1.1. CVD growth of large-scale h-BN layers.....	29
3.1.2 Cold-wall CVD growth of h-BN	32
3.1.3. Growth of CVD large-scale graphene layers	34
3.2. Metal-organic vapor-phase epitaxy (MOVPE)	34
3.2.1. MOVPE growth of ZnO nanostructure	34
3.3. Transmission electron microscopy (TEM).....	37
3.4. X-ray diffraction (XRD) study.....	37
3.4.1 XRD study for the characterization of thin films	37
3.4.2 Synchrotron radiation XRD analysis.....	37
3.5. Fabrications of nano- and micro-devices.....	40
3.5.1. Fabrication of vertical field-effect transistor using ZnO nanotubes.....	40
3.5.2. Fabrication of flexible UV sensors using ZnO/h-BN hybrid materials.....	44
3.6. Electrical characterizations	47
3.7. DFT calculation.....	47
3.8. Other characterization.....	48
4. GROWTHS OF LARGE-SCALE AND SINGLE-CRYSTALLINE 2D NANOMATERIALS	49
4.1. Introduction.....	49
4.2. Heteroepitaxial growth of epitaxial h-BN on Ni(111).....	51
4.3. Growth behavior of h-BN on Ni(111).....	56
4.4. Structural characteristics of epitaxial h-BN.....	63
4.5. Summary	78

5. HETEROEPITAXIAL GROWTHS OF SEMICONDUCTOR 1D NANOSTRUCTURES ON 2D NANOMATERIALS AND THEIR STRUCTURAL CHARACTERISTICS: ZNO NANOSTRUCTURES ON H-BN.....	79
5.1. Introduction.....	79
5.2. Growth of ZnO nanostructures on h-BN layers	81
5.3. Structural properties of ZnO nanostructures on h-BN layers.....	87
5.4. vdW heterointerface of ZnO/h-BN simulated by DFT	95
5.5. Position-controlled ZnO nanostructures on h-BN layers	99
5.6. Growth and structural properties of ZnO nanostructures on large-scale single crystalline h-BN layers	108
5.6.1. Growth of ZnO nanowall network on large-scale epitaxial h-BN layers.....	108
5.6.2. Structural properties of ZnO nanowall network grown on large-scale h-BN layers.....	111
5.7. Microstructure of GaN thin-film grown on h-BN layers	114
5.7.1. Introduction.....	114
5.7.2. Growth of GaN thin-film on h-BN layers.....	114
5.7.2. Microstructure of GaN thin-film grown on epitaxial h-BN.....	115
5.8. Summary.....	122
6. FLEXIBLE OPTOELECTRONIC DEVICES USING 1D-2D HYBRID NANOMATERIALS: LARGE-SCALE, SINGLE CRYSTALLINE ZNO NANOSTRUCTURES ON SINGLE-CRYSTALLINE H-BN FILMS AND THEIR FLEXIBLE UV SENSOR APPLICATIONS.....	123

6.1. Introduction.....	123
6.2. Photocurrent characteristics of ZnO nanostructures on h-BN	125
6.3. Photoconductivity of ZnO nanostructures on large scale epitaxial h-BN	129
6.4. Fabrication of the flexible UV sensor using ZnO/h-BN heterostructures.....	135
6.5. Summary	138
7. FLEXIBLE ELECTRONIC DEVICES USING 1D-2D HYBRID NANOMATERIALS: VERTICAL FIELD-EFFECT TRANSISTOR (VFET) USING ZNO NANOTUBES ON GRAPHENE LAYERS	139
7.1. Introduction.....	139
7.2. Fabrication of the ZnO nanotube VFET on graphene layers	140
7.3. Electrical characteristics of the nanotube VFET	146
7.4. 3D device simulation	149
7.5. Flexible device applications	152
7.6. Summary	155
8. CONCLUSION AND OUTLOOK.....	156
8.1. Summary	156
8.2. Future works and outlook.....	160
REFERENCES.....	163

ABSTRACT (KOREAN)	175
APPENDIX. SELECTIVE AREA HETEROEPITAXIAL GROWTH OF H-BN MICROPATTERNS ON GRAPHENE LAYERS.....	180
A.1. Introduction.....	180
A.2. Selective growth of h-BN on micropatterned graphene layers	181
A.3. Morphology of h-BN micropatterns on graphene layers	183
A.4. The growth scenario.....	186
A.5. Structural properties of h-BN micropatterns on graphene layers	189
A.6. Summary.....	195

List of Figures

- Figure 2.1** Large scale synthesis of h-BN layers using metal foils.^[3,4] (a) Optical microscope image of the synthesized h-BN films transferred on SiO₂/Si substrate. Ni substrate was used to grow h-BN layers. (b) Selective area diffraction pattern and (c) Raman spectrum of the h-BN films in (a). (d) Optical microscope image, scanning electron microscope image, atomic force microscope image and surface profile of the multilayer h-BN layers synthesized on Cu foils..... 12
- Figure 2.2** Synthesis of large-domain sized h-BN layers on metallic substrates^[7-9]. (a) Synthesis of hexagonal shape h-BN domains using electropolished copper. (b) Growth of large h-BN domains for graphene field effect transistors with enhanced mobility. (c) Evolution of h-BN domains on Cu foils with different Ni alloy composition..... 13
- Figure 2.3** Growth of h-BN monolayer on Ni(111) substrates.^[10] (a) Micropatches of h-BN on Ni(111) substrate. (b) Schematic illustration of the atomic configuration of h-BN and Ni(111)..... 14
- Figure 2.4** Electrochemical delamination of 2d materials (graphene) without dissolving the substrate.^[12] 14
- Figure 2.5** Different types of semiconductor nanostructures grown on graphene layers^[14-16]. (a) Vertically grown ZnO nanorods on graphene layers, showing enhanced nucleation on the step edges. (b) InAs nanorods and nanorocks on graphene layers grown by MOVPE. (c) InAs nanorods and (d) InAs/In_xGa_{1-x}As coaxial nanorod heterostructures grown on CVD graphene layers..... 17
- Figure 2.6** Controlled growth of ZnO nanostructures on graphene layers^[18,19]. (a) Schematic illustration of growing position-and morphology-controlled ZnO nanostructures on mechanically exfoliated graphene layers, (b) SEM images of resulting ZnO nanostructures. (c) Strategy of growth of ZnO nanotube on CVD graphene layers. (d) Photographs of ZnO nanotube grown graphene/Si wafer. (inset) Magnified SEM images of the ZnO nanotubes. 18
- Figure 2.7** Growth of GaN thin-film on graphene layers using ZnO nanowall as an intermediate layer^[20]. (a) Schematic illustration of heteroepitaxial growth of GaN thin-film on graphene layers using ZnO nanowall networks. (b) Microscope image of the

mechanically exfoliated graphene layers. (c) SEM image of dense ZnO nanowall networks. (d) SEM image of the grown GaN thin film showing flat surface morphology.....19

Figure 2.8 Microstructure of the GaN thin film grown on graphene layers^[21]. (a) Low-magnification cross-sectional image of the GaN/ZnO/graphene heterostructure. (b, c) Selective area diffraction patterns from the circle-marked area in (a).....20

Figure 2.9 Inorganic materials heteroepitaxially grown on h-BN layers^[24,25]. (a) Schematic illustration of heteroepitaxial growth of GaN thin-film on graphene layers using ZnO nanowall networks. (b) Microscope image of the mechanically exfoliated graphene layers. (c) SEM image of dense ZnO nanowall networks. (d) SEM image of the grown GaN thin film showing flat surface morphology.....23

Figure 2.10 Growth of organic materials on h-BN layers^[26]. (a) Illustration of organic layer (Rubrene) h-BN heterostructure. (b) Schematic diagram of the growth method. (c, d) Microscope images of h-BN flakes before & after Rubrene growth. (e) AFM surface topology of Rubrene grown h-BN.24

Figure 2.11 Functional optoelectronic devices fabricated using 2D nanomaterial based heterostructures^[20,24,27]. (a) Schematics of the fabrication and transfer process of LED on graphene layers, and their applications on different types of substrates. (b) Fabrication of vertical type LED using the released GaN thin films on h-BN layers. (c) Solar-cell applications of InAs/InGaAs nanowire heterostructures grown on graphene layers, and its open-circuit I - V characteristics with different device configurations.27

Figure 2.12 Electronic devices using h-BN based heterostructures^[25,26]. (a) Gate voltage dependence of the channel resistivity of the Bi₂Se₃ film grown on h-BN layers. (inset) A photograph of the fabricated device. (b) (top) Amplitude of SdH oscillations vs $1/B$ at $V_g = 60$ V and (bottom) Landau fan diagram of the peaks from TSS at the Bi₂Se₃/h-BN interface. (c) Strategy of preparing the h-BN crystal substrates with pre-patterned CVD graphene electrodes for the fabrication of the Rubrene/h-BN field-effect transistor. (d) Transfer characteristics of the Rubrene/h-BN field-effect transistor.28

Figure 3.1 Experimental procedure of the synthesis of large-scale h-BN layers. (a) Schematics of the experimental growth set-up. (b) Detailed growth procedure.....31

Figure 3.2 Schematics of the cold-wall CVD system for the growth of h-BN.....33

Figure 3.3 Schematics of the MOCVD system for the growth of ZnO nanostructures.35

Figure 3.4 Schematic illustration of (left) conventional θ - 2θ scan and (right) grazing incidence diffraction (GID).....	39
Figure 3.5 Schematic diagram of the process used to fabricate the vertical field effect transistor (VFET) arrays using the ZnO nanotube heteroepitaxially grown on graphene layers.....	43
Figure 3.6 Schematic diagram of the process used to fabricate the flexible UV sensors using ZnO nanowall networks on h-BN substrate.....	45
Figure 4.1 Repeated growth and transfer of h-BN films using Ni (111) single crystal substrate. (a) Schematic illustration of the experiment. (b) h-BN films transferred onto SiO ₂ /Si substrates. (c) Optical microscope images of h-BN films on SiO ₂ /Si substrates obtained from the same Ni (111) substrate with different number of usage.....	53
Figure 4.2 Changes of the Ni(111) substrates after multiple growths of the epitaxial h-BN layers. (a) EBSD IPF maps of the Ni (111) substrate in the normal direction (ND) and the transverse direction (TD), after 1 and 10 growths. (b) AFM image of Ni(111) substrate (a) after 1 and 10 growths.....	55
Figure 4.3 Growth behavior of h-BN film on Ni(111) using APCVD. (a) Thickness of h-BN films grown at different ammonia-borane sublimation temperatures. Insets are optical microscope images of the film on SiO ₂ /Si substrates. Scale bar: 50 μ m. (b) SAED pattern of h-BN film with ammonia-borane sublimation temperature of 95°C and 100°C. (c) Optical microscope images of h-BN films with different cooling rates. Insets are corresponding SAED patterns of the h-BN films. Scale bar: 5 nm ⁻¹ (d) High saturation optical microscope image of h-BN films transferred onto SiO ₂ /Si substrates with different growth time.	59
Figure 4.4 Growth behavior of h-BN films under different growth conditions. (a) High-saturation optical microscope images of h-BN films with ammonia-borane sublimation temperature of 93°C and growth time of 30 min and 3 hr. (b) SAED patterns of h-BN film grown under different growth temperatures, 875°C, 950°C and 1030°C.....	60
Figure 4.5 Initial growth stages of the epitaxial h-BN on Ni(111). (a) Height profile of h-BN films on SiO ₂ /Si substrate with different growth time (30 sec, 3 min and 30 min). (b) Proposed growth model of h-BN films on Ni(111).....	62
Figure 4.6 Synchrotron radiation x-ray diffraction (SR-XRD) profiles of h-BN film grown	

on Ni(111) substrate. (a) θ - 2θ scan of as grown h-BN/Ni(111). (b) Grazing incident diffraction (GID) profile of h-BN/Ni(111) with different x-ray azimuthal angles, separated by 30° . (c) Azimuthal angle(ϕ)-scan of h-BN{10-10} plane from as grown h-BN/Ni, showing six-fold symmetry. (d) HK mesh contour maps of reciprocal space mapping (RSM) around h-BN(11-20) and Ni(20-2) diffraction.....66

Figure 4.7 SR-XRD analysis of h-BN film transferred onto SiO₂/Si substrate. (a) theta-2theta(θ - 2θ) scan, (b) GID profile along the direction of h-BN<10 $\bar{1}$ 0>. (c) Azimuthal angle(ϕ)-scan of h-BN{10 $\bar{1}$ 0} plane, showing six-fold symmetry even after transfer process.....67

Figure 4.8 Microstructural analysis of h-BN film using TEM. (a) Schematic image of the SAED mapping analysis. (b) SAED image of a h-BN film from a single spot and overlaid SAED mapping images from 16 SAED patterns over a 0.3×0.3 mm² area and 9 SAED patterns over a 0.9×0.9 mm² area. (c) Schematic illustration of the TEM-EBSD analysis which visualizes real-space crystal structure. (d) TEM-EBSD IPF maps of a h-BN film in ND and TD. (e) HR-TEM image of a h-BN film. FFT image is shown in the inset71

Figure 4.9 Physical properties of the epitaxial h-BN film. (a) Optical microscope image of a h-BN film transferred onto a SiO₂/Si substrate. (b) Raman map of the h-BN E2g peak. The Raman mapping was performed in the region marked by the green square in (a). Raman spectrum of the h-BN film measured at a single spot is shown in the inset. (c) Surface morphology of the h-BN film investigated by AFM. (inset) Cross-sectional HR-TEM image of h-BN film transferred onto SiO₂/Si substrate. (d) UV-Vis-IR absorption spectrum of a h-BN film transferred onto a quartz substrate. Inset shows optical band gap analysis using Tauc's plot.74

Figure 4.10 XPS analysis of the epitaxial h-BN film transferred onto SiO₂/Si substrate. (a) XPS survey curve of the h-BN. (b, c) Detailed spectra of (b) B 1s and (c) N 1s peaks.75

Figure 4.11 Electrical characterization of the epitaxial h-BN film. (a) Optical microscope image of metal electrodes on an h-BN film transferred onto a SiO₂/Si substrate. (b) I - V characteristic curves of the h-BN film.77

Figure 4.12 Flexibility demonstration of h-BN films transferred onto 25 μ m-thick PET

film.....	77
Figure 5.1 Morphology-controlled vdW heteroepitaxy of ZnO nanostructures on h-BN substrates. Schematic of the fabrication process and tilt-view FESEM images of (a,b) ZnO vertical nanoneedle arrays and (c,d) nanowall networks. ZnO nanoneedles and nanowall networks were obtained using pristine h-BN and plasma-treated h-BN substrates, respectively.	83
Figure 5.2 Plots of root-mean-square roughness of the h-BN layer treated by (a) oxygen and (b) argon plasma as a function of the plasma treatment time. The roughness was characterized on the step-edge-free h-BN areas of $1 \times 1 \mu\text{m}^2$ to clarify the roughening effect of plasma treatment. Error bars denote the standard deviations.....	84
Figure 5.3 Effect of h-BN surface roughness on nanowall density. (a) Top-view SEM images of ZnO nanowalls formed on h-BN layers treated by oxygen plasma for 0, 15, and 60 sec. (b) Plot of nanowall line density as a function of the plasma treatment time. Error bars denote the standard deviations.....	85
Figure 5.4 Tilt-view SEM image of ZnO nanostructures grown on bare h-BN exfoliated from h-BN crystallites. Three different morphologies are obtained: i) isolatedly grown ZnO nanoneedles; ii) high density nanoneedles or iii) nanowall with high density nanoneedles in a specific alignment.....	86
Figure 5.5 Heterointerface of vdW epitaxial ZnO/h-BN observed by cross-sectional TEM. (a) Low-magnification cross-sectional TEM image of vertical ZnO nanoneedles grown on h-BN. (b) HRTEM lattice images of the ZnO nanoneedle/h-BN heterointerface. The right insets are selected-area diffraction patterns obtained through a FFT process of the HRTEM images marked with enclosed areas. (c) Experimental and simulated CBED patterns of ZnO nanoneedles preferentially grown along the O-polar $(000\bar{1})$ direction.	91
Figure 5.6 VdW heteroepitaxial relationship of ZnO/h-BN investigated by plan-view TEM. (a) Plan-view low-magnification TEM image of ZnO nanoneedles grown on few-layer h-BN. (b) Plan-view HRTEM lattice image displaying in-plane epitaxial relationship of ZnO/h-BN. Diamond-shape Moiré patterns are repeatedly observed every 1 nm. (c) SAED patterns obtained from the area shown in the inset (scale bar, 100 nm). (d) Intensity profile of electron beam diffraction of ZnO $(10\bar{1}0)$ as a function of the central	

angle.....92

Figure 5.7 Ball-and-stick model for vdW epitaxial ZnO/h-BN heterostructure. (a) Low-magnification model for $(000\bar{1})[10\bar{1}0]\text{ZnO} \parallel (0001)[10\bar{1}0]\text{h-BN}$ heterostructure viewed along $[0001]$. The image clearly exhibits periodic triangular Moiré fringes with a periodicity of ~ 1.0 nm. (b) Diffraction patterns obtained from a through a Fourier-transform-based simulation. (c) High-magnification ball-and-stick model. (d) Two heterointerfacial atomic epitaxial relationships for ball-to-ball (upper panel) and ball-to-hollow (bottom panel) configurations appearing in the Moiré pattern. (e) Two supercell structures of ball-top-matching (Type I) and hollow-matching (Type II) $(3 \times 3)\text{-ZnO}/(4 \times 4)\text{-BN}$ heterojunctions for the incommensurate vdW ZnO/h-BN heterostructure.....93

Figure 5.8 Electronic structure and adhesion energy of the vdW epitaxial ZnO/h-BN heterointerface computed by the DFT method. Atomic model structures and electron density difference isosurfaces at the periphery of the heterointerfaces with (a) ball-top-matching and (b) hollow-matching configurations of ZnO/h-BN. The electron density was contoured with an isovalue of $\pm 0.0002e \text{ \AA}^{-3}$. (c) vdW heterointerfacial adhesion energy and equilibrium vdW distance values for type I and II supercells. (d) The electron populations in the ZnO and h-BN parts of the supercells before and after the vdW epitaxy, calculated by Bader analysis. The electronic structure mapped at the ZnO/h-BN heterointerface implies a vdW binding feature with less electron orbital hybridization.97

Figure 5.9 Shape-controlled vdW heteroepitaxy of ZnO nanoarchitectures on h-BN layers. (a) Schematic of selective growth of ZnO nanowalls on h-BN films for shaping the outer nanowalls. Tilt-view SEM image of ZnO (b-c) nanoarchitectures on h-BN films with designed shape and spatial arrangements. (d) Cross-sectional schematic showing how ZnO nanoarchitectures are formed on a plasma-treated h-BN area via the vdW-MOVPE. (e) Room-temperature CL spectra of ZnO nanostructures. The insets are top-view SEM images (upper) and the corresponding monochromatic CL image obtained at a photon energy of 3.25 eV (bottom)..... 103

Figure 5.10 H-BN layer etched by plasma treatment. (a) Optical micrograph of h-BN layer treated by oxygen plasma for 1 min via polymer resist layer with line-opening patterns. (b) AFM topological map of h-BN flake marked in (a). The polymer resist was

removed before the AFM measurement. (c) Depth profile of the h-BN surface measured along the red dotted line depicted in (b). The etch rate is estimated to be 0.5–0.8 Å sec⁻¹..... 104

Figure 5.11 Photoluminescent characteristics of ZnO nanoarchitectures grown on h-BN by vdW epitaxy. A series of PL spectra was measured at various temperatures in the range of 11–180 K. The spectrum at 11 K shows seven distinct NBE emission peaks at 3.376, 3.364, 3.361, 3.359, 3.351, 3.319, and 3.235 eV. The PL peak at 3.376 is attributed to a free exciton peak (XA). The peaks at 3.359, 3.351, and 3.364 eV are ascribed to neutral-donor bound excitonic emissions (I2) [see Ref. S1, S2]. The sharp and strong NBE emission indicates high optical quality of ZnO nanoarchitectures grown by vdW epitaxy (see inset). The excellent PL properties may result from the high crystallinity of ZnO nanoarchitectures because threading dislocations were not generated from the vdW heterointerface, as confirmed by HRTEM observations. 105

Figure 5.12 Transmission electron microscopic analysis of ZnO nanoarchitectures. (a) Cross-sectional low-magnification TEM image of ZnO nanostructure arrays. (b) Selected-area electron diffraction (SAED) patterns obtained from the dotted line circle marked in (a), confirming the single crystallinity of the nanoarchitectures. The ZnO nanoarchitectures grew along the c-axis of wurtzite normal to the surface of h-BN. (c) Experimental and simulated convergence beam electron diffraction (CBED) patterns of ZnO nanoarchitectures preferentially grown along the O-polar (000 $\bar{1}$) direction. The sample thickness for CBED was 37 nm, and the simulation was performed under the same thickness condition. Plan-view (d) low-magnification TEM image and (e) SAED patterns of ZnO nanowalls grown on few-layer h-BN. The SAED patterns exhibit the heteroepitaxial relationship of (000 $\bar{1}$)[10 $\bar{1}$ 0]ZnO || (0001)[10 $\bar{1}$ 0]h-BN. 106

Figure 5.13 Large-scale growth of ZnO nanostructures on the large-scale, single-crystalline h-BN layers. (a) Schematic illustration of the heteroepitaxial growth of ZnO nanostructures on single crystalline h-BN film. (b) The photograph of the ZnO nanostructures heteroepitaxially grown on the single crystalline h-BN film. (c) Tilted-view FE-SEM image of ZnO nanostructures grown on h-BN and SiO₂. 110

Figure 5.14 Structural properties of ZnO nanostructures grown on single crystalline h-

BN film and the SiO₂ layer. (a) $\theta - 2\theta$ scan and (b) ϕ -scan of ZnO {10-11} of ZnO nanostructures grown on (red) the single crystal h-BN layer and (black) the SiO₂ layer. 113

Figure 5.15 TEM analysis of the GaN films grown on large-scale epitaxial h-BN. (a) Low-magnification image of the cross-sectional GaN/h-BN. (b, c) SAED patterns obtained from the low-quality buffer and high-quality thin-film area marked by white dashed circles. 118

Figure 5.16 Two-beam dark-field images of the cross-sectional GaN thin-film on h-BN, with respect to the different burgers vector. (a) $g = (0002)$ which corresponds to the screw dislocations, and (b) $g = (10-10)$ which corresponds to the edge dislocations. 119

Figure 5.17 Two-beam dark field image of the planar GaN thin-film sample, showing low-angle grain boundaries and threading dislocations. 120

Figure 6.1 UV photoconductor device of ZnO nanowall/h-BN. (a) Schematics of ZnO nanowall network/h-BN photoconductor device with three different electrode configurations. (b) $I-V$ characteristic curves of ZnO nanowall networks, ZnO nanowall/h-BN heterojunction, and bare h-BN layer measured in dark room. Inset is the $I-V$ curves of ZnO nanowall-h-BN heterojunction (black solid line) and bare h-BN layer (red solid line). (c) Time response curve of photocurrent measured at applied bias voltage of 1.0 V. 127

Figure 6.2 $I-V$ characteristic curves of (a) ZnO nanowalls, (b) ZnO nanowall-h-BN heterojunction, and (c) bare h-BN layer measured under UV irradiation (red lines) and (black lines) dark room conditions. 128

Figure 6.3 Power-dependent photocurrent characteristics of ZnO nanostructures grown on h-BN or SiO₂ substrates. (a) Linear and (b) semi-log plot of the $I-V$ characteristics of ZnO/h-BN. (c) Linear and (d) semi-log plot of the $I-V$ characteristics of ZnO/SiO₂. 132

Figure 6.4 Normalized spectral response curves of ZnO nanostructures grown on h-BN and SiO₂ substrates. 133

Figure 6.5 Temporal response and decay curve fitting of the photocurrent in ZnO/h-BN. (a) Temporal response of the ZnO nanostructures on h-BN and SiO₂ substrates. (b) Normalized decay behaviors of the ZnO nanostructures on h-BN and SiO₂ substrates,

with biexponential decay fitting curves. (c) Factors of biexponential decay models of the photocurrent in ZnO/h-BN and ZnO/SiO₂, calculated from the fitting curves in (b).. 134

Figure 6.6 Schematic diagram of the process for fabricating flexible UV sensors using ZnO/h-BN heterostructures. (b, c) Photographs of the fabricated flexible UV sensor (b) as fabricated and (c) transferred onto flexible substrates and bent. (d) I–V characteristics of the flexible UV sensor under dark and UV-illuminated conditions. (e) Time-dependent photocurrent behavior of the flexible UV sensors under different bending conditions. 137

Figure 7.1. ZnO nanotubes grown on graphene layers and its structural properties. (a) Tilted-view scanning electron microscopy (SEM) images of the position- and dimension-controlled ZnO nanotube arrays. Hexagonal nanotube arrays with diameters of (top-left) 160 nm and (top-right) 300 nm and arrays with spacings of (bottom-left) 1 μm and (bottom-right) 6 μm. (b) (top) Selective area electron diffraction (SAED) image of a ZnO nanotube. (bottom) High-resolution transmission electron microscopy image of a ZnO nanotube. 142

Figure 7.2. Fabrication of the ZnO nanotube VFET and its structure. (a) Schematic diagram of the process used to fabricate the vertical field effect transistor (VFET) arrays using the ZnO nanotube heteroepitaxially grown on graphene layers. Field-emission SEM (FE-SEM) images of a ZnO nanotube array on a graphene substrate (b) after formation of conformal gate electrodes, and (c) after fabrication of the VFET structure. (d) Cross-sectional FE-SEM image of the nanotube VFET..... 145

Figure 7.3 Electrical characteristics of the fabricated VFET. (a) $I_{ds} - V_{gs}$ transfer characteristic curves of the VFETs. (b) $I_{ds} - V_{ds}$ output characteristic curves of the VFET. 148

Figure 7.4 3D simulation of the ZnO nanotube VFET. (a) Simplified model of the nanotube VFET used in transport simulation. (b) Transport simulation of the nanotube VFET and comparison to experimental data. (c) Distribution of the carrier concentration in the ZnO nanotube at different gate biases, according to the results of our simulation. 151

Figure 7.4 Mechanical transfer of the fabricated VFET onto flexible substrate. (a) Schematic diagram of the process used to fabricate flexible VFETs with mechanical lift-

off. (b) Photographs of the device transfer process. (c) Transfer curves of the nanotube VFET before and after transfer. 154

Figure A.1. (a) Schematic diagram of the process used to fabricate the position-controlled h-BN/graphene heterostructure. (b) Atomic force microscopy (AFM) topographic image and height profile (inset) of patterned graphene layers after focused ion beam (FIB) irradiation and thermal annealing in ammonia. (c) Tilt-view field-emission scanning electron microscopy (FE-SEM) image of selectively grown h-BN on the micropatterned graphene layers. Top-view FE-SEM image (inset) of the same. 182

Figure A.2. (a) Surface topography of selectively formed h-BN investigated by atomic force microscopy (AFM). (b) The height profiles (black) and theoretical expectation of the surface profile with a diffusion length of 200 nm (red). 185

Figure A.3. Growth scenario of h-BN on focused ion beam (FIB)-patterned graphene layers, illustrating the mechanism of position-selective nucleation and side-wall thickening. 188

Figure A.4. High-resolution synchrotron radiation X-ray diffraction analysis (SR-XRD) of the selectively formed h-BN micropatterns on graphene layers. (a) θ - 2θ scan near the (0002) diffraction of h-BN on the graphene layers. (b) Reciprocal space mapping around the diffraction of $(0002)_{h\text{-BN}}$ and $(0002)_{\text{graphene}}$. The inset shows the detailed profile of the diffraction indicated by the red arrows. 191

Figure A.5. Microstructural properties of h-BN selectively formed on graphene layers investigated by transmission electron microscopy (TEM). (a) Selective-area electron diffraction (SAED) patterns obtained from a single h-BN micropattern. Top and middle inset: Magnified images of diffraction from the $(10\bar{1}0)$ and $(\bar{1}2\bar{1}0)$ planes of h-BN and graphene. Bottom inset: Plan-view image of an h-BN micropattern on the graphene layers. (b) Cross-sectional image of h-BN/graphene and high-resolution TEM (HR-TEM) images of the enclosed area. Inset: Fast Fourier transform (FFT) images of h-BN. 194

List of Tables

Table 3.1. Summary of precursors and gases used in the growth of h-BN, graphene using CVD system, and ZnO using MOCVD system.....	36
Table 3.2 Typical parameters in bench-top XRD and SR-XRD analysis.....	39
Table 3.3 Typical process conditions for fabrication of flexible VFET using ZnO nanotubes grown on graphene layers.	42
Table 3.4 Typical process conditions for fabrication of flexible UV sensor.....	46
Table 5.1 Comparison of the density of threading dislocation of GaN thin-films grown on different substrates.....	121

1. Introduction

1.1. Motivation: Potentials of hexagonal boron nitride (h-BN) based hybrid nanomaterials for flexible and wearable device applications

Flexible & stretchable devices are getting tremendous interests as next-generation mobile devices since the paradigm shifts from hand-held to wearable devices.^[1] Wearable devices will be monitoring and analyzing human activities in real-time, providing intelligent supports combined with its powers of computing and communicating. To achieve the flexible and stretchable formfactors, organic materials have been widely employed as active materials due to their excellent scalability with low process temperature and low cost of fabrication. However, unsatisfactory physical properties such as low electron mobility, easy degradation and poor integration density have hindered them to be used widely. On the other hand, it is well known that inorganic materials exhibit superior performance and reliability. Nevertheless, high growth temperature and difficulties of the release process from the rigid substrates limited them to be employed in flexible or stretchable devices.

To overcome the challenge, a hybrid material system composed of one dimensional (1D) inorganic nanostructures on two dimensional (2D) nanomaterials has been recently proposed. The high-quality inorganic nanostructures could serve

as an efficient channel for electronic and optoelectronic devices with better electrical and physical properties, such as high carrier mobility, higher electron-hole recombination rate, better thermal or chemical resistance or superior reliability. In addition, functionalities such as flexibility, transparency or transferability can be offered from the 2D nanomaterial substrates. Consequently, heteroepitaxy of semiconductors on two-dimensional nanomaterials could suggest a new paradigm for the fabrication of functional devices such as transferable and flexible electronic and optoelectronic devices.

Hexagonal boron nitride (h-BN) is an ideal material for this hybrid nanomaterial system. H-BN is a layered 2D material having a honeycomb lattice structure consists of boron and nitrogen. Because of its wide bandgap of 5.2–5.9 eV, h-BN normally exhibits electrically insulating properties. On the other hand, it is famous for its excellent physical properties such as high thermal conductivity, chemical/mechanical stability and mechanical strength. Importantly, its unique structural properties and great chemical/mechanical stability makes it favorable substrates for the heteroepitaxy of semiconductors. The hexagonal structure of the h-BN is compatible with many different types of semiconductors having wurtzite, zinc blende or diamond structures. On the other hand, high chemical/thermal stability allow it to be used in the heteroepitaxial growth in which chemical reactions occur under high-temperature. Furthermore, the layered structure allows the device fabricated on h-BN to be mechanically released, a very important process

in the fabrication of flexible devices. Accordingly, h-BN is an attractive platform for 2D nanomaterial-based hybrid nanomaterials for the fabrication of flexible electronic and optoelectronic devices.

In this dissertation, synthesis, characterization and device applications of the h-BN based hybrid nanomaterials are discussed. The research will suggest a new paradigm in the industry of semiconductor electronic and optoelectronics.

1.2. Objective and approach

Multiple issues remain unsolved in the heteroepitaxial growth of semiconductor nanostructures on the h-BN layers and their device applications. The main objective of the dissertation is to seek the answers or solutions for such issues related to building high-quality h-BN based heterostructures and their applications.

The synthesis of large-area, high-quality h-BN film would be the most important initial step to achieve h-BN based heterostructures which can be further employed in practical applications. The basic approach in this dissertation is to utilize the heteroepitaxial growth of h-BN nanosheets on single crystalline Ni substrates, in combination with non-destructive transfer of the synthesized h-BN film: an electrochemical delamination technique. As presented in Chapter 4, it shows a good promise to synthesis a single-crystalline h-BN in a scalable way, with reduced cost of process by recycling the single crystalline Ni substrates.

Understanding the growth mechanism of semiconductor nanostructures on h-BN films is highly important because not only it reveals a unique physics of epitaxy on non-covalent surface, but also it allows us to engineer the h-BN based heterostructures in a controlled way. The studies on the growth mechanism, microstructural properties and defect analysis of the semiconductor nano/microstructures on h-BN layers are presented in the Chapter 5.

For better structural characterizations, the conventional characterization

methods like the bench-top X-ray diffraction (XRD) study could not be employed for the 2D nanomaterial based heterostructures, due to the limited interaction volume of 2D nanostructures. Accordingly, the synchrotron-radiation XRD (SR-XRD) study, which uses an extremely strong light source, is required to understand the structural characteristics of 2D materials and their heterostructures. For example, heteroepitaxial relationships of h-BN films grown on Ni(111) substrates and graphene substrates were investigated using SR-XRD, which are discussed in Chapter 4 and Chapter A. Furthermore, micro-fabricated planar and cross-sectional samples prepared by in-situ growth or focused-ion beam (FIB) technique allow us to investigate their structural properties using transmission electron microscopy (TEM) in an atomic level. In particular, the study on defect structures of semiconductor thin-films on h-BN using micro-fabricated samples shows great promises in fabricating nanoscale electronic devices with compatible material qualities compared to other thin-films on conventional substrates.

Fabrication of flexible electronic and optoelectronic devices using h-BN based hybrid nanomaterials were discussed in the Chapter 6 and 7. To fully utilize the flexibility of the hybrid system, a special device structure was presented in Chapter 6, including patterning of the nanostructures, formation of electrical interconnections and the mechanical release of the fabricated device. For those vertical nanostructure devices, due to the difference of three-dimensional (3D) device architectures with conventional 2D device structures, it is very crucial to develop

new fabrication techniques, including gap insulation and conformal contact formation, for the reliable device fabrication. The details can be found in the Chapter 7.

There are also other material-related issues, such as catalyst-free growth of h-BN nanostructures and their growth control. Although the suggested issues are not the scope of this dissertation, it will be briefly discussed in the end of dissertation because it is also closely related with nanodevice applications.

1.3. Outline

The dissertation is composed of eight chapters including this introductory chapter. In the following Chapter 2, the current research activities on growth, characterizations, and electronic and optoelectronics device applications of 2D nanomaterials and their heterostructures will be briefly reviewed. The experimental methods that have been used in this dissertation will be described in Chapter 3, including detailed process of material growth and device fabrication, as well as structural, optical and electrical characterizations. In Chapter 4, the growth of large-scale single crystalline h-BN films using heteroepitaxy on Ni(111) will be discussed. Chapter 5 presents the comprehensive study on the growth of ZnO nanostructures on h-BN substrates, so called van der Waals epitaxy. Position-controlled growth of ZnO nanostructures on h-BN was demonstrated by selective-area plasma treatment, where the idea comes from detailed structural investigations, supported by first-principle calculation. Defect structures of the GaN thin-films grown on h-BN layers will be also discussed. In Chapter 6, flexible ultra violet (UV) sensors were fabricated using ZnO nanostructures grown on h-BN films, followed by the mechanical transfer on flexible substrates. It turned out that by using single crystalline h-BN films, single oriented ZnO nanostructures were grown on the h-BN and showed better performance as a UV sensor, compared to the ZnO nanostructures on amorphous substrates such as quartz. In Chapter 7, in a practical approach, semiconductor nanotube based vertical field effect transistor (VFET) was

demonstrated. Position-controlled grown ZnO nanotube on graphene films was used to fabricate VFET, and readily transferred onto flexible substrates. Although the device was prepared on graphene layers, it can readily be integrated with h-BN and its heterostructures. Finally, in Chapter 8, the research works in this dissertation will be summarized with possible suggestions for future works and give an outlook for h-BN based hybrid material system for practical applications in flexible high-performance electronic and optoelectronic devices.

2. Literature review

In this chapter, current research activities on growth and device applications of h-BN layers and their heterostructures are reviewed. First, large-scale synthesis of h-BN layers are discussed, as a primary building block of the hybrid nanomaterial system. Large-scale growth of graphene layers will be briefly reviewed as well because it is closely related to the growth of the h-BN. Next, a review on the 1D-2D hybrid material system is followed, which is mainly focused on the graphene-based system as they opened the field of the 1D-2D hybrid materials. After the overview of the synthesis of 2D materials and their heterostructures, their functional device applications, such as transferrable and stretchable optoelectronic devices are explained more in detail. Finally, the current status and issues of 1D-2D hybrid materials system and their applications are discussed.

2.1. Growths of large scale, single crystalline h-BN layers and related materials

The current technologies for the synthesis of large-scale h-BN are primarily based on the chemical vapor deposition (CVD) methods, in which usually metal foils or films are used as catalytic substrates. Large-scale growths of few-layered h-BN films were first reported using copper or nickel foils as substrates.^[2-4] In these

methods, ammonia borane or borazine were vapor transported into the chamber as a precursor, and h-BN layers are formed on the surface of metal foils. Typical growth temperature ranges from 800 to 1000 °C. The number of layers of the grown h-BN depends on multiple parameters, such as a type of metal foil, growth temperature, feed rate of the precursor, crystal orientation of the surface, etc. Moreover, uniform monolayer h-BN films over large area were achieved by several groups^[2,5,6]. It should be noted that the methodology of h-BN growth using CVD with metallic substrates was greatly inspired by the large-scale synthesis of graphene layers.

Although the CVD growth method offers sufficient scalability, it is challenging to grow single crystalline films because of the polycrystalline nature of the metallic substrates. Considering that the polycrystal nature of 2D materials can permanently degrade the performance of the materials itself, as well as 1D-2D hybrid material system based on them, it is highly important to synthesize a single-domain 2D nanomaterials over large scale.

One of the way to get a single crystalline film is to make the individual grain size as large as possible. The effort to increase the domain size of CVD h-BN have achieved significant progress recently.^[7-9] Suppressing the nucleation density was a key parameter to get larger domain sizes of few millimeters or even few centimeters. Surface treatment was also important to minimize the nucleation density. Using electropolishing methods, the root-mean square (rms) surface

roughness value decreased down to few tens of nm scale.

On the other hand, utilizing the heteroepitaxial growth on single crystalline metal substrates is another way to achieve single crystalline 2D materials. Ni(111) is widely used substrate for the heteroepitaxial growth, because of its lattice matching structure with h-BN. Molecular beam epitaxy was widely used to grow h-BN heteroepitaxially on Ni(111) substrates.^[10] Similarly, Ru(0001) and Rh(111) substrates were also used as the substrates to heteroepitaxially grow h-BN layers^[11]. However, the lack of methodology to separate the grown film without damaging the substrates have hindered the research to be widely spread to produce high-quality h-BN layers.

Majority of growth methods requires dissolving metallic substrate to separate the grown films. However, the grown film can be nondestructively separated as well, so called electrochemical delamination, without consuming the substrates.^[12] The method utilizes a generation of hydrogen bubbles which separates the substrates and films, by applying a bias to the film/substrates in the conductive liquid. Usually the substrates can be re-used after transfer process. The advantages of recycling the substrates made this method widely used in the h-BN synthesis, especially expensive substrates such as platinum was used^[13].

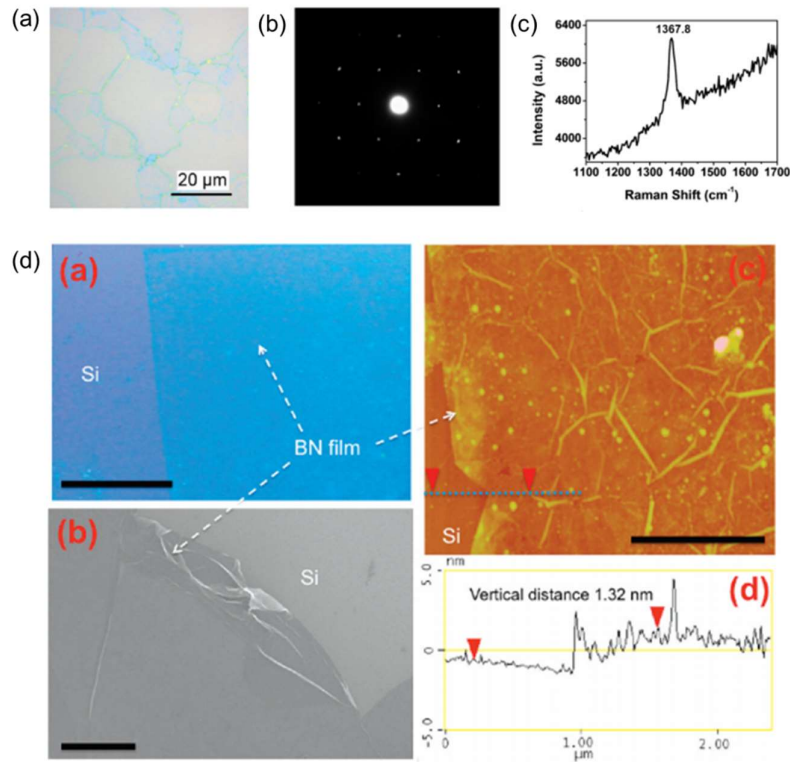


Figure 2.1 Large scale synthesis of h-BN layers using metal foils.^[3,4] (a) Optical microscope image of the synthesized h-BN films transferred on SiO₂/Si substrate. Ni substrate was used to grow h-BN layers. (b) Selective area diffraction pattern and (c) Raman spectrum of the h-BN films in (a). (d) Optical microscope image, scanning electron microscope image, atomic force microscope image and surface profile of the multilayer h-BN layers synthesized on Cu foils.

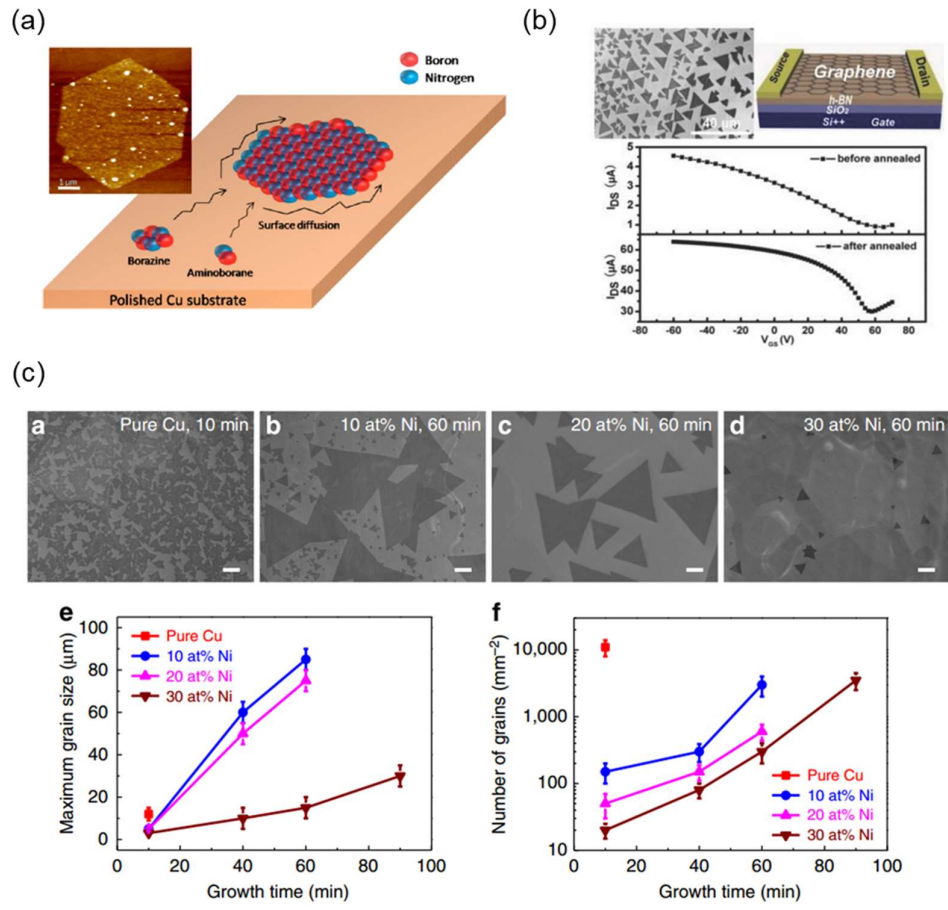


Figure 2.2 Synthesis of large-domain sized h-BN layers on metallic substrates^[7–9]. (a) Synthesis of hexagonal shape h-BN domains using electropolished copper. (b) Growth of large h-BN domains for graphene field effect transistors with enhanced mobility. (c) Evolution of h-BN domains on Cu foils with different Ni alloy composition.

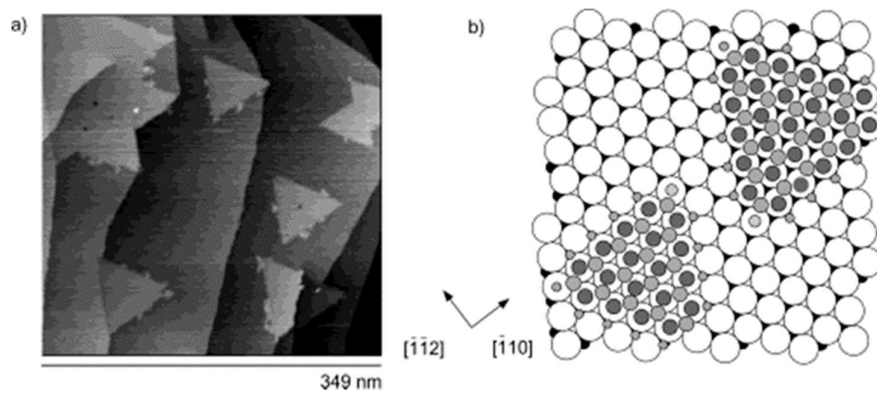


Figure 2.3 Growth of h-BN monolayer on Ni(111) substrates.^[10] (a) Micropatches of h-BN on Ni(111) substrate. (b) Schematic illustration of the atomic configuration of h-BN and Ni(111)

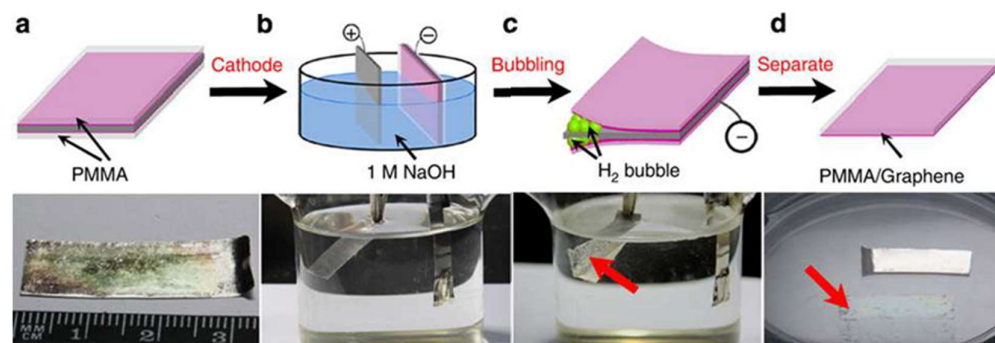


Figure 2.4 Electrochemical delamination of 2d materials (graphene) without dissolving the substrate.^[12]

2.2. Growths of inorganic nanostructures/thin films on h-BN layers or related materials

The growth of inorganic microstructures/thin films on h-BN layers can provide a unique opportunity to fabricate high-performance, functional electronic and optoelectronic devices with transferrable, flexible or stretchable properties. H-BN has not been widely studied as growth substrates yet, while most inorganic nanostructures/thin films were grown on single crystalline substrates and showed excellent material properties and device performance. However, few reports on the growth of inorganics on h-BN layers exhibited the strong potential of the h-BN based hybrid structure. Before explaining the researches on the h-BN based works, growth of semiconductor nanostructures on graphene layers will be discussed first.

2.2.1. Growth of semiconductor nanostructures on graphene layers

Different types of materials were grown on graphene layers, to exploit the potential of the 1D-2D hybrid materials. ZnO nanoneedles were grown on mechanically exfoliated graphene layers, using metal organic vapor phase epitaxy.^[14] In this work, ZnO nanoneedles were vertically aligned, implying the heteroepitaxial relationship between ZnO and graphene layers. Similarly, InAs nanowires, as a narrow band gap material, were grown on mechanically exfoliated graphene layers, using MOCVD^[15] or MBE^[16]. Thorough studies on the

microstructure of InAs and graphene revealed that heteroepitaxial growth on graphene is possible even though there exists lattice mismatch.^[17] Not only homogeneous materials, coaxial structures such as InAs/InGaAs coaxial nanorods were grown on graphene layers as well, showing the possibility of combining the quantum structure with graphene layers.^[16]

Also, the observation of an enhanced nucleation on the step edges of the graphene layers lead to the development of the precise growth control.^[14] Position- and morphology-controlled ZnO nanotubes were grown on both mechanically exfoliated or CVD synthesized graphene layers.^[18,19]

Thin films are difficult to be grown directly on graphene layers. To circumvent this problem, ZnO nanowalls, which were heteroepitaxially grown on graphene layers, were employed as an intermediate layer. GaN thin films were grown on the ZnO coated graphene layers and exhibited good physical properties which is comparable to the GaN thin films on sapphire substrate.^[20-23]

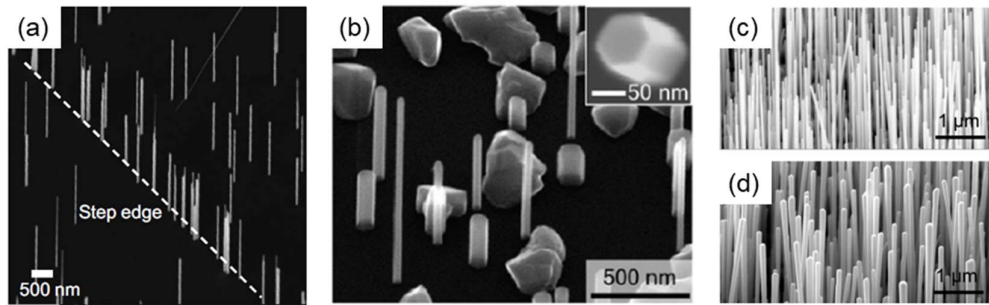


Figure 2.5 Different types of semiconductor nanostructures grown on graphene layers^[14–16]. (a) Vertically grown ZnO nanorods on graphene layers, showing enhanced nucleation on the step edges. (b) InAs nanorods and nanorocks on graphene layers grown by MOVPE. (c) InAs nanorods and (d) InAs/In_xGa_{1-x}As coaxial nanorod heterostructures grown on CVD graphene layers.

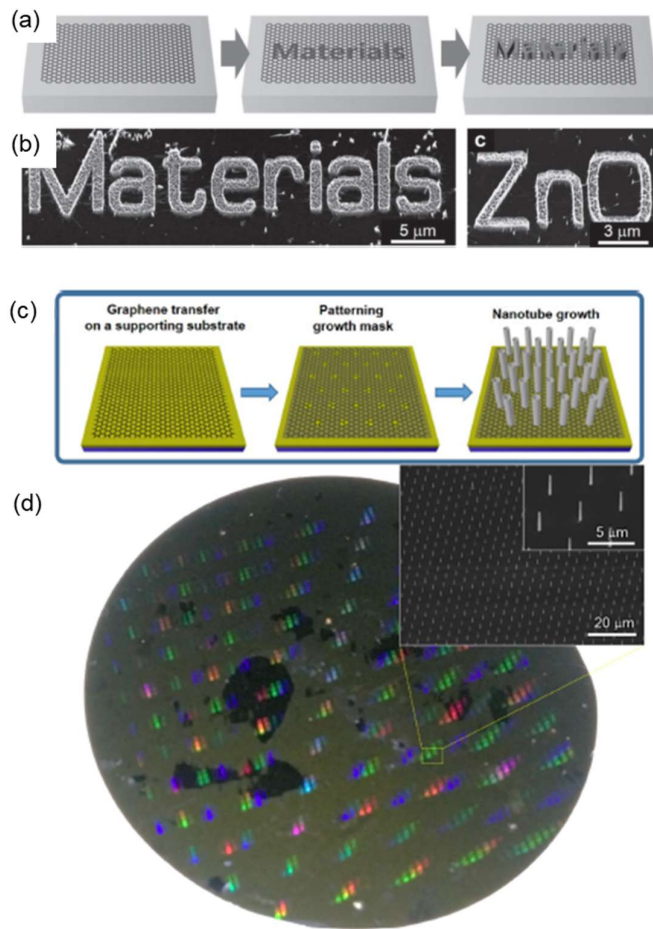


Figure 2.6 Controlled growth of ZnO nanostructures on graphene layers^[18,19]. (a) Schematic illustration of growing position- and morphology-controlled ZnO nanostructures on mechanically exfoliated graphene layers, (b) SEM images of resulting ZnO nanostructures. (c) Strategy of growth of ZnO nanotube on CVD graphene layers. (d) Photographs of ZnO nanotube grown graphene/Si wafer. (inset) Magnified SEM images of the ZnO nanotubes.

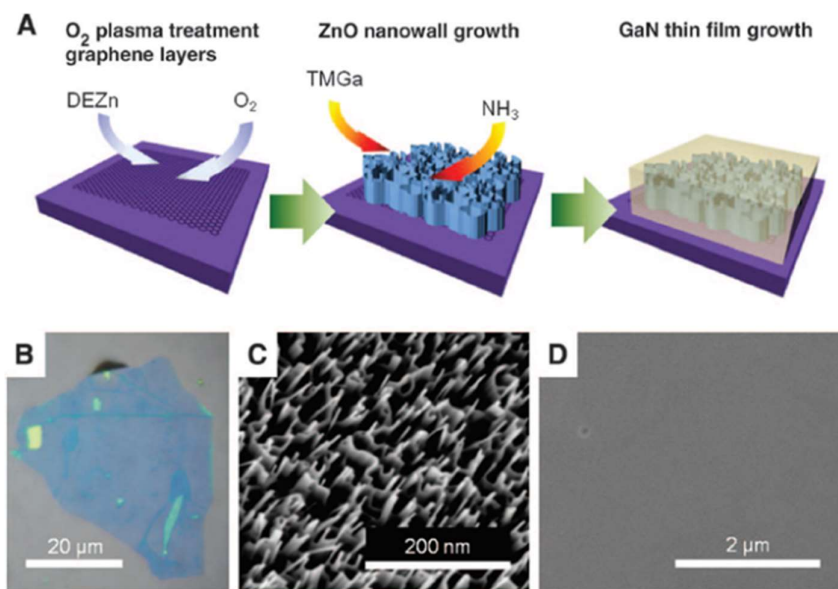


Figure 2.7 Growth of GaN thin-film on graphene layers using ZnO nanowall as an intermediate layer^[20]. (a) Schematic illustration of heteroepitaxial growth of GaN thin-film on graphene layers using ZnO nanowall networks. (b) Microscope image of the mechanically exfoliated graphene layers. (c) SEM image of dense ZnO nanowall networks. (d) SEM image of the grown GaN thin film showing flat surface morphology.

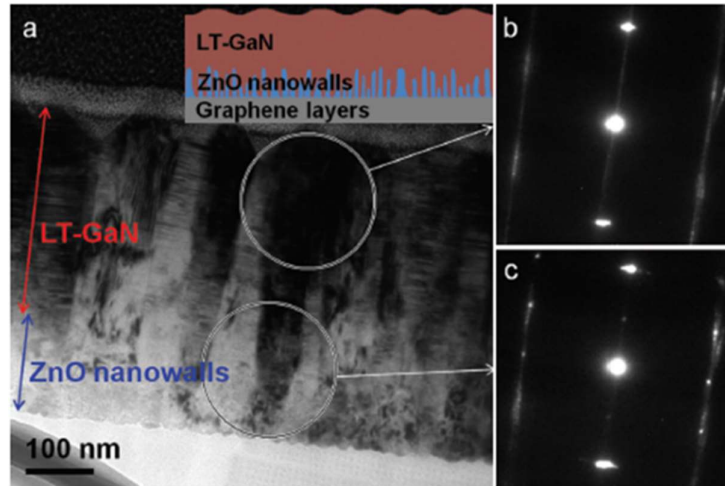


Figure 2.8 Microstructure of the GaN thin film grown on graphene layers^[21]. (a) Low-magnification cross-sectional image of the GaN/ZnO/graphene heterostructure. (b, c) Selective area diffraction patterns from the circle-marked area in (a).

2.2.2. Growth of inorganic materials on h-BN layers

In contrast to the graphene-based hybrid materials, h-BN has been recently considered as a functional template for the heteroepitaxial growth, and only few researches are reported so far. However, these researches showed significant breakthroughs which cannot be achieved by conventional approaches.

As a layered material, h-BN was employed as a substrate and a mechanical release layer at the same time, to grow and release GaN thin films^[24]. The researchers showed that MOCVD grown few layer h-BN on sapphire, followed by the growth of AlN buffer layers and GaN thin films. The film exhibited comparable qualities to the GaN on sapphire, in terms of defect density. Interestingly, the crystal quality improved when the GaN thin film was released, due to the reduced stress which come from the substrate.

In addition to the conventional semiconductors, h-BN is also an ideal substrate for growing another two-dimensional material since the surface of h-BN is atomically flat and free of dangling bonds. As a demonstration, Bi₂Se₃, a topologically insulating two-dimensional material, was grown on mechanically exfoliated h-BN layers using MBE^[25]. Microstructural studies revealed that the grown Bi₂Se₃ is of single crystalline without significant defects due to the heteroepitaxial relationship with h-BN. It should be noted that the interface with the underlying h-BN substrates was atomically clean without intermediate layers.

Interestingly, organic materials were grown on the h-BN to form organic/inorganic 2D van der Waals heterostructure^[26]. In this research, organic material (Rubrene) was vapor transported to the h-BN, and formed van der Waals heterostructure.

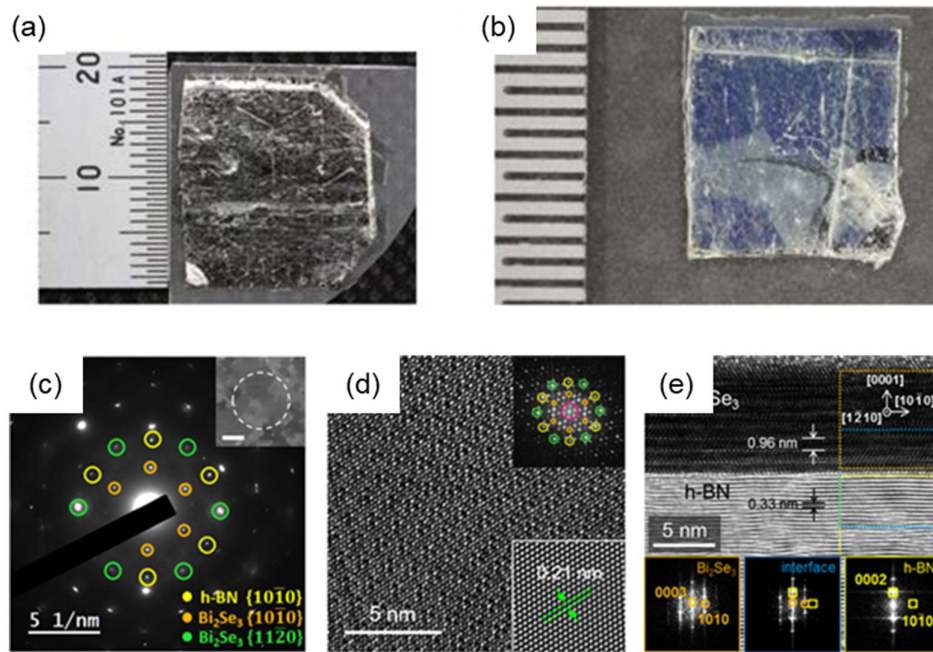


Figure 2.9 Inorganic materials heteroepitaxially grown on h-BN layers^[24,25].

(a) Schematic illustration of heteroepitaxial growth of GaN thin-film on graphene layers using ZnO nanowall networks. (b) Microscope image of the mechanically exfoliated graphene layers. (c) SEM image of dense ZnO nanowall networks. (d) SEM image of the grown GaN thin film showing flat surface morphology.

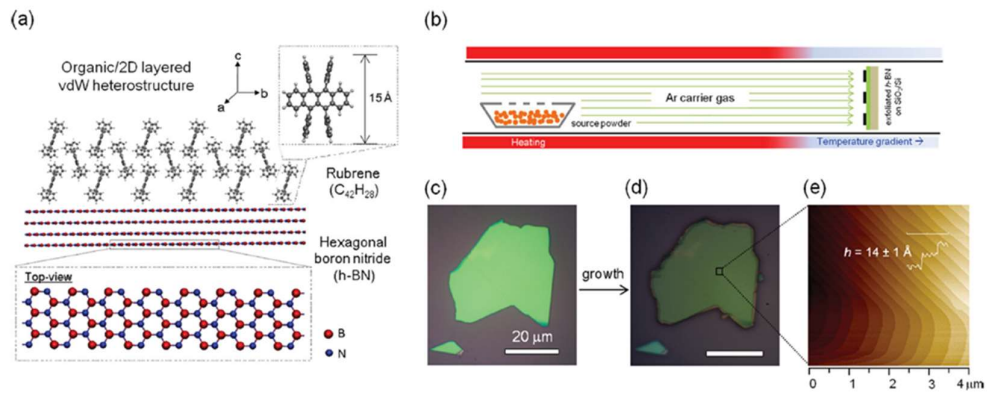


Figure 2.10 Growth of organic materials on h-BN layers^[26]. (a) Illustration of organic layer (Rubrene) h-BN heterostructure. (b) Schematic diagram of the growth method. (c, d) Microscope images of h-BN flakes before & after Rubrene growth. (e) AFM surface topology of Rubrene grown h-BN.

2.2.3. Functional optoelectronic devices using 1D-2D hybrid nanomaterials

2D nanomaterial-based hybrid nanomaterials opened a unique way to fabricate electronic and optoelectronic devices with additional functionality. Especially, by taking advantages of the layered structure, transferrable devices were reported. Since the device layer can be released mechanically and transferred onto arbitrary substrates, this method enabled to integrate inorganic materials on flexible or stretchable form factor.

The first transferrable optoelectronic device using 2D material was demonstrated by Chung et al^[20]. In this research, GaN thin-films and quantum structures for LED were grown on graphene layers using ZnO nanowall as a intermediate layer. After fabrication, the LED was mechanically transferred onto the arbitrary substrates such as plastic, glass or metal, showing the flexibility of the method. A very similar approach – transferrable GaN device using 2d material as a release layer – was demonstrated again by another team^[24]. They grew GaN thin-film on h-BN grown sapphire, transferred the film, then fabricated the released film into a vertical LED. Nowadays, many researchers report growth and transfer of GaN thin films and related devices grown on 2D nanomaterials, mainly graphene or h-BN. This indicates that the approach is solid, versatile and universal, overcoming the current challenge in the field of GaN devices.

In combination with narrow band gap materials, nanowire based solar cell was demonstrated, by using InAs/InGaAs nanowire grown on graphene layers. In this study, the graphene was used as a heteroepitaxial template and bottom electrode at the same time. The fabricated device exhibited a highest efficiency reported so far, thanks to the novel material and device structure^[27].

Few researches on the electronic devices using 2D material-based hybrids were reported. A micro-sized electronic device using two dimensional topological insulators (Bi_2Se_3) grown on h-BN substrates was fabricated, from which exotic physical properties such as Shubnikov–de Haas (sdH) oscillation were observed under the strong magnetic field^[25]. An atomically clean interface between Bi_2Se_3 and h-BN played an important role to preserve the unique quantum states inherent in the topological insulator. On the other hand, conventional field-effect transistor was reported as well, using organic materials on h-BN. The device operated as normally-off, p-type transistor with high $I_{\text{max}}/I_{\text{min}}$ ratio of 10^6 . It should be noted that pre-patterned graphene layer was used as source and drain electrodes^[26].

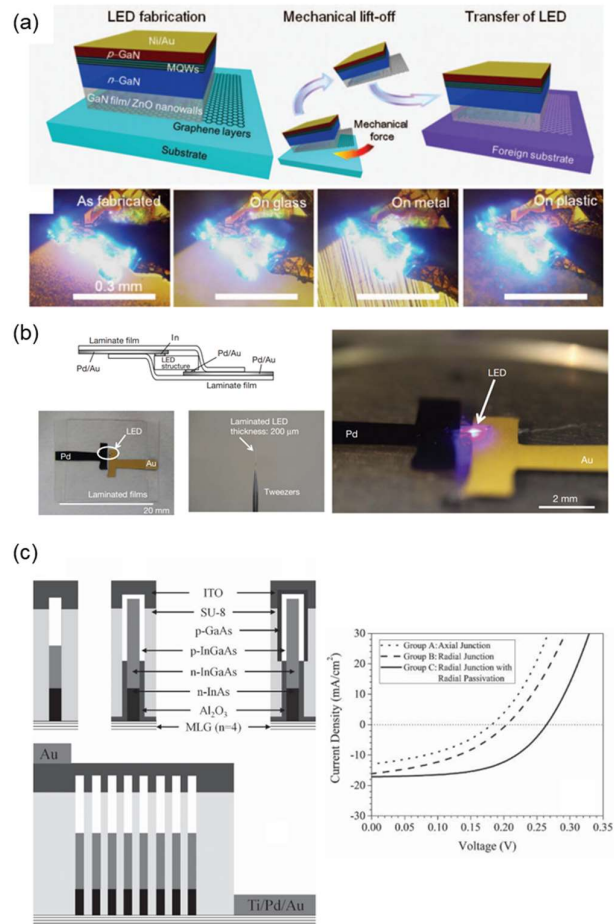


Figure 2.11 Functional optoelectronic devices fabricated using 2D nanomaterial based heterostructures^[20,24,27]. (a) Schematics of the fabrication and transfer process of LED on graphene layers, and their applications on different types of substrates. (b) Fabrication of vertical type LED using the released GaN thin films on h-BN layers. (c) Solar-cell applications of InAs/InGaAs nanowire heterostructures grown on graphene layers, and its open-circuit I - V characteristics with different device configurations.

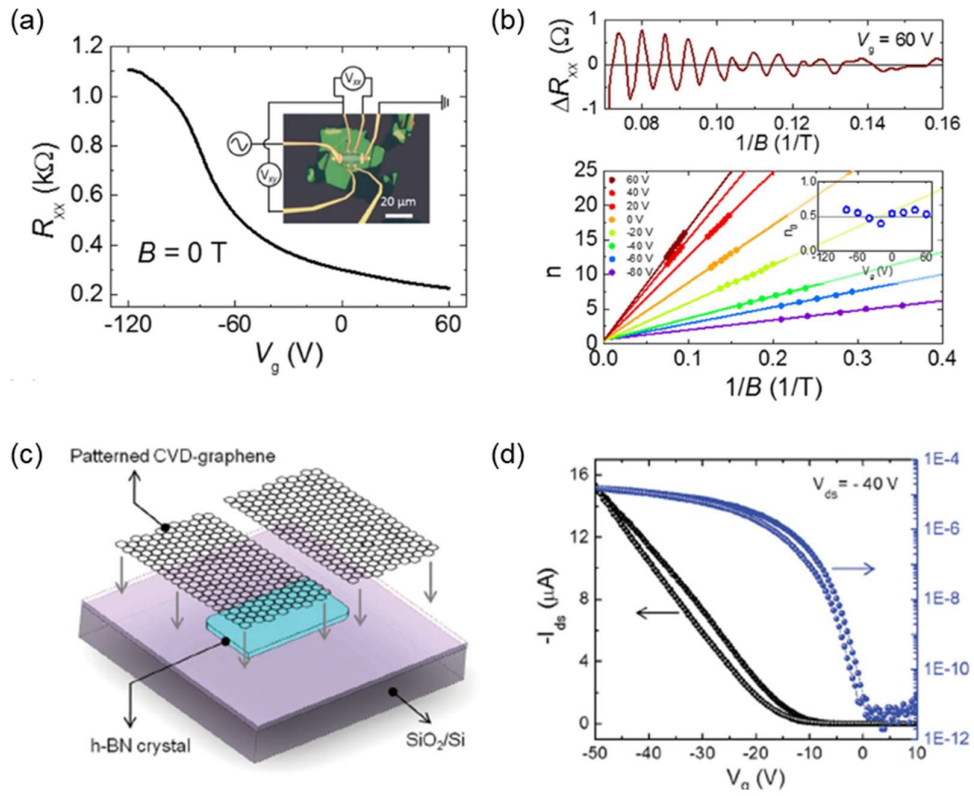


Figure 2.12 Electronic devices using h-BN based heterostructures^[25,26]. (a) Gate voltage dependence of the channel resistivity of the Bi₂Se₃ film grown on h-BN layers. (inset) A photograph of the fabricated device. (b) (top) Amplitude of SdH oscillations vs 1/B at V_g = 60 V and (bottom) Landau fan diagram of the peaks from TSS at the Bi₂Se₃/h-BN interface. (c) Strategy of preparing the h-BN crystal substrates with pre-patterned CVD graphene electrodes for the fabrication of the Rubrene/h-BN field-effect transistor. (d) Transfer characteristics of the Rubrene/h-BN field-effect transistor.

3. Experimental methods

3.1. Chemical vapor deposition (CVD)

3.1.1. CVD growth of large-scale h-BN layers

Polished $10 \times 10 \text{ mm}^2$ or $20 \times 20 \text{ mm}^2$ Ni(111) single crystals were purchased from commercial vendors. The substrates were further chemical-mechanical polished by a commercial polishing service in order to obtain a smooth surface. The root-mean-square (rms) surface roughness value scanned over an area of $5 \times 5 \text{ }\mu\text{m}^2$ was 3 nm. The smooth surface of the substrates is important for the preparation of high quality h-BN films because rough surface of the as-received Ni crystals contains grains with unwanted crystal orientations. An ammonia-borane solid precursor and the Ni(111) crystal were loaded in each heating zone of a two-zone furnace in an atmospheric pressure chemical vapor deposition (APCVD) system (Fig. 3.1a). Temperatures of each zone were carefully chosen to precisely control the sublimation rate of ammonia-borane and the growth of h-BN film (Fig. 3.1b). A mixture of high purity argon and hydrogen (800/200 sccm of Ar/H₂ flow, respectively) were flown in the reactor to purge the gas inside. The Ni(111) single crystal was heated up to 800–1030°C for 1 hour, after which ammonia-borane was heated up to 90–100°C for slow sublimation. The Ar/H₂ gas flow remained at 800/200 sccm during the growth. After 1 hour of growth, the furnace was cooled

down naturally to room temperature.

The h-BN films grown on the Ni(111) substrates were transferred by an electrochemical delamination method. For the film transfer, poly(methyl methacrylate) (PMMA) was spin-coated on the h-BN/Ni(111) stack at 4,000 rpm for 1 minute, and baked at 180°C for 1 minute. Then, a Ni foil and the PMMA/h-BN/Ni(111) stack were connected to the anode and cathode of a DC power supply, respectively. Both electrodes were dipped into a 0.1 M NaOH solution. Then a bias voltage of 10 V with a current of 0.3–1.0 A was applied during this process. The PMMA/h-BN films were slowly separated from the Ni(111) surface by hydrogen bubbles. After the PMMA/h-BN was completely detached, the floating films were transferred to deionized water for rinsing, and then finally transferred to SiO₂/Si or quartz substrates for further characterization. After drying the films at room temperature, the PMMA layers were dissolved in acetone. On the other hand, the Ni(111) substrates were cleaned by sonication in acetone and isopropanol after the delamination to grow more h-BN films.

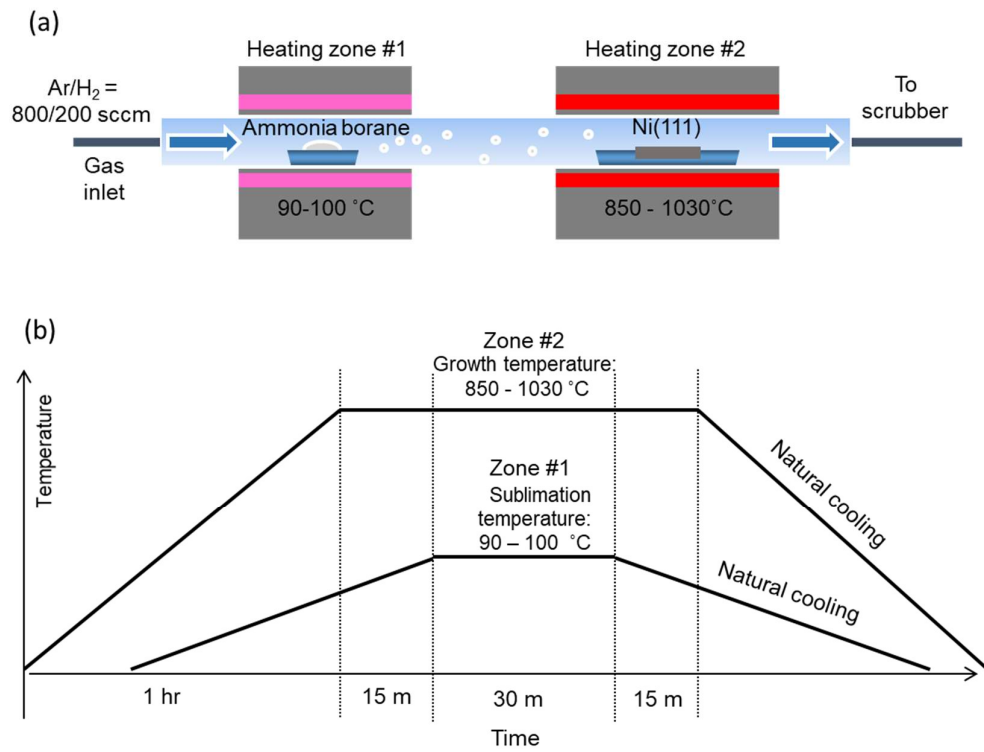


Figure 3.1 Experimental procedure of the synthesis of large-scale h-BN layers. (a) Schematics of the experimental growth set-up. (b) Detailed growth procedure.

3.1.2 Cold-wall CVD growth of h-BN

Ultrathin micropatterns and films of h-BN were grown on graphene layers using a cold-wall chemical vapor deposition (CVD) system. In this type of system, the graphite susceptor is heated remotely by a surrounding induction coil while the chamber wall is kept cold. Compared with the conventional hot-wall CVD system where the entire volume of the chamber is heated, the cold-wall CVD system allows chemical reactions to take place only on the hot surface of the susceptor and thus prevent unwanted pre-reactions and the incorporation of impurities generated from the heated inner wall of the chamber. Borazine, which has a 1:1 stoichiometric ratio of boron and nitrogen, was used as the precursor to h-BN and was transported as a vapor into the reaction chamber. To suppress the high vapor pressure of borazine and maintain a constant flow rate, a borazine-filled container was thermostatted at -15°C . High-purity nitrogen carrier gas was introduced at a flowrate of 8 sccm through a bubbler into the chamber to deliver gaseous borazine. The chamber had a continuous supply of ammonia and nitrogen during the growth process at 300 and 2000 sccm, respectively. The pressure inside the chamber was maintained at ca. 650 Torr during the growth process, the substrate was heated to 1130°C , and the growth time ranged from 10 to 60 min.

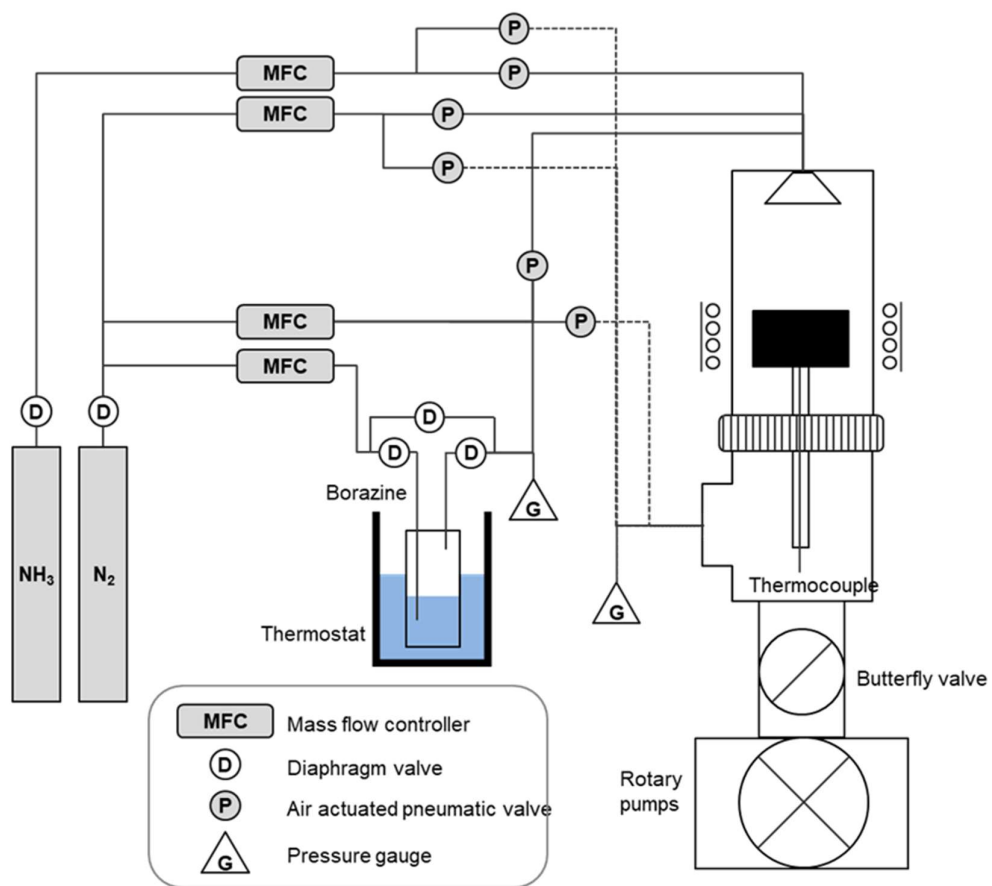


Figure 3.2 Schematics of the cold-wall CVD system for the growth of h-BN.

3.1.3. Growth of CVD large-scale graphene layers

Large-scale, multi-layered graphene films were synthesized on Cu foils using the CVD method. High-purity methane (CH₄) was used as a precursor to the graphene, and high-purity hydrogen (H₂) was used as the ambient gas. The graphene film was grown at 1,030°C for 2 h. During the growth period, the flow rates of CH₄ and H₂ were held constant at 10 and 100 standard cubic centimeters per minute (sccm), respectively. The reactor pressure was maintained at 220 Torr. The Cu foil was removed with ammonia persulfate, then the grown graphene films were transferred onto the Si substrate.

3.2. Metal-organic vapor-phase epitaxy (MOVPE)

3.2.1. MOVPE growth of ZnO nanostructure

ZnO nanostructures were grown on h-BN or graphene by metal-organic vapor-phase epitaxy (MOVPE). High-purity diethylzinc (DEZn) and oxygen (99.995%) were used as precursors for zinc and oxygen, respectively. For the ambient and carrier gas, high-purity argon (99.999%) was used. The flow rates of DEZn and O₂ were 20 and 100 sccm, respectively. To prevent the oxidation of h-BN layers, DEZn was first introduced into the reactor followed by the O₂. The growths was typically performed at a growth temperature of 500–700°C and a

reactor pressure of ~ 3.0 Torr for 60 min.

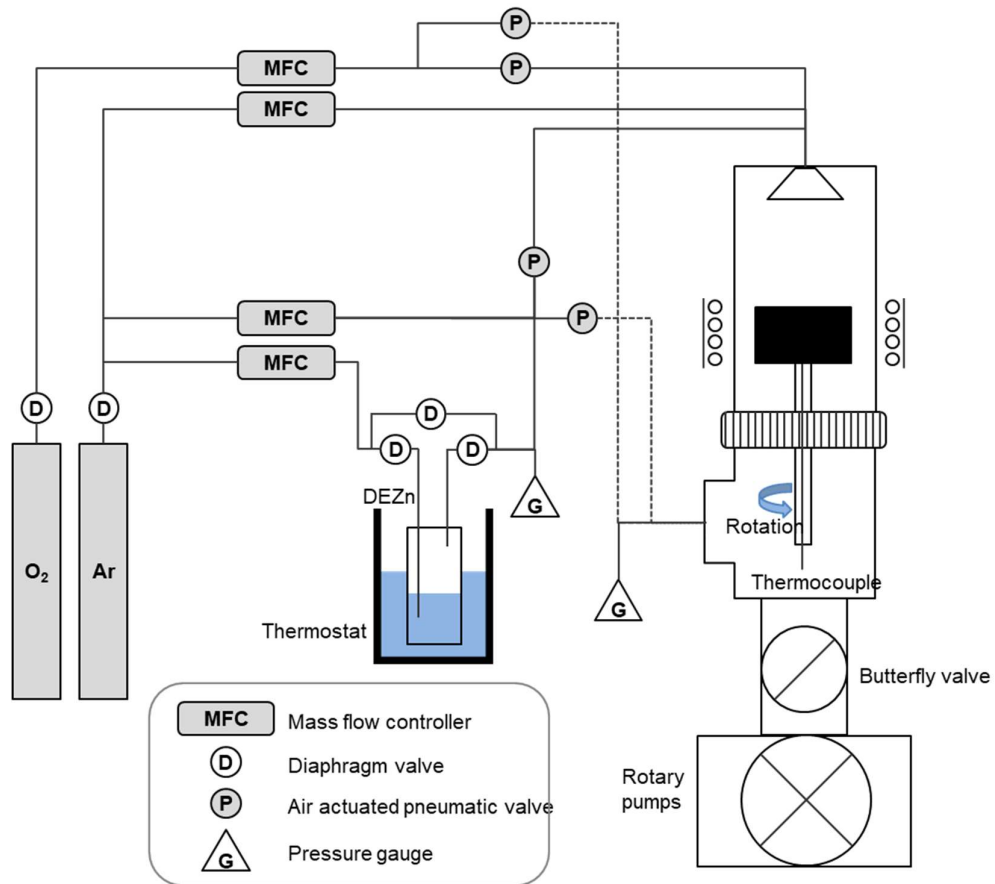


Figure 3.3 Schematics of the MOCVD system for the growth of ZnO nanostructures.

Table 3.1. Summary of precursors and gases used in the growth of h-BN, graphene using CVD system, and ZnO using MOCVD system.

Precursors	Purity (%)	Vapor pressure (K)	Company	System
		$\text{Log}_{10}P$ (torr) =		
DEZn	Electronic grade	$8.208-2109/T$ (K)		MOCVD
O ₂	99.9995+ %	–	–	MOCVD
Ar	99.9999+ %	–	–	MOCVD
Borazine	–	–	Planar materials	CVD
NH ₃	99.999+%	–	–	CVD
N ₂	99.9999+%	–	–	CVD
H ₂	99.9999+%	–	–	CVD

3.3. Transmission electron microscopy (TEM)

For the structural characterization, transmission electron microscopy was used; specifically, Tecnai F20 for selective area electron diffraction (SAED) pattern mapping, JEM-2100F equipped with ASTAR (NanoMEGAS SPRL) for electron back-scattered diffraction (EBSD) analysis and Titan 80-300TM (FEI) for high resolution imaging and analysis. Cross-sectional TEM samples were prepared by focused ion beam technique.

3.4. X-ray diffraction (XRD) study

3.4.1 XRD study for the characterization of thin films

X-ray diffraction (XRD) analyses, including theta-2theta ($\theta-2\theta$) scan, rocking-curve and azimuthal angle (ϕ) scan have been carried out at Research Institute of Advanced Materials in Seoul National University. D8-Advance Bruker Miller Co. was used. The X-ray wavelengths from Cu K- α was 1.5406 Å.

3.4.2 Synchrotron radiation XRD analysis

Synchrotron radiation x-ray diffraction (SR-XRD) analyses, including theta-2theta ($\theta-2\theta$) scan, grazing incidental diffraction (GID), reciprocal lattice mapping (RSM) and azimuthal angle (ϕ) scan have been carried out at 5A beamline of

Pohang Acceleration Laboratory in Korea. The X-ray wavelengths used for SR-XRD were 0.693 Å for θ - 2θ and ϕ scans, and 1.071 Å for GID measurements and RSM analysis. The measurements at different x-ray wavelengths were carried out in separate XRD facilities.

Table 3.2 Typical parameters in bench-top XRD and SR-XRD analysis

Parameters	Bench-top XRD	SR-XRD
		(5A beamline in PAL)
Source	Cu K α	Synchrotron radiation
Wavelength	1.5406 Å	1.071 Å
Energy	-	5 – 16 keV
Intensity	-	$\sim 10^{13}$ photons/sec
Resolution ($\Delta E/E$)	-	10^{-4}

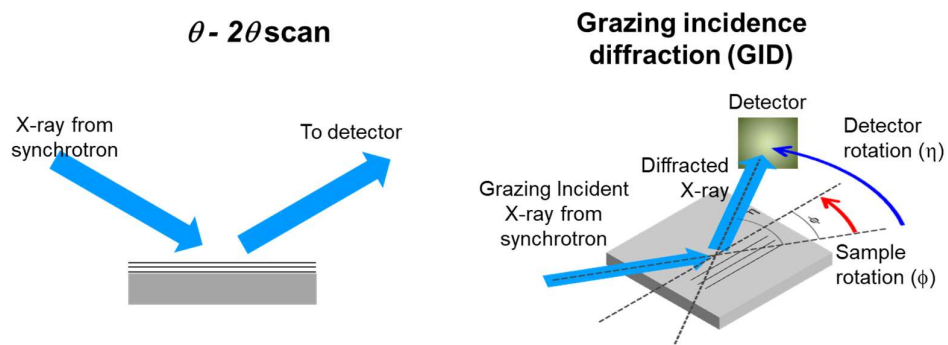


Figure 3.4 Schematic illustration of (left) conventional θ - 2θ scan and (right) grazing incidence diffraction (GID).

3.5. Fabrications of nano- and micro-devices

3.5.1. Fabrication of vertical field-effect transistor using ZnO nanotubes

The first step to fabricate the VFETs is to spin-coat the first polyimide (PI) layers on ZnO nanostructures at 4,000 rpm for 1 min and to cure at 300°C in nitrogen for 3 min. This acted both as a spacer between the gate and the source, and as the gate dielectric. Subsequently, the thickness of the PI layer was controlled to be 600 nm by O₂ plasma etching. The gate electrode patterns were then fabricated by electron-beam lithography, followed by a conformal deposition layer of Au with a thickness of 70 nm. The Au/PI/ZnO nanotubes were spin-coated by PMMA 950K (11 %) and only PMMA on the upper part of Au electrode was removed by O₂ plasma treatment. The exposed Au layer to air was selectively removed using a potassium iodide solution (KI, I₂ and DI water in the ratio 4 g : 1 g : 40 mL). After the gate electrode fabrication, another PI layer was coated at 4000 rpm for 1 min and thermally cured at 300°C in nitrogen for 3 min. The tips of the ZnO nanotubes were then exposed to air by O₂ plasma treatment. The drain electrode patterns were made by electron beam lithography, followed by conformal deposition of a Ti/Au (20/60 nm) layer using an e-beam evaporator. Finally, we removed the second PI layer from the top of the gate electrode by exposing the wafers to O₂ plasma at 50 W for 15 min at an O₂ partial pressure of 100 mT.

We transferred the ZnO nanotubes onto foreign substrates using a mechanical lift-off process. Before transfer, we coated the samples with a thick layer of PMMA by spin-coating them with PMMA 950K (11%) at 4,000 rpm for 1 min. We protected the samples from damage during transfer by baking them on a hot plate at 180 °C for 1.5 min. To support the device mechanically during the lift-off process, 5-mm-wide PI adhesive tapes were attached at the all edges of the sample. A small mechanical force was sufficient to detach the samples from the Si substrates. A metal bi-layer of Cr/Au (10/20 nm) was deposited onto the graphene film side of the free-standing device using an e-beam evaporator. Following the deposition of the metal layer, the samples were transferred onto the target substrates (usually PE or polyethylene terephthalate [PET]). Finally, the PMMA layer on the device was completely removed by dipping the sample in the acetone bath for more than 30 min.

Table 3.3 Typical process conditions for fabrication of flexible VFET using ZnO nanotubes grown on graphene layers.

Fabrication steps	Process conditions
1.1. Spin coating of 1 st polyimide layer	VTEC-Polyimide (No dilution), 4000 rpm 60 sec, pre-baked on 120°C hot-plate for 3 min
1.2. Curing	Rapid thermal annealing, N ₂ , 200°C (ramping for 3 min) for 3 min and 300°C (ramping for 3 min) for 3 min.
1.3. Etching for partial exposure	O ₂ plasma, 100 mT, 50 mA, 5 min
2.1. Patterning	E-beam lithography. Resist: PMMA 950K 11%, 4000 rpm,
2.2. Deposition of gate electrodes	thermal evaporator, sample rotation 10–12 rpm, Au 120 nm (Sample tilted)
2.3. Lift-off	Acetone bath > 30 min
2.4 Etch-masking layer coating	PMMA 950K 5%, 4000 rpm, baked on 180°C hot-plate for 1 min
2.5 Etching for tip exposure	O ₂ plasma, 100 mT, 50 mA, 5 min
2.6. Selective etching	KI/I ₂ /DI water 1:1:40 mixed gold etchant solution. 30 sec. CF ₄ (mixed with Ar/O ₂) plasma etching is also possible.
2.7. Etch-mask removal	Acetone bath > 30 min
3.1. Spin coating of 2 nd polyimide layer	VTEC-Polyimide (No dilution), 4000 rpm 60 sec, pre-baked on 120°C hot-plate for 3 min
3.2. Curing	Rapid thermal annealing, N ₂ , 200°C (ramping for 3 min) for 3 min and 300°C (ramping for 3 min) for 3 min.
3.3. Etching for partial exposure	O ₂ plasma, 100 mT, 50 mA, 5 min
4.1. Patterning	E-beam lithography. Resist: PMMA 950K 11%, 4000 rpm,

- 4.2. Deposition of gate electrodes thermal evaporator, sample rotation 10–12 rpm, Ti/Au 30/50 nm (Sample tilted)
- 4.3. Etch-mask removal Acetone bath > 30 min
-

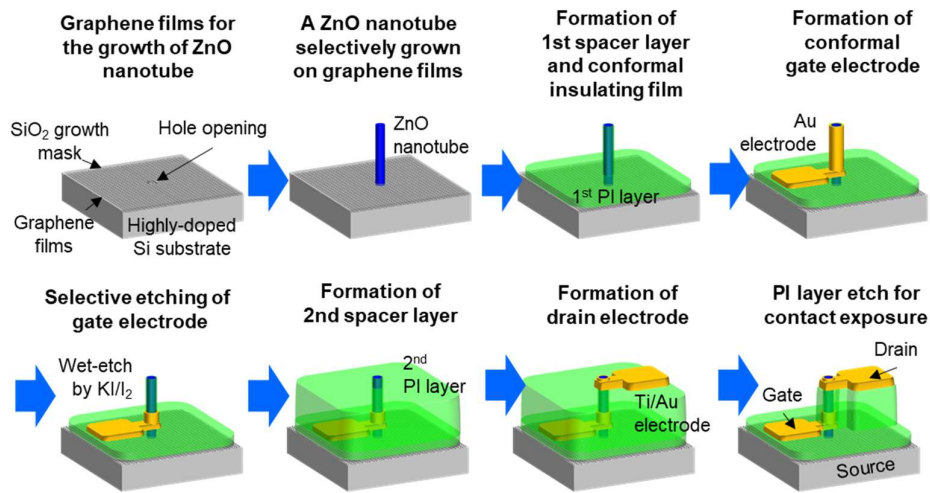


Figure 3.5 Schematic diagram of the process used to fabricate the vertical field effect transistor (VFET) arrays using the ZnO nanotube heteroepitaxially grown on graphene layers.

3.5.2. Fabrication of flexible UV sensors using ZnO/h-BN hybrid materials

First, gaps between each ZnO nanowall-networks were filled with PI layers. Liquid PI solution was spin coated then baked onto hot plate at 120 °C. Post-curing process was done in rapid thermal annealing chamber at 200 °C for 3 min and 300 °C for 3 min. Then PI layers were dry etched by oxygen plasma to expose the tip of ZnO nanowall network arrays. The finger-tip shaped electrode patterns were formed by e-beam lithography. The length and spacing of each pattern was varied by purposes. 100 nm of Au electrodes were deposited by e-beam evaporator and lift-off process was followed in acetone bath.

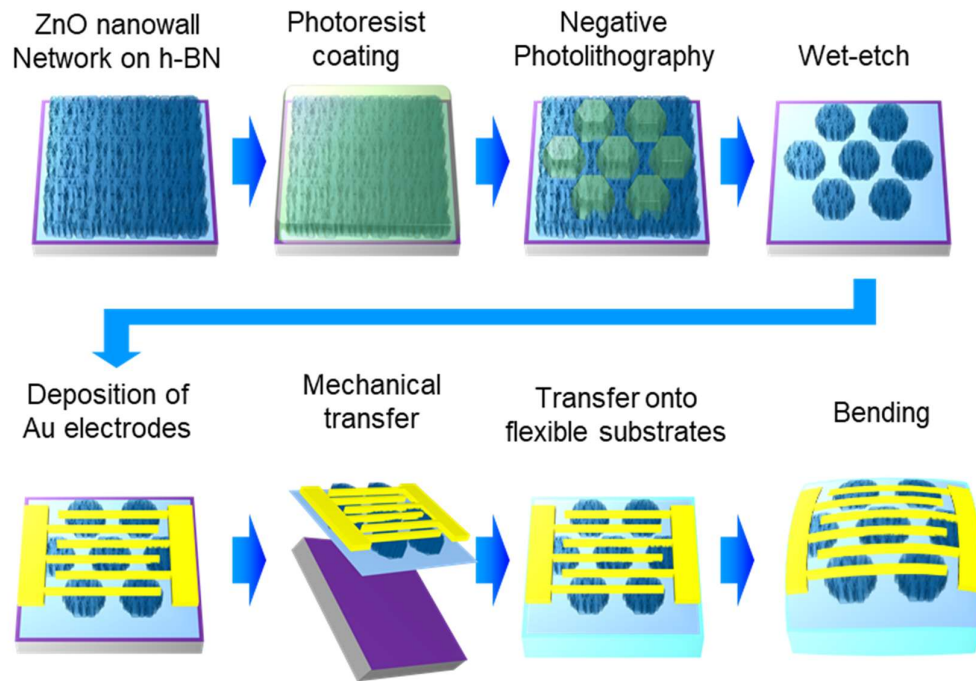


Figure 3.6 Schematic diagram of the process used to fabricate the flexible UV sensors using ZnO nanowall networks on h-BN substrate.

Table 3.4 Typical process conditions for fabrication of flexible UV sensor

Fabrication steps	Process conditions
1.1. Photolithography	Photoresist AZ5214, spin coating 4000 rpm, 90°C hot-plate 60 sec bake
1.2. ZnO wet etch	30% acetic acid, 30 sec
1.3. Resist removal	Acetone bath > 5 min
2.1. Spin coating of polyimide layer	VTEC-Polyimide (No dilution), 4000 rpm 60 sec, pre-baked on 120°C hot-plate for 3 min
2.2. Curing	Rapid thermal annealing, N ₂ , 200°C (ramping for 3 min) for 3 min and 300°C (ramping for 3 min) for 3 min.
2.3. Etching for partial exposure	O ₂ plasma, 100 mT, 50 mA, 5 min
3.1. Metallization	thermal evaporator, sample rotation 10–12 rpm Au 50 nm
3.2. Patterning	Photoresist AZ5214, spin coating 4000 rpm, 90°C hot-plate 60 sec bake
3.3 Selective wet-etch	KI/I ₂ /DI water 1:1:40 mixed gold etchant solution. 30 sec.
3.4 Resist removal	Acetone bath > 5 min

3.6. Electrical characterizations

The electrical characteristics of FETs, including the current–voltage (I_{ds} – V_{ds}) and transfer (I_{ds} – V_g) characteristic curves, were measured using a semiconductor analyzer (Keithley 4200). The characterizations were carried out under dark condition to remove any photocurrent effect in ZnO nanotube channels. The drain currents are normalized by the outer diameter of the gate, that is, channel width.

3.7. DFT calculation

A first-principles calculation based on density-functional theory (DFT) was performed using the Vienna ab initio simulation package (VASP)^[28] to study the electronic structures of the ZnO/BN heterostructure. We used the Perdew–Burke–Ernzerhof (PBE)^[29] functional based on the generalized gradient approximation (GGA) for the exchange–correlations and projector augmented-wave (PAW) method for descriptions of core electrons. The DFT-D2 method of Grimme^[30] was also used to consider London dispersion interactions between the ZnO and BN sheet. Plain-wave basis sets were used with a plain-wave cutoff of 500 eV. Brillouin-zone integrations were performed on a grid of $2 \times 2 \times 1$ Monkhorst-Pack special points. To model the ZnO/BN heterointerface, we used the $3 \times 3 \times 2$ ZnO on the 4×4 BN sheet with a vacuum region larger than 15 Å. The topmost O layer was passivated with hydrogen atoms. Because the slab system was asymmetric along the z direction,

a dipole correction was considered. All atoms were relaxed by the conjugate gradient method until none of the remaining Hellmann-Feynman forces acting on any atoms exceeded 0.03 eV \AA^{-1} .

3.8. Other characterization

Physical characteristics of h-BN films were further investigated using Raman spectrum mapping, optical microscopy, Atomic force microscopy (AFM), ultraviolet-visible-infrared (UV-Vis-IR) spectroscopy transmittance measurements, and X-ray photoelectron spectroscopy (XPS). The Raman spectra were measured using a spectrometer with a focal length of 460 mm and a wavelength of 514.5 nm of an Ar-ion laser as an excitation source. Raman mapping was performed in a $10 \text{ }\mu\text{m} \times 10 \text{ }\mu\text{m}$ region with a step size of $0.2 \text{ }\mu\text{m}$. The absorption spectra were investigated using UV-Vis-IR spectroscopy. h-BN films transferred on quartz substrates were used to investigate the absorbance curve. To extract the optical band gap of h-BN layers, the absorbance curve of the h-BN film was converted to Tauc's plot based on Tauc's equation.^[4] The chemical compositions of the films were determined by XPS. Before the XPS measurements, h-BN films were transferred onto SiO_2/Si substrates. XPS measurements were carried out under ultra-high vacuum (UHV) condition (5×10^{-9} torr) using $\text{Mg-K}\alpha$ x-ray as an excitation source.

4. Growths of large-scale and single-crystalline 2D nanomaterials

4.1. Introduction

Hexagonal boron nitride (h-BN) is a dielectric insulator with a two-dimensional (2D) layered structure. It is an appealing substrate dielectric for many applications due to its favorable properties, such as a wide band gap energy of 5.6–6.0 eV, chemical inertness of the surface, and high thermal conductivity^[31–33]. Furthermore, its remarkable mechanical strength makes it possible to use few-layered h-BN as a flexible and transparent substrate, ideal for next-generation electronics and optoelectronics in applications such as flexible and transparent transistors or light-emitting devices^[20,24,34–36]. However, the difficulty of preparing high quality large-area h-BN films has hindered their widespread use. While exceptionally clean and ordered h-BN layers can be prepared by mechanical cleavage methods from bulk crystals^[4,24], their limited sizes and random thicknesses and orientations are not suitable for practical device applications. On the other hand, large-area h-BN layers prepared by chemical vapor deposition (CVD) usually exhibit polycrystalline structures with a typical average grain size of several microns^[3,4,13] or tens of microns^[5,9]. Grain boundaries or dislocations in polycrystalline h-BN can affect its electronic or mechanical properties, resulting in

a lower band gap energy, higher leakage current, and poorer mechanical strength^[37–40]. Accordingly, large-area single crystalline h-BN layers are desired to fully realize the potential advantages of h-BN in device applications. To this end, efforts on controlling sizes and directions of individual domains of h-BN have been reported^[5,8,9,41], yet obtaining large scale single crystalline h-BN films is still challenging. Here, we report the synthesis of epitaxial h-BN films in centimeter scale, while maintaining a low cost of production by re-using the Ni(111) substrates via electrochemical delamination.

The use of Ni(111) for heteroepitaxial growth of h-BN has been previously reported^[10,42,43], in particular for obtaining monolayer h-BN on Ni(111)^[10,42]. In those previous studies, substrates were heated in an ultra-high vacuum chamber and exposure to the borazine vapor resulted in forming a h-BN layer. Similarly, Ru(0001), Rh(111) substrates were also employed as the substrates to grow h-BN layers heteroepitaxially^[11]. However, such epitaxial h-BN films were hard to be separated from the original substrates without consuming them, so further characterizations and applications were limited. In this work, h-BN layers were separated using an electrochemical delamination technique and Ni(111) were reusable. Furthermore we investigated microstructural characteristics of the free-standing h-BN films.

4.2. Heteroepitaxial growth of epitaxial h-BN on Ni(111)

The h-BN films were grown on Ni(111) single crystal substrates by APCVD and transferred onto arbitrary substrates as schematically illustrated in Figure 4.1a. Before the growth of h-BN films, the surface of Ni(111) substrates was polished by chemical-mechanical planarization, after which Ni(111) could be repeatedly re-used. Then, a two-zone furnace system with a single ammonia-borane solid precursor was used to grow h-BN films on the Ni substrates. The as-grown h-BN films were spin-coated with PMMA and then transferred to foreign substrates using the electrochemical delamination method^[13,44]. The transferred h-BN films can easily be identified by the naked eye, as shown in Fig. 4.1b. The size of the h-BN films is limited by that of the Ni(111) substrate; in this work, we report h-BN films as large as $20 \times 20 \text{ mm}^2$ (maximum size of commercially available Ni(111)). After the transfer process, Ni(111) substrates were cleaned and re-used repeatedly to grow additional h-BN films. Detailed procedures are described in the methods section.

The morphology of the repeatedly obtained h-BN films and the reliability of the growth and transfer processes were first investigated using optical microscopy. The optical microscope images of h-BN films transferred on SiO₂/Si substrates are shown in Fig. 4.1c. Over the entire scope of the image, h-BN films exhibit a uniform color contrast difference to the SiO₂/Si surface, which indicates

that the thickness of the h-BN films is uniform to nanometer scale over the entire region^[45]. This uniform growth of h-BN films on Ni(111) single crystal substrates is in strong contrast to that on a poly-crystalline Ni foil, whose resulting films grown with the same growth conditions show multiple patches of h-BN of varying thicknesses. Considering the dissimilar growth rate of h-BN on different crystal plane orientations of the nickel substrate, the uniform thickness of h-BN films on Ni(111) results presumably from the single crystallinity of the substrate^[46,47]. In addition, as shown in Fig. 1c, the same optical contrast was observed from the 1st, 5th, and 10th grown and transferred h-BN, indicating that the h-BN films with a uniform thickness were repeatedly obtained.

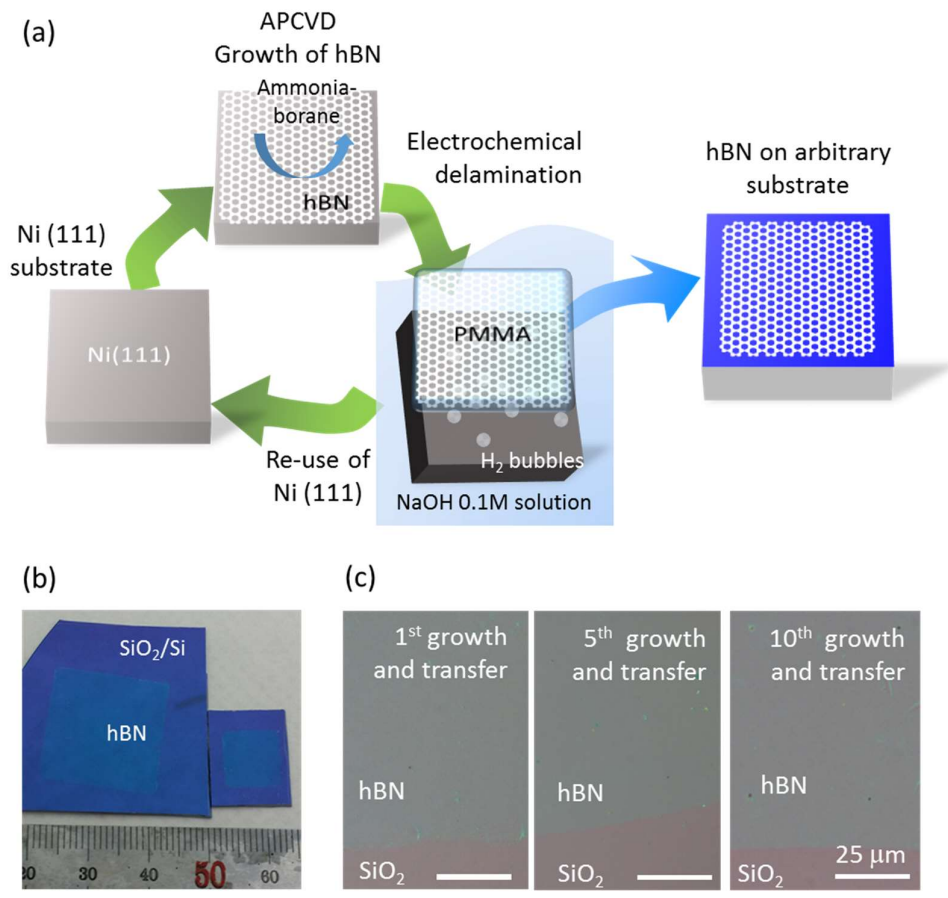


Figure 4.1 Repeated growth and transfer of h-BN films using Ni (111) single crystal substrate. (a) Schematic illustration of the experiment. (b) h-BN films transferred onto SiO₂/Si substrates. (c) Optical microscope images of h-BN films on SiO₂/Si substrates obtained from the same Ni (111) substrate with different number of usage.

The crystal structure and surface morphology of Ni(111) were examined by SEM-EBSD and AFM between repeated growth and transfer processes in order to confirm that the Ni(111) substrates can be reliably re-used. Fig. 4.2a shows the inverse pole figure (IPF) color map images of SEM-EBSD for a Ni(111) substrate after the 1st and 10th growth and transfer processes, respectively. In the IPF color map after the 1st growth and transfer, the whole surface exhibited the same blue color in normal direction(ND) and green color in transverse direction(TD), indicating that the whole region is oriented in the (111) direction. The IPF color map after 10th growth and transfer was almost identical, suggesting that the crystal structure of the Ni(111) substrate remained the same in this region after multiple growth and transfer processes, without forming additional disoriented grains at elevated temperatures during h-BN growth. In addition, as shown in Fig. 4.2b, even after 10 cycles of repeated growth and transfer processes, there were no significant change in the film surface morphology: the atomic terraces remained largely identical and no significant increase in surface roughness was observed. Both the EBSD and AFM studies on the Ni(111) substrate strongly suggest that the crystal structure and surface morphology of Ni(111) substrates were not affected by the repeated growth and transfer processes.

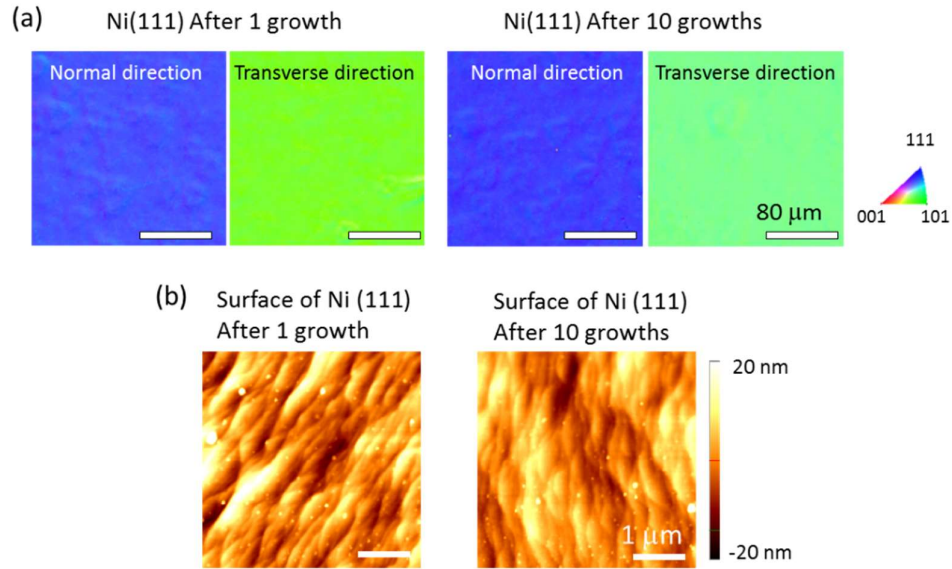


Figure 4.2 Changes of the Ni(111) substrates after multiple growths of the epitaxial h-BN layers. (a) EBSD IPF maps of the Ni (111) substrate in the normal direction (ND) and the transverse direction (TD), after 1 and 10 growths. (b) AFM image of Ni(111) substrate (a) after 1 and 10 growths.

4.3. Growth behavior of h-BN on Ni(111)

We investigated the effects of growth parameters including sublimation temperature of the ammonia-borane precursor and film growth temperature on the characteristics of h-BN films (Fig. 3.1b). Figure 4.3a and b shows the resulting changes in thickness, coverage, and crystallinity of the h-BN films grown at the various ammonia-borane sublimation temperatures of 90–100°C. The temperature of the zone #2 was kept to 875°C. The films grown with sublimation temperatures of 90 and 93°C exhibited incomplete coverage (Left in Fig. 4.4a) over a large area and very small increase in the thickness from 2.5 to 3 nm. However, the films with a sublimation temperature of 95°C showed sufficient area coverage (Fig. 4.3a, inset) and a clear dot pattern in the SAED image (left in Fig. 4.3b), and hence we used this temperature for all other analyses in this work. On the other hand, when the sublimation temperature was increased to 97 and 100°C, the thickness increased dramatically to 20 and 50 nm, respectively. However, these thick films exhibited distinct ring patterns in the SAED image resulting from randomly oriented crystal structures (right in Fig. 4.3b), and thus were less crystalline than the 95°C sample. Based on these results, it is very important to carefully control the sublimation temperature of ammonia-borane to obtain a full-coverage, few-layered film of high crystallinity. It should be noted that by increasing the growth time from 30 min to 3 hr, complete coverage was achieved even at a low sublimation temperature of 93°C as shown in the right of Fig. 4.4a. Likewise, the growth temperature in zone

#2 also played a role in controlling growth, albeit less critically. The temperature of the zone #1 was kept to 95°C. An adequate growth temperature range in our system was found to be 875–950°C, while a low temperature of 800°C resulted in slow growth and low coverage, and a high temperature of 1030°C resulted in faster growth but with unsatisfactory crystallinity (Fig. 4.4b). It is noteworthy that polycrystalline structure of 1030°C grown h-BN can also result from unwanted heating due to radiation from zone #2, because the crystallinity and thickness are very sensitive to the ammonia-borane sublimation temperature.

The effect of varying the cooling rate was also investigated to clarify the governing growth mechanism. The cooling rate of the substrate was varied by opening the top cover of the chamber after finishing the growth, which increases the initial cooling rate from 10°C/min to >50°C/min. The temperatures of zone #1 and #2 were 95°C and 900°C, respectively. Generally, a precipitation-driven growth is expected to be strongly affected by the change in cooling rate, while a surface-mediated growth would be minimally affected^[6,48]. In our case, Fig. 4.3c shows that the film thickness, uniformity, and crystallinity were nearly identical for both fast and slow cooling, indicating that a surface-mediated growth was more likely. This is presumably attributable to the low dissolution rate of other reactants into the Ni(111) facet due to its low surface energy^[46].

The initial growth mode was investigated by reducing the growth duration. For this purpose, h-BN films with growth durations of 30 sec, 3 min, and 30 min were transferred to SiO₂/Si substrates and compared using optical microscopy (Fig. 4.3d). The growth of h-BN in our experiments appears to initiate from dense, multiple points on the Ni(111) surface, already covering a large percentage of the whole area even at 30 sec duration. This is in contrast to previous CVD works where individual grains with a low density grew larger to cover the entire film^[5,9,41]. As the growth time increases, each h-BN nuclei merged into several multi-layered h-BN patches, then films with complete coverage were finally formed (see Fig.4.5a and b). Nevertheless, a strong epitaxial relation between the h-BN film and the Ni(111) surface in our case presumably led to the formation of a single oriented h-BN film.

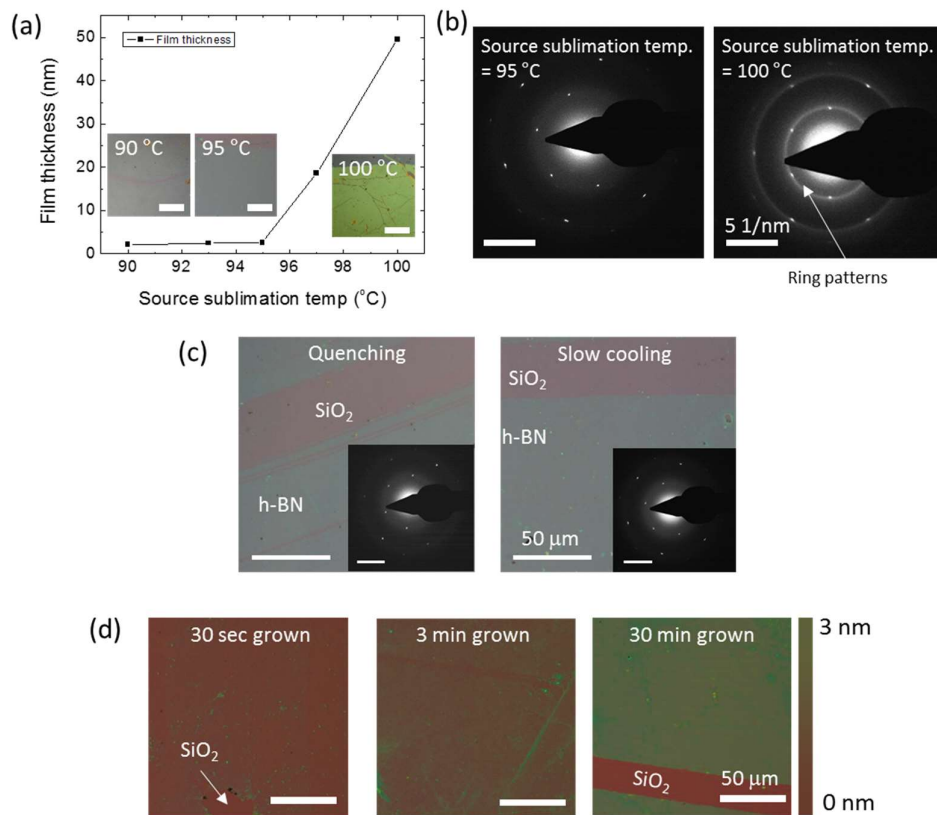


Figure 4.3 Growth behavior of h-BN film on Ni(111) using APCVD. (a) Thickness of h-BN films grown at different ammonia-borane sublimation temperatures. Inset are optical microscope images of the film on SiO₂/Si substrates. Scale bar: 50 μm. (b) SAED pattern of h-BN film with ammonia-borane sublimation temperature of 95°C and 100°C. (c) Optical microscope images of h-BN films with different cooling rates. Inset are corresponding SAED patterns of the h-BN films. Scale bar: 5 nm⁻¹ (d) High saturation optical microscope image of h-BN films transferred onto SiO₂/Si substrates with different growth time.

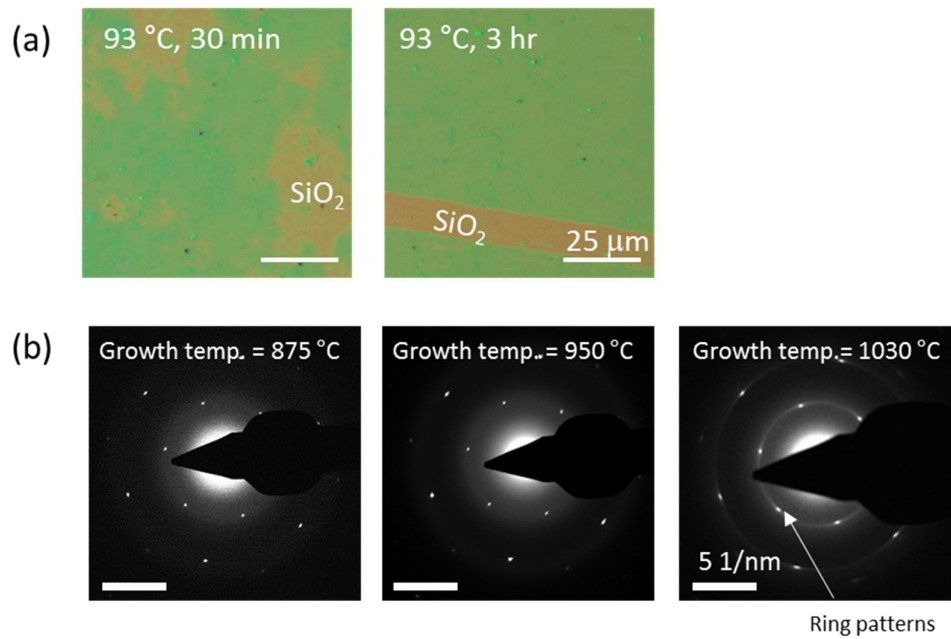


Figure 4.4 Growth behavior of h-BN films under different growth conditions. (a) High-saturation optical microscope images of h-BN films with ammonia-borane sublimation temperature of 93°C and growth time of 30 min and 3 hr. (b) SAED patterns of h-BN film grown under different growth temperatures, 875°C, 950°C and 1030°C.

To give more quantitative data, height profiles of h-BN films with different growth time was measured, as shown in Fig. 4.5a. At the initial growth stage (30 sec of growth), only nano-sized particles were observed, which are expected to be h-BN nano islands. As the growth time was increased to 3 min, the size of each h-BN islands increased, but not enough to form a complete film. When the growth time reached 30 min, h-BN films with full coverage were obtained. From this observation, we expect that h-BN islands were first formed, and then they merge to form thin films with full coverage. The expected growth mechanism is shown in Fig. 4.5b.

The precise growth mechanism of multilayer growth is unknown. However, it has been reported that the catalytic effect of the metal substrate can reach beyond the first layer to ca. 3 nm above the surface⁵. We believe the multilayer formation of h-BN films on Ni(111) in our APCVD growth can also be attributed to a similar mechanism. The poor crystallinity of thick h-BN film observed in Fig. 4.3b can be attributed to a non-catalytic growth mode due to the extended distance from the surface, while 3 nm thick h-BN films show only a single orientation.

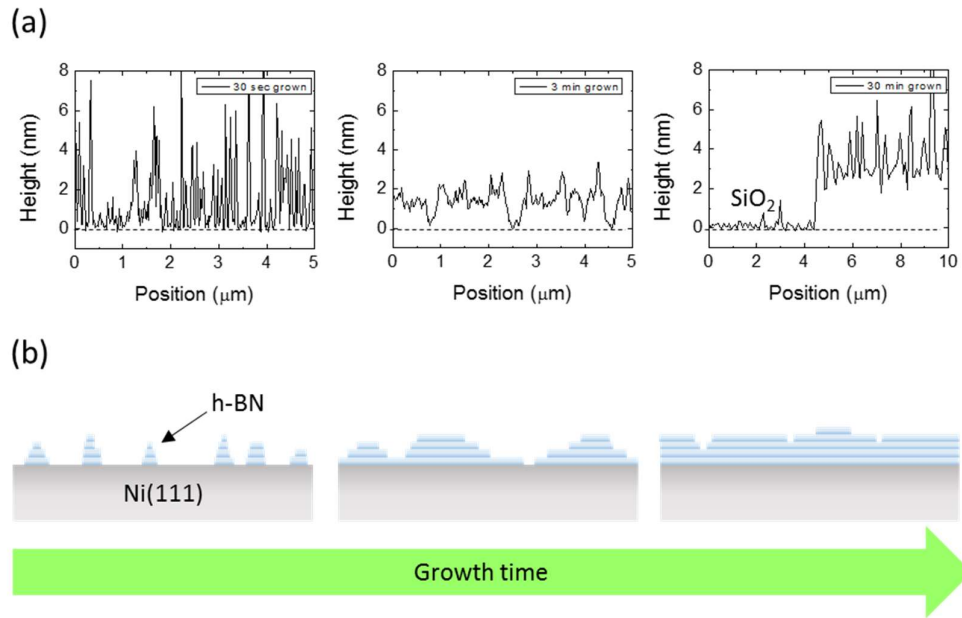


Figure 4.5 Initial growth stages of the epitaxial h-BN on Ni(111). (a) Height profile of h-BN films on SiO₂/Si substrate with different growth time (30 sec, 3 min and 30 min). (b) Proposed growth model of h-BN films on Ni(111).

4.4. Structural characteristics of epitaxial h-BN

The heteroepitaxial relationship and overall crystallinity of h-BN films on Ni(111) were investigated using SR-XRD. Figure 4.6a shows a θ - 2θ scan of as grown h-BN on Ni(111), showing peaks only from h-BN(0002) and Ni(111) planes. This indicates that the c -axis of the h-BN film is normal to the Ni surface plane. More importantly, we employed GID to verify the crystallinity along the in-plane direction. With a beam at an incident angle of 0.3° in our experiments, the area of the illuminated surface was $0.4 \times 10 \text{ mm}^2$, allowing a centimeter-scale investigation of the in-plane crystallinity. Figure 4.6b shows high resolution GID spectra of h-BN/Ni(111), taken at two different sample orientations separated by 30° from each other. Strong and sharp h-BN($10\bar{1}0$) peak was observed along the Ni $\langle\bar{1}\bar{1}2\rangle$ direction, with no other h-BN related peaks, indicating a well-ordered h-BN crystal with a single orientation through the whole surface interaction area. On the other hand, measurement along the Ni $\langle 10\bar{1}\rangle$ direction (*i.e.*, 30° rotation from Ni $\langle\bar{1}\bar{1}2\rangle$) exhibited peaks from h-BN($1\bar{1}20$) and Ni($20\bar{2}$), which are not clearly separated due to their very similar d -spacing values (1.252 \AA for h-BN($1\bar{1}20$) and 1.246 \AA for Ni($20\bar{2}$)).

The in-plane crystallinity of the h-BN films was further investigated by scanning XRD of the h-BN $\{10\bar{1}0\}$ peak as a function of the substrate angle (or azimuthal angle) ϕ . Due to the elongated surface footprint up to 10 mm, this ϕ -scan probes the distribution of in-plane crystal orientation over a wide centimeter-scale area. As shown in Fig. 4.6c, the resulting plot from as-grown h-BN on Ni exhibits diffraction peaks from h-BN $\{10\bar{1}0\}$ only at ϕ values of exact multiples of 60° , exhibiting a clear six-fold symmetry of h-BN. A small angular dispersion with a full width at half maximum (FWHM) value of 0.8° was observed. Furthermore, the θ - 2θ scan, GID, and ϕ -scan results were nearly identical after delaminating and transferring the h-BN film onto a SiO₂/Si substrate (Fig. 4.7).

We investigated the epitaxial relationship between the h-BN film and Ni substrate using reciprocal space mapping (RSM) of SR-XRD. Figure 4.6d shows a HK-mesh contour plot of the RSM exhibiting an exact overlap of two peaks originating from h-BN(11 $\bar{2}$ 0) and Ni(20 $\bar{2}$). The diffraction peak from Ni(20 $\bar{2}$) was sharp in Q_y -direction with its value matching well with known values (d -spacing of 1.246 Å or Q_y -value of 5.041 Å⁻¹), but spread out in Q_x -direction as commonly seen with other single crystal metallic substrates. On the other hand, the diffraction peak from h-BN(11 $\bar{2}$ 0) was situated at a larger Q_y -value than expected (d -spacing of 1.252 Å or Q_y -value of 5.019 Å⁻¹). Furthermore, while its spread in Q_x -direction

(estimated as a width at 10% maximum of 0.13 \AA^{-1} , corresponding to 1.5° spread in ϕ -scan) was in accordance with the FWHM seen in Fig. 4.6c, its spread in Q_y -direction was larger than that of the $\text{Ni}(20\bar{2})$ peak. These results strongly suggest that the $\text{h-BN}(11\bar{2}0)$ planes were compressed due to the strain from the $\text{Ni}(111)$ surface to form a heteroepitaxial relationship of $\text{h-BN}(11\bar{2}0) \parallel \text{Ni}(20\bar{2})$ (or $\text{h-BN}(10\bar{1}0) \parallel \text{Ni}(11\bar{2})$)^[43,49].

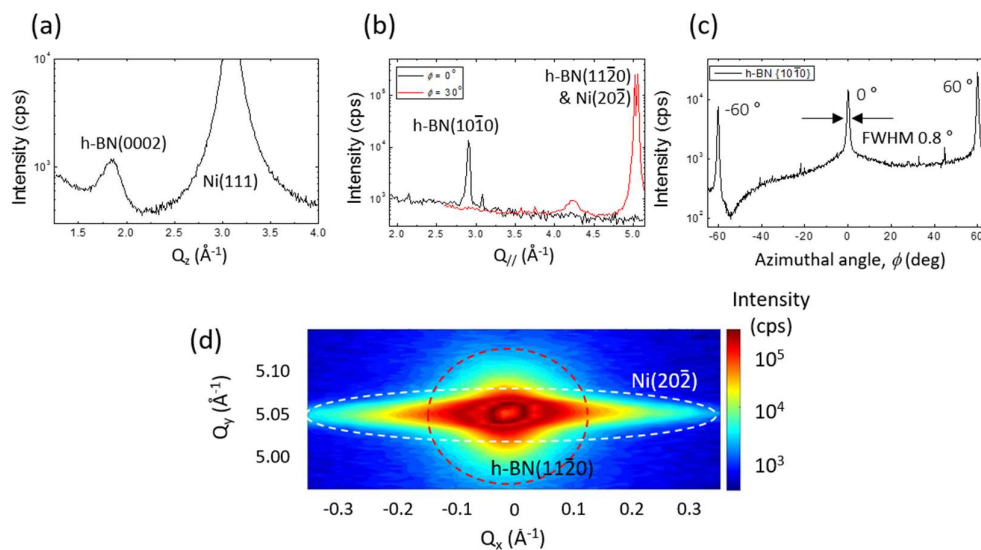


Figure 4.6 Synchrotron radiation x-ray diffraction (SR-XRD) profiles of h-BN film grown on Ni(111) substrate. (a) θ - 2θ scan of as grown h-BN/Ni(111). (b) Grazing incident diffraction (GID) profile of h-BN/Ni(111) with different x-ray azimuthal angles, separated by 30° . (c) Azimuthal angle(ϕ)-scan of h-BN{10-10} plane from as grown h-BN/Ni, showing six-fold symmetry. (d) HK mesh contour maps of reciprocal space mapping (RSM) around h-BN(11-20) and Ni(20-2) diffraction.

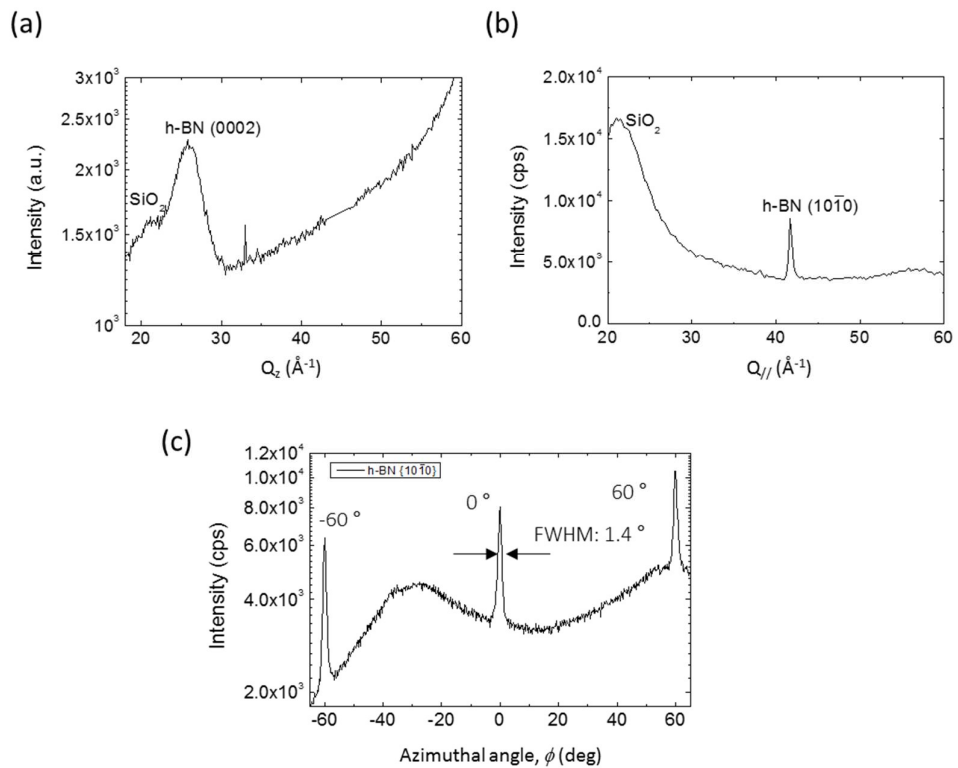


Figure 4.7 SR-XRD analysis of h-BN film transferred onto SiO₂/Si substrate. (a) θ - 2θ (θ - 2θ) scan, (b) GID profile along the direction of h-BN $\langle 10\bar{1}0 \rangle$. (c) Azimuthal angle (ϕ)-scan of h-BN {10 $\bar{1}$ 0} plane, showing six-fold symmetry even after transfer process.

The crystal structure and crystallinity of the h-BN film were further studied using SAED. Fig. 4.8a illustrated our SAED measurements at different positions distributed over a large area^[50]. As shown in the left image in Fig. 4.8b, first, the SAED measured with a 4.5- μm aperture clearly showed a single-oriented hexagonal crystal structure. Then, 16 SAED patterns were obtained in the same manner at different positions over a $0.3 \times 0.3 \text{ mm}^2$ area. The obtained images were overlapped into a single image (middle in Fig. 4.8b). Because all the patterns were almost identical, the overlapped image was almost the same as each individual pattern. This indicates that the SAED patterns originated from a single domain of h-BN over the $0.3 \times 0.3 \text{ mm}^2$ region. To investigate the crystallinity over an even larger area, nine SAED patterns were obtained at the center and corners of a $0.9 \times 0.9 \text{ mm}^2$ area, using a 20- μm aperture. The obtained pattern images were again overlapped into a single image (right in Fig. 4.8b). Similarly, no significantly different crystal orientations were observed, indicating that the SAED patterns still belonged to the same single domain of h-BN over the $0.9 \times 0.9 \text{ mm}^2$ area. Meanwhile, as the measurement area became wider, the dispersion of $(10\bar{1}0)$ spot increased from 2.9° to 4.4° , and then to 7.1° (left, middle, and right in Fig. 4.8b, respectively). This broadening may be attributed to the accidental folding of h-BN layers introduced during the wet transfer process.

Electron back-scatter diffraction accompanied by TEM (TEM-EBSD) allows for spatial mapping of the crystal orientation of h-BN in nanometer scale^[51]. In TEM-EBSD, nanometer-sized electron beam probe scans the specimen point-by-point, after which the crystal orientation mapping image is constructed using the electron diffraction pattern at each point (Fig. 4.8c). Fig. 4.8d shows the inverse pole figure (IPF) map with color legends over a $3 \times 3 \mu\text{m}^2$ area of a h-BN film, in normal direction (ND) and transverse direction (TD), respectively. The colors represent the crystallographic orientation with respect to each direction of the sample. In the left image in Fig. 4.8d, the entire region of the image is colored in red, which corresponds to the (0001) plane of the hexagonal structure of h-BN aligned to ND in the whole region of the image. The black points in the image are caused by the low signal-to-noise ratio, limited by the small thickness of the sample and integration time during scanning, which hinders determination of the crystallographic information within a desired accuracy. The IPF map in TD shown in the right image in Fig. 4.8d shows a similar result with the entire region of the image colored in green, which corresponded to the $(2\bar{1}\bar{1}0)$ plane of the sample aligned to TD.

The atomic structure of h-BN films was also investigated using HR-TEM, obtained by Cs aberration-corrected low acceleration voltage TEM (LVTEM). Figure 4.8e shows an HR-TEM image of an h-BN film, where the hexagonal

structure of h-BN layers can be clearly seen. The d -spacing value of the $(10\bar{1}0)$ lattice planes obtained from the image, $d = 2.18 \text{ \AA}$, agrees well with the known d -spacing value of h-BN $(10\bar{1}0)$ lattice planes, $d = 2.17 \text{ \AA}$ ^[52]. The fast-Fourier-transformed (FFT) image in the inset of Fig. 4.8e also confirms that the hexagonal lattice is single-orientated. Nanometer and atomic resolution imaging using TEM-EBSD and HR-TEM strongly suggest that the h-BN films are single-oriented and free of nanometer-sized grain boundaries or turbostratic crystalline structures.

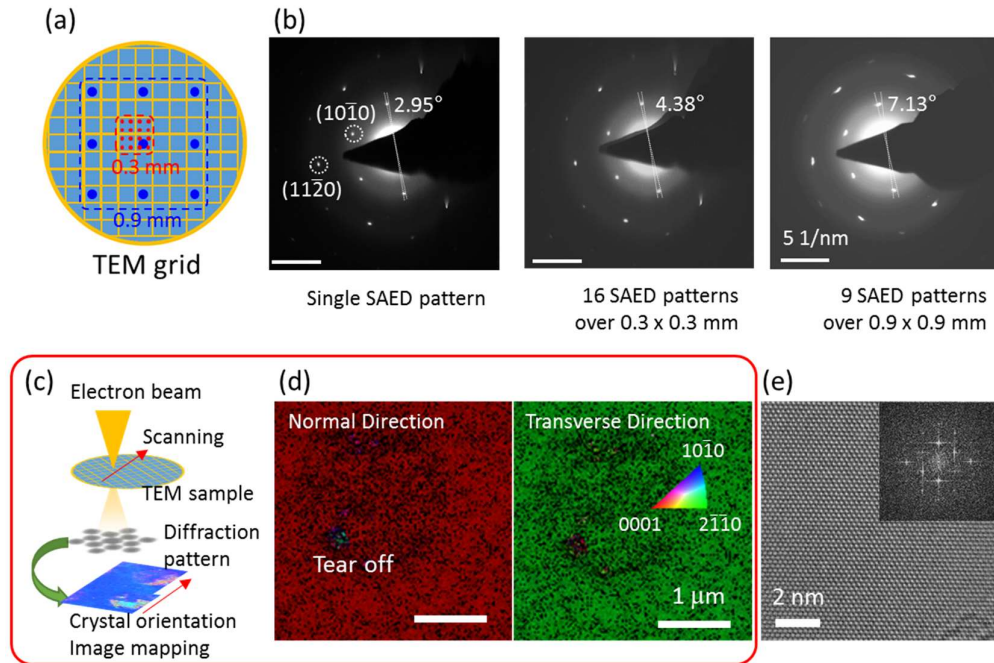


Figure 4.8 Microstructural analysis of h-BN film using TEM. (a) Schematic image of the SAED mapping analysis. (b) SAED image of a h-BN film from a single spot and overlaid SAED mapping images from 16 SAED patterns over a $0.3 \times 0.3 \text{ mm}^2$ area and 9 SAED patterns over a $0.9 \times 0.9 \text{ mm}^2$ area. (c) Schematic illustration of the TEM-EBSD analysis which visualizes real-space crystal structure. (d) TEM-EBSD IPF maps of a h-BN film in ND and TD. (e) HR-TEM image of a h-BN film. FFT image is shown in the inset

The physical properties of h-BN were characterized by Raman spectrum mapping, optical microscopy, AFM, ultraviolet-visible-infrared (UV-Vis-IR) spectroscopy transmittance measurements, and X-ray photoelectron spectroscopy (XPS). An optical microscope image of an h-BN film from which the Raman spectrum mapping is obtained is shown in Fig. 4.9a. The area covered by h-BN shows a uniform color contrast to the exposed SiO₂/Si substrate. From this region, the Raman spectrum was taken at each point in a 10 × 10 μm-sized area, using a 514.5-nm Ar-ion laser with a spot size of 1 μm. The Raman spectrum at a single spot is shown in the inset of Fig. 4.9b, showing a strong and sharp peak at a Raman shift of 1,368.3 cm⁻¹ corresponding to the characteristic E_{2g} modes of h-BN crystals¹. The slight shift of 2.3 cm⁻¹ compared to the bulk h-BN peak at 1,366 cm⁻¹ is attributed to the effect of the decreased number of layers^[53]. The intensity at the E_{2g} peak was mapped into a single image, as shown in Fig. 4.9b, where the E_{2g} peak exhibits a strong, uniform intensity on the h-BN-covered area in contrast to the SiO₂/Si area. The thickness of the h-BN film was investigated by AFM, as shown in Fig. 4.9c. A uniform thickness of 3 nm was observed over the measured region, with a surface roughness of 1 nm over a 1 × 1 μm area. This corresponded to 7–10 layers of h-BN, considering the *c*-spacing value of 3.3 Å. The measured thickness and corresponding number of layers were in agreement with cross-sectional HR-TEM analysis (inset of Fig. 4.9c), which shows a layered structure with 8 layers of h-BN.

The absorption spectra were investigated using UV-Vis-IR spectroscopy. h-BN films transferred on quartz substrates were used to investigate the absorbance curve. As shown in Fig. 4.9d, the absorbance was nearly 0 in near-IR, visible, and near-UV range, but increased significantly at wavelengths near 200 nm. To extract the optical band gap of h-BN layers, the absorbance curve of the h-BN film was converted to Tauc's plot (Fig. 4.9d, inset) based on Tauc's equation^[54]. The thickness of the h-BN film was assumed to be 3.0 nm. The calculated optical band gap was 6.0 eV, which is in good agreement with the known value of h-BN layers, 5.6–6.0 eV^[54].

The chemical composition of the h-BN film was examined by XPS. The XPS survey curve is shown in Fig. 4.10a, and detailed XPS spectra near B and N 1s peaks are shown in Fig. 4.10b–c, respectively. The binding energy of B and N were observed to be 190.59 eV and 398.09 eV, respectively, which is in good agreement with the literature values^[3,4]. The observed atomic composition ratio of B / N was 0.902, close to the 1:1 ratio of h-BN.

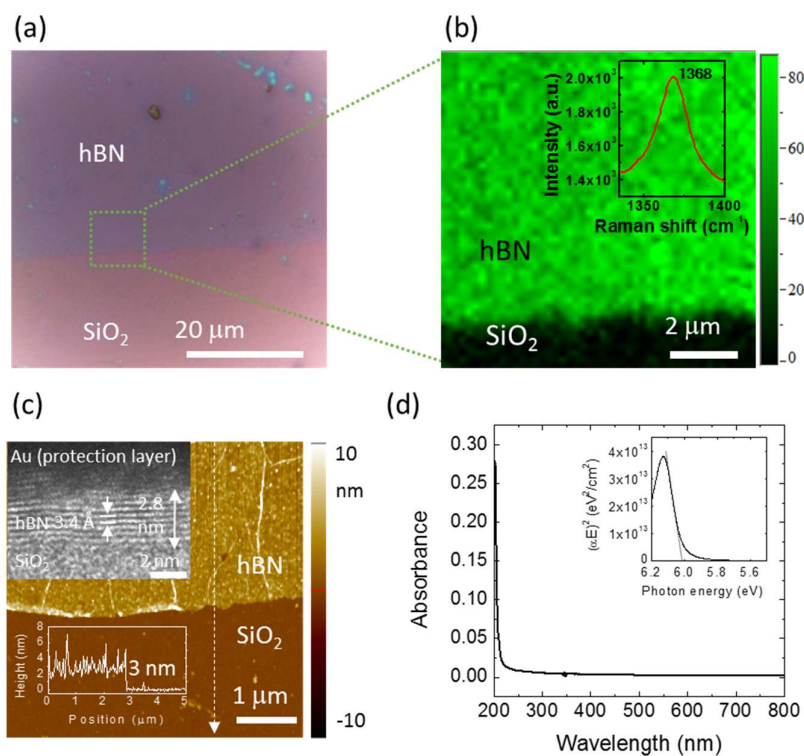


Figure 4.9 Physical properties of the epitaxial h-BN film. (a) Optical microscope image of a h-BN film transferred onto a SiO₂/Si substrate. (b) Raman map of the h-BN E_{2g} peak. The Raman mapping was performed in the region marked by the green square in (a). Raman spectrum of the h-BN film measured at a single spot is shown in the inset. (c) Surface morphology of the h-BN film investigated by AFM. (inset) Cross-sectional HR-TEM image of h-BN film transferred onto SiO₂/Si substrate. (d) UV-Vis-IR absorption spectrum of a h-BN film transferred onto a quartz substrate. Inset shows optical band gap analysis using Tauc's plot.

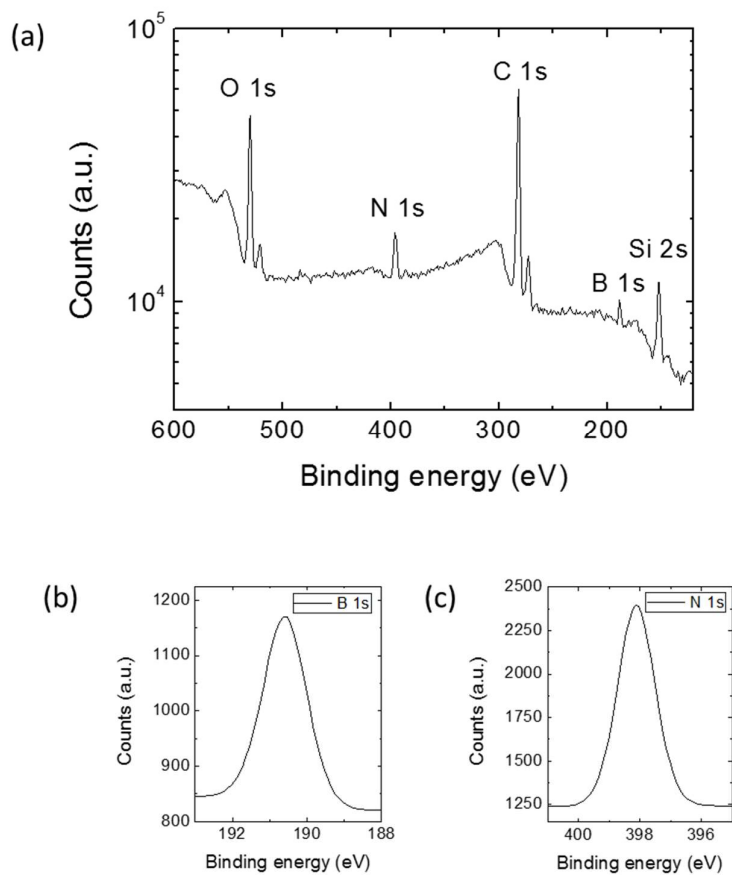


Figure 4.10 XPS analysis of the epitaxial h-BN film transferred onto SiO₂/Si substrate. (a) XPS survey curve of the h-BN. (b, c) Detailed spectra of (b) B 1s and (c) N 1s peaks.

The lateral electrical characteristics of h-BN films were investigated measuring the current–voltage (I – V) characteristics. Ti and Au for electrical contacts were evaporated on the h-BN film transferred onto a SiO₂/Si substrate as shown in Fig. 4.11(a). The metal contacts in an interdigit configuration were separated by 10 μm. The I – V characteristic curve of the device in Fig. 4.11(b) shows that the current level was as low as 0.3×10^{-9} A even at such a high bias voltage of 200 V, which is a very small value considering the small length-to-width ratio of the h-BN channel. This indicates that the h-BN film can be used as an insulating substrate for applications in large-area electronics and optoelectronics.

The flexibility of h-BN films in centimeter scale is demonstrated as shown in Fig. 4.12 by transferring the h-BN films on PET films and bending it.

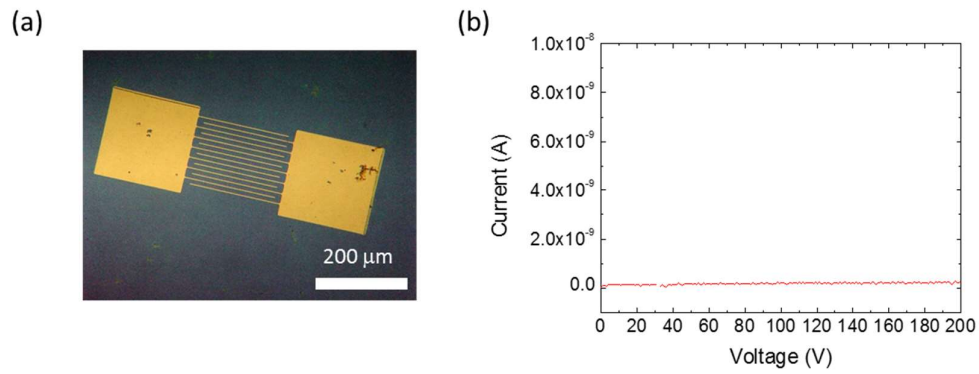


Figure 4.11 Electrical characterization of the epitaxial h-BN film. (a) Optical microscope image of metal electrodes on an h-BN film transferred onto a SiO₂/Si substrate. (b) *I*–*V* characteristic curves of the h-BN film.

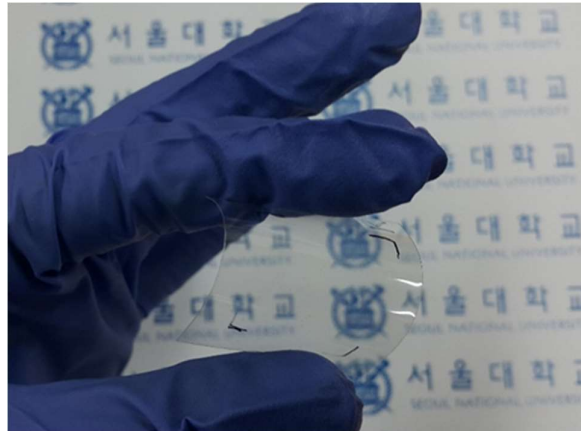


Figure 4.12 Flexibility demonstration of h-BN films transferred onto 25 μm-thick PET film.

4.5. Summary

In conclusion, centimeter-scale epitaxial h-BN layers were successfully grown and separated from Ni(111) single crystal substrates by combining CVD growth of h-BN with the bubbling transfer technique. The optimal source sublimation and growth temperatures were found to be important in synthesizing few layered h-BN with full coverage and high crystallinity, while cooling rate played a negligible role. Over repeated growth and transfer after the initial annealing, no significant degradation of Ni(111) substrates was observed and the crystallinity of h-BN layers was reproduced reliably. Using high-resolution SR-XRD, the h-BN films were confirmed to be single domain over a centimeter-scale area, and h-BN and Ni were found to form a heteroepitaxial relationship of h-BN(0002) \parallel Ni(111) and h-BN(11 $\bar{2}$ 0) \parallel Ni(20 $\bar{2}$) (or h-BN(10 $\bar{1}$ 0) \parallel Ni(11 $\bar{2}$)). The microstructural analysis using TEM suggested that the grown h-BN layers were of high crystallinity and have uniform crystallographic orientation over the entire region. Especially, structural distortions or nanometer-sized defects were not observed even at nanometer and atomic scales. The grown h-BN films showed typical physical characteristics of h-BN, with a high uniformity over a wide area. The large-area synthesis and transfer of atomically thin uniform epitaxial h-BN layers can be applied in various fields where high quality 2D insulating layers are required.

5. Heteroepitaxial growths of semiconductor 1D nanostructures on 2D nanomaterials and their structural characteristics: ZnO nanostructures on h-BN

5.1. Introduction

Heteroepitaxy of semiconductors on 2D layered nanomaterials has become a new integration method for fabricating transferable^[20,24] and flexible^[55–57] electronic and optoelectronic devices. Among various 2D layered nanomaterials^[58,59], hexagonal boron nitride (h-BN), a dielectric insulator with a wide direct bandgap of 5.2–5.9 eV, has great advantages as a substrate for many advanced electronics and optoelectronics,^[60,61] owing to its excellent thermal conductivity, optical properties,^[31] chemical/mechanical stability,^[4] and low dielectric constant.^[45] Because of the diatomic honeycomb crystal lattices of 2D layered h-BN sheets, the h-BN can be structurally compatible with many semiconductors having wurtzite, zinc blende, and diamond structures.^[24] The atomic layered structure of h-BN is also well suited as a substrate for transferable^[24] and flexible device applications. Moreover, the ability of h-BN to form alloy^[62] or lateral heterostructures^[63] with graphene is noteworthy for fabricating sophisticated

on-demand devices. The recent progress of large-scale h-BN synthesis with precisely controlled thickness via chemical vapor deposition techniques^[4] may allow the integration of semiconductors with wafers based on conventional microfabrication processes. Accordingly, the heteroepitaxial integration of semiconductors on h-BN is expected to generate significant advances in design, fabrication, and performance for diverse semiconductor optoelectronic and electronic circuitry.

Noncovalent epitaxy, the so-called van der Waals (vdW) epitaxy,^[27,64–66] has the ability to produce single-crystalline semiconductor nanostructures with an abrupt clean heterointerface and suppressed threading dislocation density even for highly lattice-mismatched heteroepitaxial systems^[67]. Accordingly, it is well suited for fabricating high-quality epitaxial semiconductor/h-BN heterostructures for diverse device applications. Nevertheless, the weak attraction due to the chemically inert vdW surfaces makes it difficult to control the heterogeneous nucleation at specific sites; thus, amorphous open-patterned mask layers were used to direct the semiconductor nucleation on the vdW surfaces.^[15,68] In addition, a major challenge remains in the vdW epitaxy of semiconductors on h-BN: precise control of the position, size, and shape of semiconductor nanostructures, all of which are critical for monolithic microelectronic processing^[69–73]. In this chapter, we report on the maskless shape-controlled vdW heteroepitaxy of ZnO nanostructures on h-BN substrates in a designed fashion using the artificially formed atomic ledges on h-

BN. Electron microscopic analyses and first-principles theoretical calculations exhibit how the highly lattice-mismatched ZnO/h-BN heterojunction is fabricated to be high quality using vdW epitaxy. The role of atomic ledges of h-BN in controlling the morphology and shape of the semiconductor overlayer is discussed. The ultraviolet (UV) photosensor device using the vdW epitaxial ZnO nanowall networks/h-BN heterostructure is further demonstrated as an example of h-BN substrate-based device applications.

5.2. Growth of ZnO nanostructures on h-BN layers

The vdW heteroepitaxy of ZnO using MOVPE yielded two distinct nanostructure morphologies on h-BN. The schematics in Figure 5.1 represent experimental procedures for obtaining either ZnO nanoneedles or nanowalls depending on the surface treatment of h-BN. Under the same vdW–MOVPE growth conditions, the pristine h-BN surface resulted in vertical ZnO nanoneedle arrays (Figures 1a and b), while O₂ or Ar plasma-treated h-BN substrates yielded high-density vertical nanowall networks (Figures 1c and d). The number density of nanoneedles was measured to be $(6.2 \pm 2.8) \times 10^8 \text{ cm}^{-2}$; the line density of nanowall networks was $(1.5 \pm 0.2) \times 10^5 \text{ cm}^{-1}$ (corresponding to $\approx 2.3 \times 10^{10} \text{ cm}^{-2}$ in areal density). This suggests that the plasma-treated h-BN surface promotes high-density heterogeneous vdW nucleation, leading to the formation of interconnected

nanowalls, presumably resulting in random network morphology. Because both Ar and O₂ plasma treatments damage and etch the h-BN surfaces (Figure 5.2), the roughness, including atomic steps and kinks, formed by plasma is thought to play a critical role in the control of nanostructure density and morphology (Figure 5.3). This implies that artificially controlled atomic steps or kinks of h-BN enable the growth of nanostructures with designed shapes, which will be demonstrated later.

We envision that ZnO nanoneedles are grown on quite tiny atomic edges (or vacancy) of h-BN while the nanowalls are grown along the long ledges that are contoured continuum of atomic step-edges. On the mechanically exfoliated pristine h-BN substrates, three different morphologies of ZnO nanostructures were obtained by the vdW epitaxy: i) isolatedly grown nanoneedles, ii) high-density nanoneedles, and iii) nanowalls with high-density nanoneedles formed in an alignment (Figure 5.4). Since there are many long step-edges on the exfoliated h-BN layers, it is surmised that the isolated nanoneedles were formed on the flat h-BN terrace region, while high density formation of nanoneedles along the ledges became interconnected to be nanowalls.

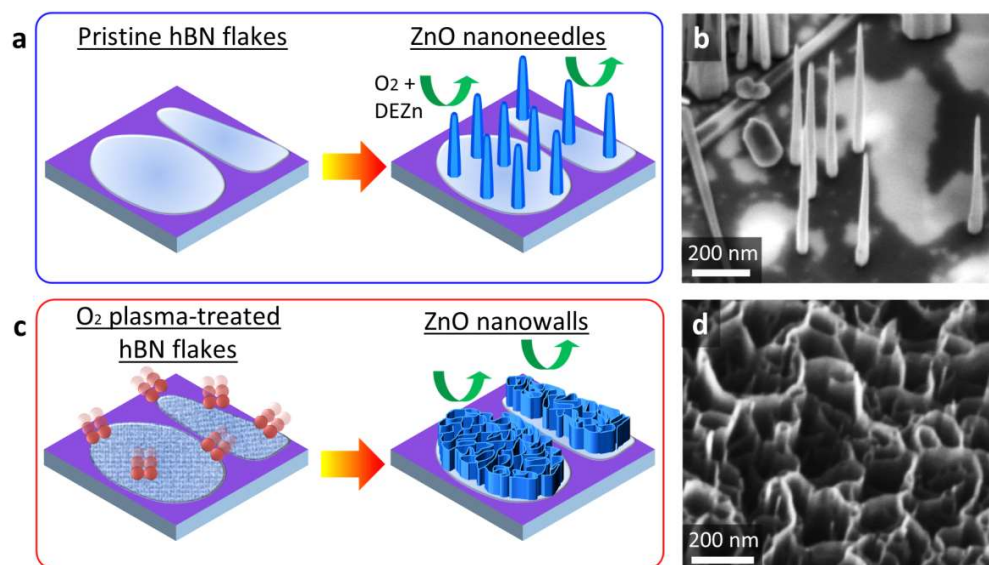


Figure 5.1 Morphology-controlled vdW heteroepitaxy of ZnO nanostructures on h-BN substrates. Schematic of the fabrication process and tilt-view FESEM images of (a,b) ZnO vertical nanoneedle arrays and (c,d) nanowall networks. ZnO nanoneedles and nanowall networks were obtained using pristine h-BN and plasma-treated h-BN substrates, respectively.

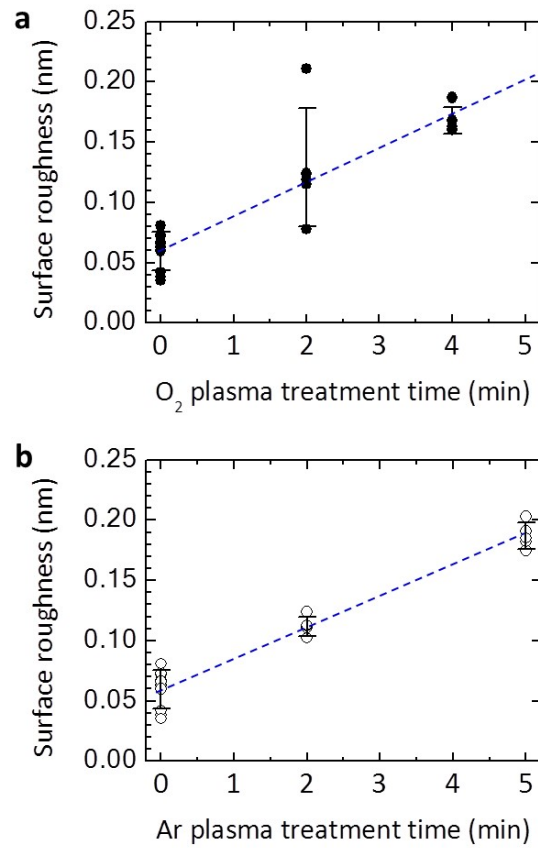


Figure 5.2 Plots of root-mean-square roughness of the h-BN layer treated by (a) oxygen and (b) argon plasma as a function of the plasma treatment time. The roughness was characterized on the step-edge-free h-BN areas of $1 \times 1 \mu\text{m}^2$ to clarify the roughening effect of plasma treatment. Error bars denote the standard deviations.

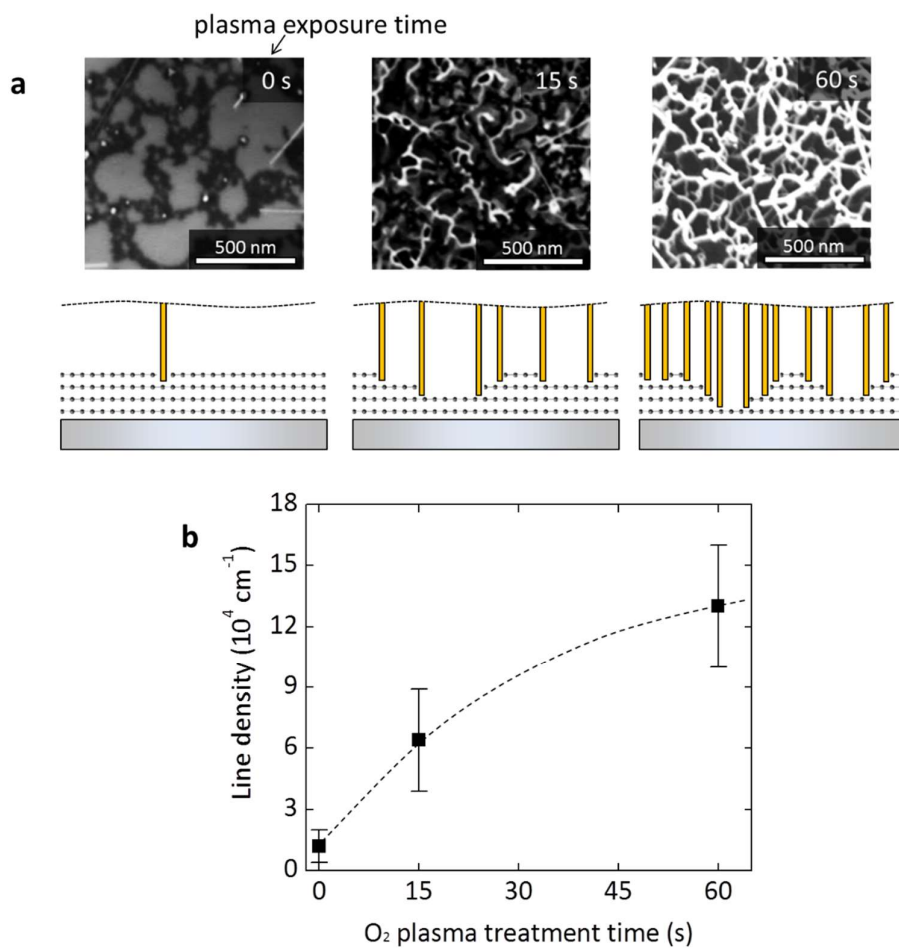


Figure 5.3 Effect of h-BN surface roughness on nanowall density. (a) Top-view SEM images of ZnO nanowalls formed on h-BN layers treated by oxygen plasma for 0, 15, and 60 sec. (b) Plot of nanowall line density as a function of the plasma treatment time. Error bars denote the standard deviations.

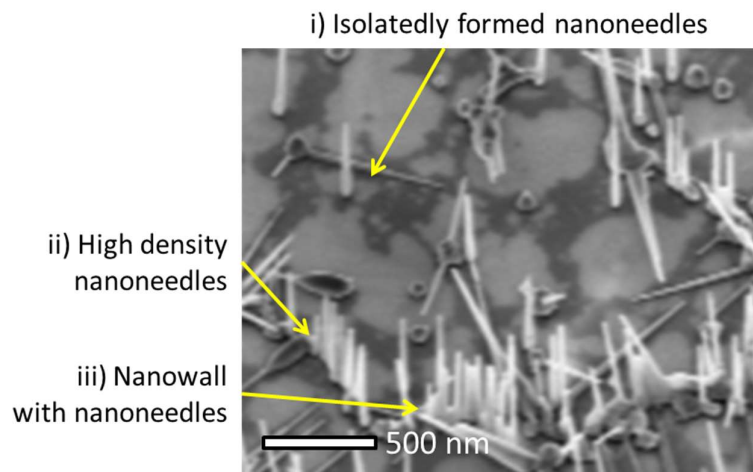


Figure 5.4 Tilt-view SEM image of ZnO nanostructures grown on bare h-BN exfoliated from h-BN crystallites. Three different morphologies are obtained: i) isolatedly grown ZnO nanoneedles; ii) high density nanoneedles or iii) nanowall with high density nanoneedles in a specific alignment.

5.3. Structural properties of ZnO nanostructures on h-BN layers

The vdW heterointerface and crystallographic growth direction of the ZnO nanostructures were examined by cross-sectional HRTEM. The TEM images of Figures 5.5a and b show that a ZnO nanoneedle grew vertically on h-BN layers with an atomically abrupt heterointerface. From the HRTEM image, the lattice spacings between adjacent planes were measured to be 0.26 and 0.34 nm in the ZnO nanoneedle and h-BN layer, corresponding to the d -spacings of ZnO(0002) and h-BN(0002), respectively. Fast Fourier-transformed (FFT) micrographs in the insets of Figure 5.5b show that the ZnO nanoneedle grew along the c -axis of wurtzite perpendicular to the h-BN surface. Importantly, no extended crystal defects, such as threading dislocations and stacking faults, were observed at the heterointerface through high-resolution and two-beam microscopic analyses, presumably due to stress relaxation through the noncovalent vdW heterointerface. The previous works by Utama *et al.* clarified that no misfit threading dislocations are generated from the highly incommensurate vdW heteroepitaxial system.^[67] Hence, all the microstructural features showed that high-quality heterointerfaces of single-crystalline ZnO nanostructure/h-BN are presumably attributed to the weakly bound vdW heterojunction.

The CBED analyses revealed notable microstructural characteristics of vdW epitaxial ZnO/h-BN. Figure 5.5c shows that the CBED disk patterns obtained from the ZnO nanoneedle exhibit clear asymmetric stripy contrasts: the ZnO nanoneedles were found to grow along the oxygen-terminated $[000\bar{1}]$ direction by vdW heteroepitaxy on h-BN, which is in close accordance with those simulated at the same sample thickness (~ 25 nm). Noticeably, ZnO nanowalls on plasma-treated h-BN also exhibited identical growth orientation (Figure 5.12). These CBED analyses obtained from nanoneedles and nanowalls grown on h-BN indicate that ZnO nanostructures grow exclusively along the oxygen-polar c -axis direction through vdW heteroepitaxy, regardless of the surface treatment of h-BN.

The vdW heteroepitaxial relationship of ZnO nanostructures and h-BN was further investigated by plan-view TEM observations. The low-magnification TEM image of ZnO nanoneedles grown on few-layer h-BN films shows that the neighboring nanoneedles, all of which exhibit a hexagonal prismatic morphology with six wurtzite- $\{10\bar{1}0\}$ sidewall facets, have a fairly uniform six-fold rotational in-plane alignment (Figure 5.6a). The HRTEM images in the insets of Figure 5.6b display the hexagonal lattices of ZnO and h-BN with the same crystallographic alignments, although the lattice mismatch of ZnO/h-BN is -30.0% for the heteroepitaxial relationship of $(000\bar{1})[10\bar{1}0]_{\text{ZnO}} \parallel (0001)[10\bar{1}0]_{\text{h-BN}}$. It is well known that such large lattice misfits in a hexagonal heteroepitaxial system, *e.g.*,

ZnO/Al₂O₃, GaN (or AlN)/Al₂O₃, *etc.*, typically yield the heterostructures of (0001)[11 $\bar{2}$ 0]_{overlayer} || (0001)[10 $\bar{1}$ 0]_{substrate}, whose overlayer is crystallographically rotated by 30° with respect to the substrate to minimize dangling bond density through covalent heteroepitaxy.^[74–76] Recent works on epitaxy of III–V nanowires on graphene also points the possible rotated in-plane epitaxial relationships or different nanowire growth directions presumably caused by lattice mismatch when covalent epitaxial links exist at the heterointerface.^[77,78] Hence, it is strongly suggested that the observed domain-aligned heteroepitaxial relationship of ZnO/h-BN should result from weakly bound vdW heterointerfaces.

The plan-view TEM image in Figure 5.6b shows the presence of periodic triangular Moiré fringes in the ZnO/h-BN with a periodicity of ~1.0 nm due to the large lattice misfits. The periodicity was three times as large as the d_{100} of ZnO (≈ 3.25 Å) and four times as large as the d_{100} of h-BN (≈ 2.50 Å). These values for the Moiré periodicity, however, have a misfit of 2.5% so that the ZnO/h-BN is classified as an incommensurate vdW epitaxial system.

The selected-area electron diffraction (SAED) patterns in Figure 5.6c, obtained from a few dozen nanoneedles within a selected area aperture size of ~200 nm, show the homogeneous heteroepitaxial relationship of ZnO/h-BN. No multiple epitaxial relationships were observed in the plan-view TEM analysis, and the statistical distribution of the in-plane alignment of ZnO nanoneedles was estimated

at a standard deviation width of $\pm 4.5^\circ$ in the SAED intensity profile of ZnO $\{10\bar{1}0\}$ (Figure 5.6d). We believe that the slightly deviated epitaxial relationship is presumably caused by the weakly bound attraction of the vdW epitaxial ZnO/h-BN heterointerface.

Based on the TEM observations, a ball-and-stick model was simulated with an assumption that the ZnO/h-BN interfacial layers are fully relaxed, owing to weakly bound vdW heteroepitaxy. The low-magnification ball-and-stick image clearly displays regular triangular Moiré patterns with a periodicity of ~ 1.0 nm (Figures 5.7a and c). This is in close agreement with the plan-view TEM observation shown in Figure 3b. The corresponding simulated diffraction patterns (Figure 4b), obtained through Fourier transforms from the ball-and-stick image of Figure 4a, are also in good agreement with the SAED pattern shown in Figure 5.6c. Inside a unit Moiré pattern (marked with a triangle in Figure 5.7c), two distinct heteroepitaxial atomic configurations are shown: ball-to-ball and ball-to-hollow epitaxial atomic configurations (Figure 5.7d). According to the ball-and-stick model, there are at least a few plausible epitaxial arrangements because of the incommensurate epitaxial relationship, as displayed in Figure 5.7e.

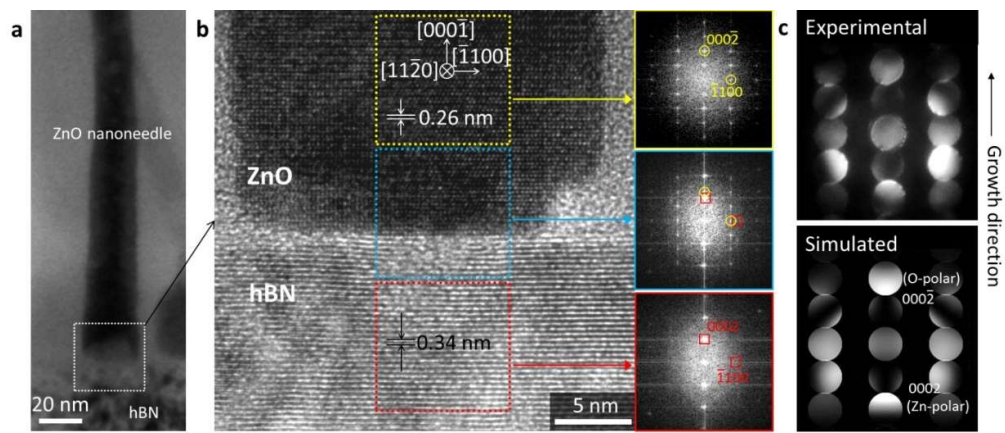


Figure 5.5 Heterointerface of vdW epitaxial ZnO/h-BN observed by cross-sectional TEM. (a) Low-magnification cross-sectional TEM image of vertical ZnO nanoneedles grown on h-BN. (b) HRTEM lattice images of the ZnO nanoneedle/h-BN heterointerface. The right insets are selected-area diffraction patterns obtained through a FFT process of the HRTEM images marked with enclosed areas. (c) Experimental and simulated CBED patterns of ZnO nanoneedles preferentially grown along the O-polar (0001) direction.

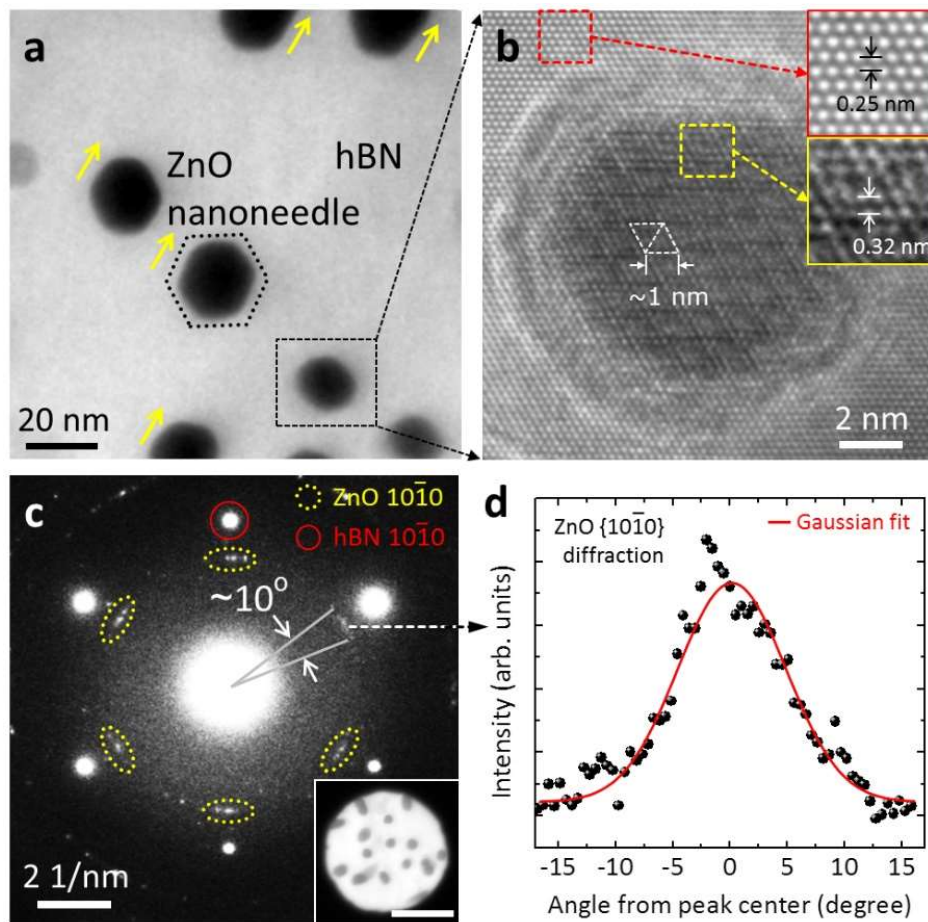


Figure 5.6 VdW heteroepitaxial relationship of ZnO/h-BN investigated by plan-view TEM. (a) Plan-view low-magnification TEM image of ZnO nanoneedles grown on few-layer h-BN. (b) Plan-view HRTEM lattice image displaying in-plane epitaxial relationship of ZnO/h-BN. Diamond-shape Moiré patterns are repeatedly observed every 1 nm. (c) SAED patterns obtained from the area shown in the inset (scale bar, 100 nm). (d) Intensity profile of electron beam diffraction of ZnO $\{10\bar{1}0\}$ as a function of the central angle.

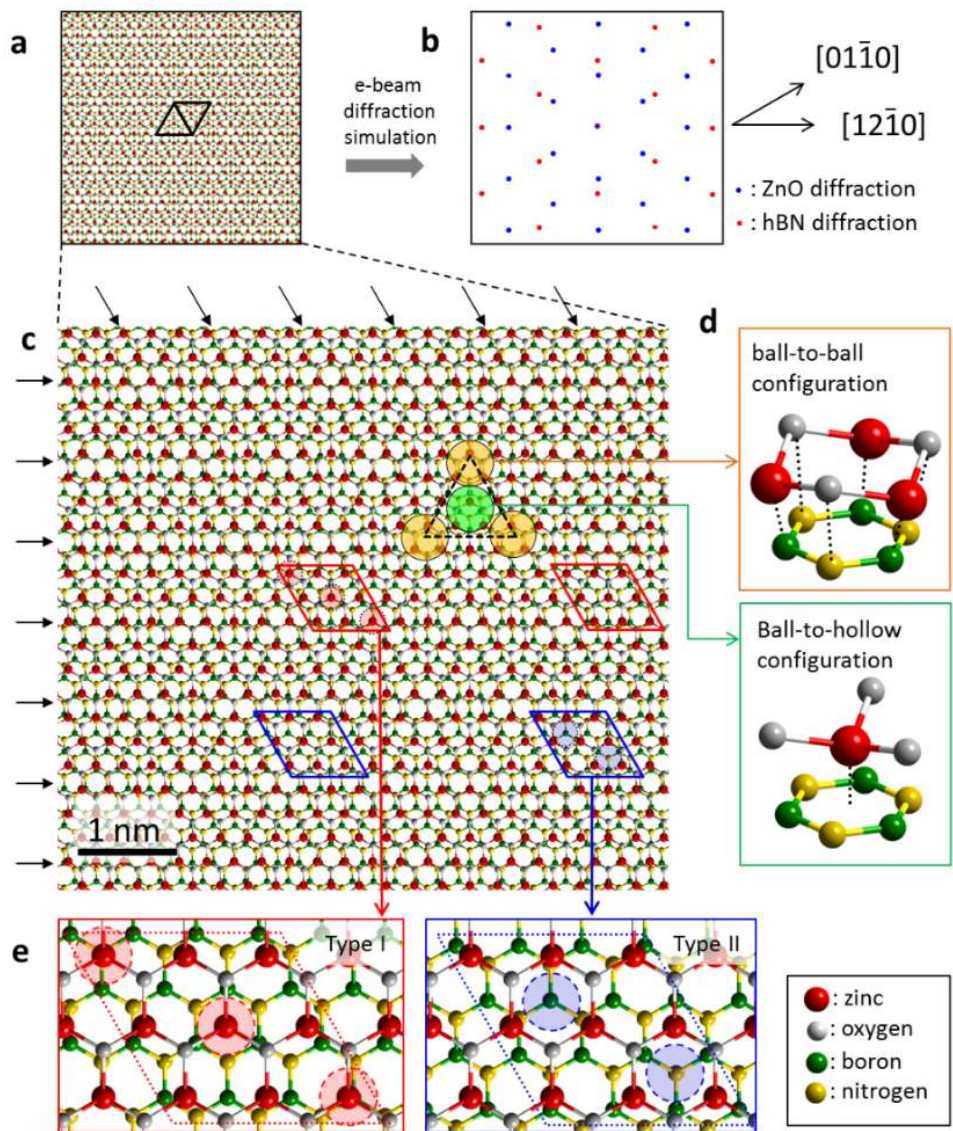


Figure 5.7 Ball-and-stick model for vdW epitaxial ZnO/h-BN heterostructure. (a) Low-magnification model for $(000\bar{1})[10\bar{1}0]\text{ZnO} \parallel (0001)[10\bar{1}0]\text{h-BN}$ heterostructure viewed along $[0001]$. The image clearly exhibits periodic triangular Moiré fringes with a periodicity of ~ 1.0 nm. (b) Diffraction patterns obtained from (a) through a Fourier-transform-based simulation. (c) High-

magnification ball-and-stick model. (d) Two heterointerfacial atomic epitaxial relationships for ball-to-ball (upper panel) and ball-to-hollow (bottom panel) configurations appearing in the Moiré pattern. (e) Two supercell structures of ball-top-matching (Type I) and hollow-matching (Type II) (3×3) -ZnO/ (4×4) -BN heterojunctions for the incommensurate vdW ZnO/h-BN heterostructure.

5.4. vdW heterointerface of ZnO/h-BN simulated by DFT

The vdW interfacial binding properties of the epitaxial ZnO/h-BN heterostructures were explored by DFT total energy and electronic structure calculations. Two representative supercells are presented in Figures 5.8a and b: a ball-top-matching configured supercell in which two Zn atoms are on top of B and/or N atoms (type I, Figure 5.8a); and a hollow-matching supercell consisting of two hollows of ZnO hexagon lattices on top of B or N atoms (type II, Figure 5.8b) in a supercell of a ZnO slab (3×3) on a BN slab (4×4).

The DFT computation for these two supercells revealed a few important interfacial features. First, the interaction energy ($\Delta E = E_{\text{total}} - E^{\text{ZnO}} - E^{\text{h-BN}}$) values of both types I and II supercells were calculated to be 2.170 and 2.165 eV nm⁻². These values are much smaller than that of typical covalent bindings by one or two orders of magnitude. Importantly, the differences in the interfacial interaction energies were quite small (5 meV nm⁻²) between them. Second, the equilibrium vdW spacing of ZnO-h-BN was 3.4 Å (Figure 5.8c), greater than the typical distances of chemical primary bonds such as covalent or ionic binding. Third, the heterointerface for both type I and II supercells exhibited no bonds with valence electrons being shared or donated (Figure 5.8d). The electron density difference contoured at $\pm 0.0002e \text{ \AA}^{-3}$ (Figures 5.8a and b) and Bader analysis (Figure 5.8d) showed little electron orbital hybridization (charge transfer) through the vdW

heterointerface. At equilibrium, little buckling (or distortion) was observed at the heterointerfaces. It is notable that the calculated values for type I and II supercell heterointerfaces showed negligible disparities in terms of binding energy, equilibrium vdW distance, and electronic structure. This implies that there is no primary epitaxial relationship among them. Therefore, all the calculated heterointerfacial results show that the binding interactions are almost homogeneous over the whole ZnO/h-BN heterointerface.

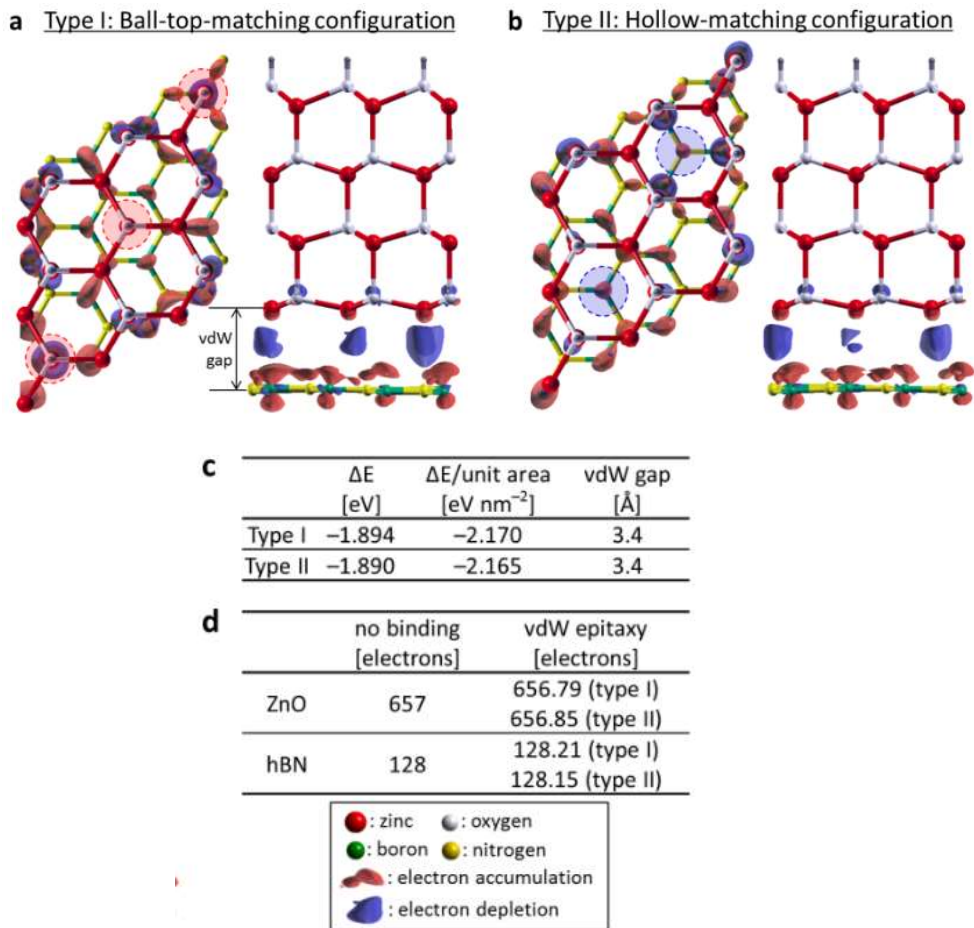


Figure 5.8 Electronic structure and adhesion energy of the vdW epitaxial ZnO/h-BN heterointerface computed by the DFT method. Atomic model structures and electron density difference isosurfaces at the periphery of the heterointerfaces with (a) ball-top-matching and (b) hollow-matching configurations of ZnO/h-BN. The electron density was contoured with an isovalue of $\pm 0.0002e \text{ \AA}^{-3}$. (c) vdW heterointerfacial adhesion energy and equilibrium vdW distance values for type I and II supercells. (d) The electron populations in the ZnO and h-BN parts of the supercells before and after the

vdW epitaxy, calculated by Bader analysis. The electronic structure mapped at the ZnO/h-BN heterointerface implies a vdW binding feature with less electron orbital hybridization.

5.5. Position-controlled ZnO nanostructures on h-BN layers

The preferential formation of high-density nanowalls on the rough h-BN surface could be exploited for creating shape- and position-controlled ZnO nanostructures. Figure 5.9a shows schematics of the process for selective-area vdW–MOVPE of ZnO nanowalls. To control both the shape and position of the ZnO nanowalls, the predetermined area of h-BN was treated by O₂ (or Ar) plasma through the opening of a resist layer patterned by conventional lithography, followed by wet removal of the polymer resist for high-temperature growth.

The SEM images of Figures 5.9b and c shows the shape- and position-controlled ZnO nanostructures composed of vertical nanowall networks. The shapes of outer nanowalls were determined by the plasma-treated area of h-BN. Specifically, the outer nanowalls are continuously interconnected with uniform height even in complicated shapes, because of the enhanced growth of ZnO nanowalls along ledges of the plasma-treated h-BN area. Shape-controlled ZnO nanowall architectures grown on h-BN exhibited the same epitaxial relationship of $(000\bar{1})[10\bar{1}0]_{\text{ZnO}} \parallel (0001)[10\bar{1}0]_{\text{h-BN}}$ and exclusive growth orientation along the oxygen-terminated $[000\bar{1}]$ direction (Figure 5.12).

The optical properties of ZnO nanoarchitectures were investigated using CL spectroscopy. The room-temperature CL spectrum of the ZnO nanostructure arrays

shows a dominant near-band-edge (NBE) emission peak at 3.25 eV, attributable to a free exciton emission (Figure 5.9e).^[79] No deep-level emission, typically observed from bulk ZnO materials, was observed. The full width at half maximum of the NBE was as narrow as ~ 100 meV, comparable to a previous report,^[80] indicating a high quality and purity of ZnO nanostructures grown on h-BN by vdW epitaxy. The insets of Figure 5.9e show the SEM and corresponding CL monochromatic images of the ZnO nanostructure array. The latter was measured at the photon energy of 3.25 ± 0.01 eV using a monochromator. The monochromatic CL image shows homogeneous and strong CL emission of the ZnO nanostructure arrays. The SEM and CL images look almost the same, suggesting that nonradiative or other radiative transitions caused from defects or impurities were not observed. The NBE emissions of the nanostructure arrays were homogeneous in intensity. In addition, from the high-resolution photoluminescence spectroscopic analyses, nitrogen- or boron-associated ZnO luminescence was not observed (Figure 5.11).^[81,82] This suggested that the atoms in h-BN were not incorporated into the ZnO nanostructures during the vdW–MOVPE process.

The vdW–MOVPE growth mode of ZnO was altered from 1D nanoneedle formation to vertical 2D nanowall growth as the surface of h-BN was roughened by plasma treatment. This vdW growth mode transition is strongly related to the atomic ledges formed on the h-BN surface by the plasma. According to our investigations (Figures 5.2 and 3), it is envisioned that the h-BN ledges formed by plasma

treatment promote the formation of high-density ZnO nuclei along the ledges, resulting in continuously interconnected ZnO nanowalls. This plausible scenario could be applied to the architectural vdW epitaxy of ZnO nanostructures. Because of the slow plasma etching rate of h-BN ($\sim 0.5\text{--}0.8 \text{ \AA s}^{-1}$), shape-controlled atomic ledges could be formed with a precisely controlled etching depth at the few-atomic-layer level (Figure 5.9d and 5.10). During the vdW–MOVPE process, multiple ZnO nuclei that preferentially dwell along the vdW ledges (the edge of the plasma-treated area) are then connected at their base to form outer nanowalls.

The enhanced nucleation of ZnO along the ledges points to the existence of a reduced Ehrlich–Schwoebel energy barrier encountered by the adatoms that diffuse downward^[83,84] from the non-treated ultraflat h-BN area into the plasma-etched rough h-BN in the initial vdW growth stage. The reduced barrier presumably played a critical role in overcoming the difficulties of heterogeneous nucleation at specific sites caused by the weak attraction of the chemically inert vdW surface. In consequence, the shape-controlled semiconductors could be created by maskless vdW heteroepitaxy along the artificially formed ledges, distinguishable from the conventional selective-area growth that necessarily uses amorphous growth mask layers.^[85] The high-density formation of nanowalls on the h-BN flake entirely etched by plasma also supports our argument on the reduced energy barrier for enhanced nucleation of ZnO along the ledges because longer plasma exposure causes formation of more ledges on the h-BN flake (Figures 5.2 and 3). Importantly,

the ZnO nanowalls grown by the architected vdW heteroepitaxy were single crystalline, as confirmed by TEM analysis (Figure 5.12b), indicating that no other directional growth occurred from the ledges. This implies that the maskless vdW selected-area heteroepitaxy of shape-controlled ZnO nanostructures is a suitable integration method for electronic and optoelectronic device applications. It is also expected that the selective vdW epitaxy can be exploited for fabricating smooth ZnO thin film structures by combining two processes required to grow the film structures: i) formation of high-density regular arrays of nuclei (or nanostructures) that are sufficiently close to coalesce to form films, and ii) epitaxial lateral overgrowth on the site-selectively formed nanostructures. It is noted that Liu and co-workers reported that the selected-area chemical surface modification inhibited the growth but only the intact substrate area contributed to the maskless site-selective vdW epitaxy of Bi_2Se_3 , Bi_2Te_3 ^[86], and In_2Se_3 ^[87] nanoplates with desired spatial arrangements.

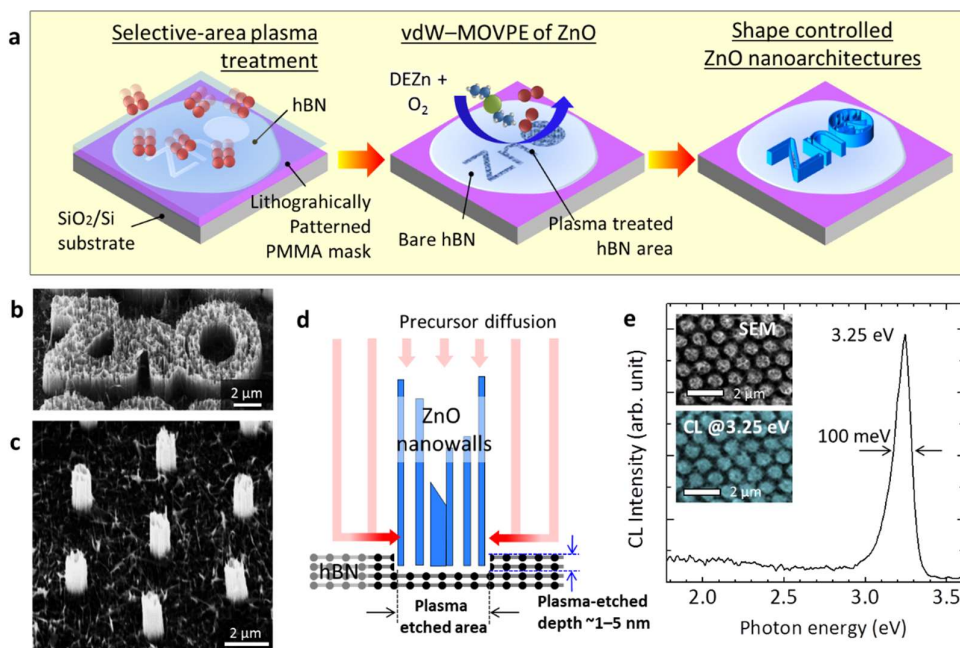


Figure 5.9 Shape-controlled vdW heteroepitaxy of ZnO nanoarchitectures on h-BN layers. (a) Schematic of selective growth of ZnO nanowalls on h-BN films for shaping the outer nanowalls. Tilt-view SEM image of ZnO (b–c) nanoarchitectures on h-BN films with designed shape and spatial arrangements. (d) Cross-sectional schematic showing how ZnO nanoarchitectures are formed on a plasma-treated h-BN area via the vdW–MOVPE. (e) Room-temperature CL spectra of ZnO nanostructures. The insets are top-view SEM images (upper) and the corresponding monochromatic CL image obtained at a photon energy of 3.25 eV (bottom).

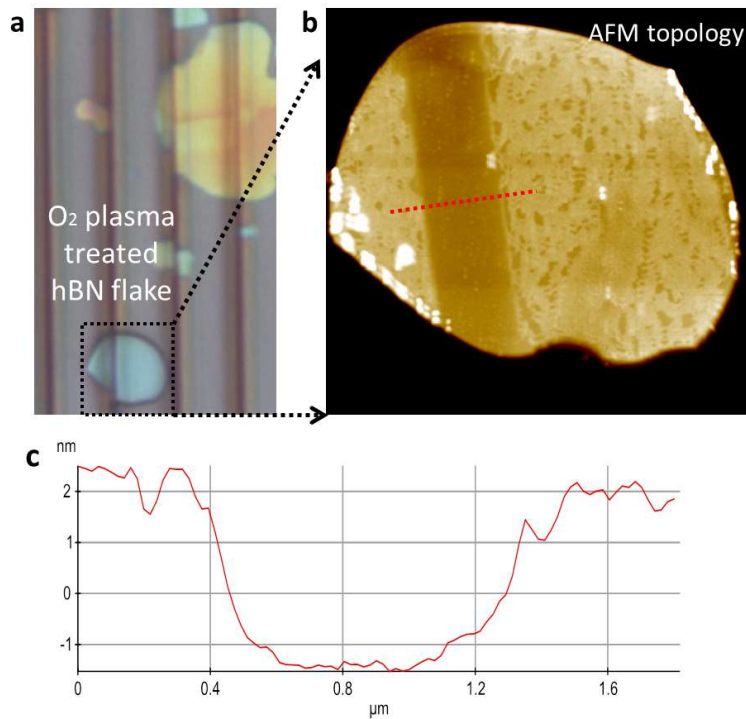


Figure 5.10 H-BN layer etched by plasma treatment. (a) Optical micrograph of h-BN layer treated by oxygen plasma for 1 min via polymer resist layer with line-opening patterns. (b) AFM topological map of h-BN flake marked in (a). The polymer resist was removed before the AFM measurement. (c) Depth profile of the h-BN surface measured along the red dotted line depicted in (b). The etch rate is estimated to be 0.5–0.8 Å sec⁻¹.

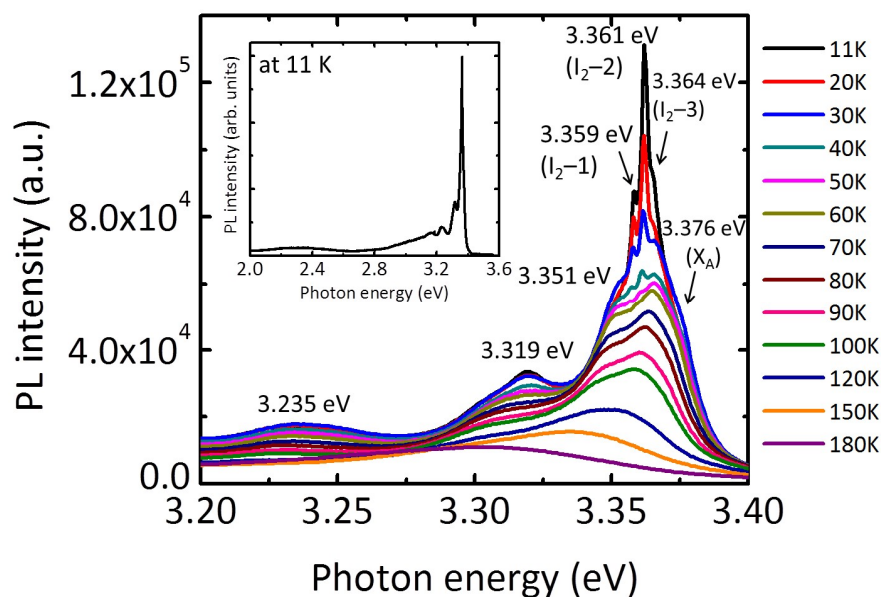


Figure 5.11 Photoluminescent characteristics of ZnO nanoarchitectures grown on h-BN by vdW epitaxy. A series of PL spectra was measured at various temperatures in the range of 11–180 K. The spectrum at 11 K shows seven distinct NBE emission peaks at 3.376, 3.364, 3.361, 3.359, 3.351, 3.319, and 3.235 eV. The PL peak at 3.376 is attributed to a free exciton peak (X_A). The peaks at 3.359, 3.351, and 3.364 eV are ascribed to neutral-donor bound excitonic emissions (I_2) [see Ref. S1, S2]. The sharp and strong NBE emission indicates high optical quality of ZnO nanoarchitectures grown by vdW epitaxy (see inset). The excellent PL properties may result from the high crystallinity of ZnO nanoarchitectures because threading dislocations were not generated from the vdW heterointerface, as confirmed by HRTEM observations.

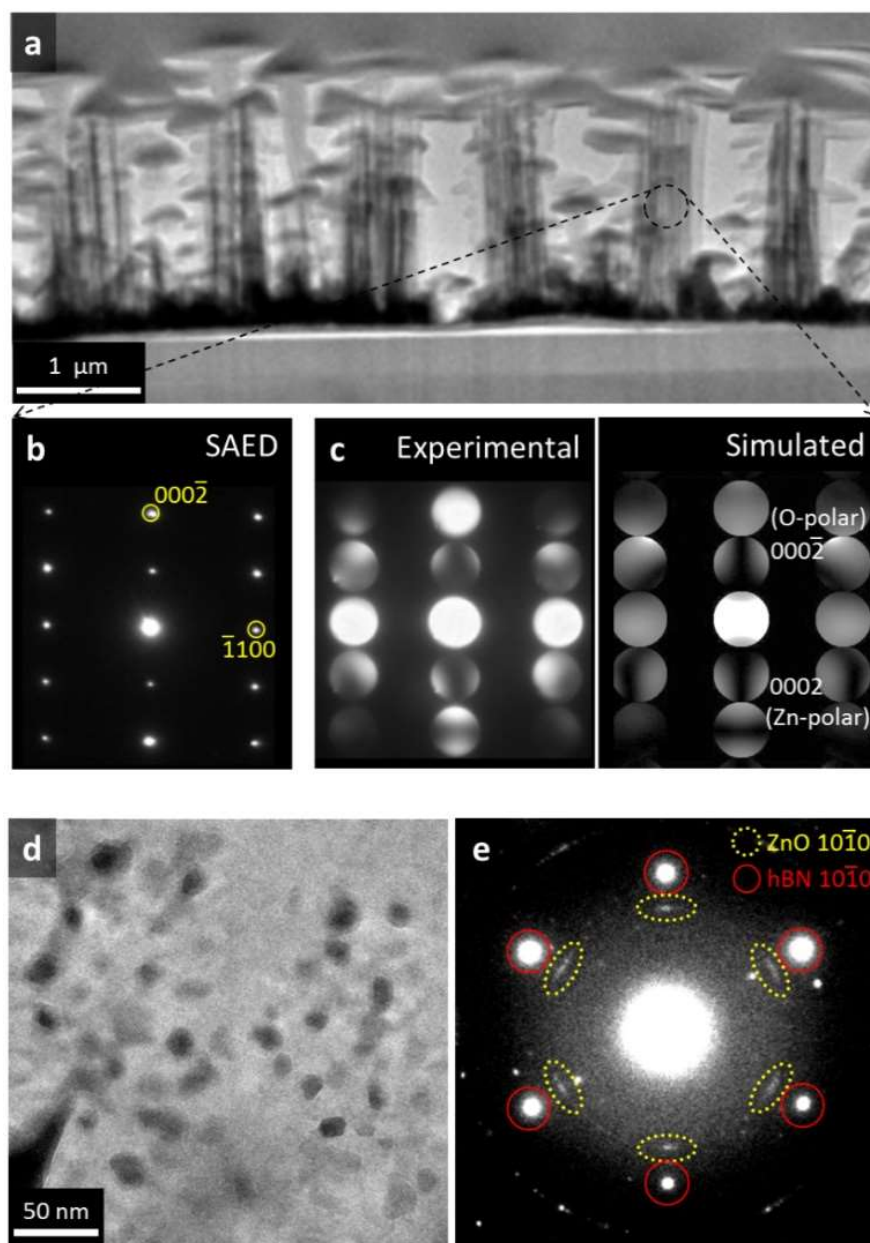


Figure 5.12 Transmission electron microscopic analysis of ZnO nanoarchitectures. (a) Cross-sectional low-magnification TEM image of ZnO nanostructure arrays. (b) Selected-area electron diffraction (SAED)

patterns obtained from the dotted line circle marked in (a), confirming the single crystallinity of the nanoarchitectures. The ZnO nanoarchitectures grew along the c-axis of wurtzite normal to the surface of h-BN. (c) Experimental and simulated convergence beam electron diffraction (CBED) patterns of ZnO nanoarchitectures preferentially grown along the O-polar $(000\bar{1})$ direction. The sample thickness for CBED was 37 nm, and the simulation was performed under the same thickness condition. Plan-view (d) low-magnification TEM image and (e) SAED patterns of ZnO nanowalls grown on few-layer h-BN. The SAED patterns exhibit the heteroepitaxial relationship of $(000\bar{1})[10\bar{1}0]\text{ZnO} \parallel (0001)[10\bar{1}0]\text{h-BN}$.

5.6. Growth and structural properties of ZnO nanostructures on large-scale single crystalline h-BN layers

5.6.1. Growth of ZnO nanowall network on large-scale epitaxial h-BN layers

The basic strategy for the heteroepitaxial growth of ZnO nanostructures on the single crystalline h-BN film is illustrated schematically in Figure 5.13a. The h-BN films is synthesized on single crystalline Ni(111) substrates using chemical vapor deposition (CVD) method with ammonia-borane as a single precursor, and transferred onto arbitrary substrates such as SiO₂/Si using electrochemical delamination methods. Detailed procedures are described elsewhere.⁽¹⁸⁾ Then, ZnO nanostructures are grown on h-BN/SiO₂/Si substrates using metal-organic vapor phase epitaxy with diethylzinc (DEZn) and high-purity oxygen gas as precursors of zinc and oxygen. The typical growth temperature and time are 600 °C and 2 hr, respectively. Here, DEZn is introduced 3 sec prior to the oxygen to enhance the nucleation and prevent unwanted pre-reactions.

The ZnO/h-BN heterostructure was prepared in a centimeter-sized area, as shown in the photograph in Figure 5.13b. Uniform greenish color is observed from the ZnO nanostructures grown on h-BN film, while bluish color is observed from the ZnO nanostructures directly grown on SiO₂ layers. This suggests that the growth of ZnO nanostructures was uniform over the substrate, but the structures of them

are different depending on the types of substrate. Figure 5.13c shows corresponding field-effect secondary electron microscope (SEM) images of ZnO nanostructures, marked in Fig. 5.13b. Vertically aligned ZnO nanostructures are observed only on the h-BN films, while entangled ZnO nanowires with random orientations are observed on the SiO₂/Si substrate. The unique vertical alignment of the ZnO nanostructure on the h-BN film implies the heteroepitaxial relationship between ZnO and h-BN, which will be discussed later. The average height of ZnO nanostructures were determined to be 3 μm, corresponding to the growth rate of 1.5 μm/hr.

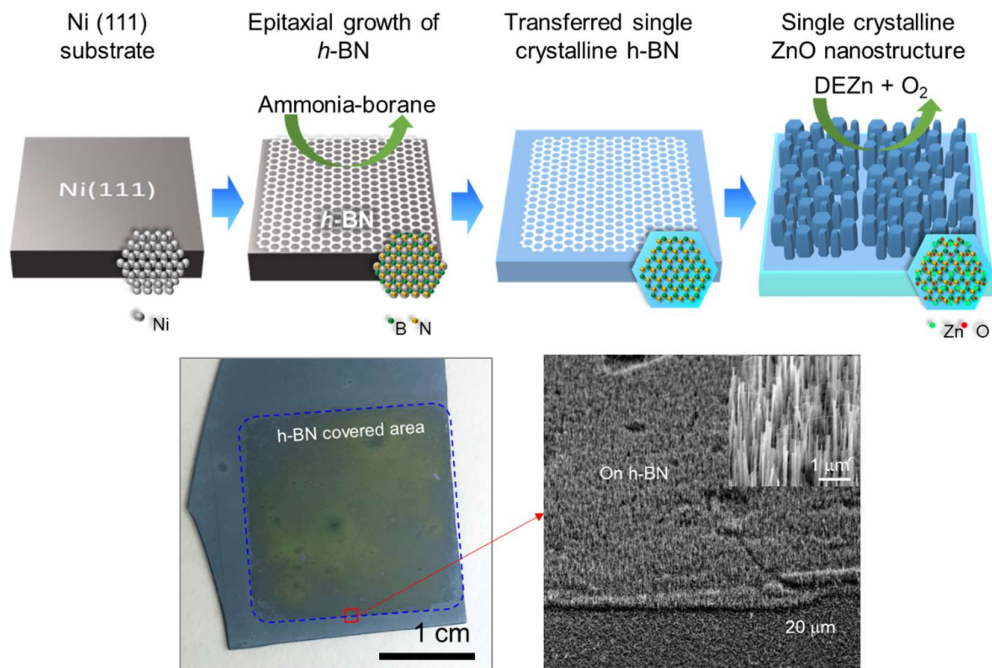


Figure 5.13 Large-scale growth of ZnO nanostructures on the large-scale, single-crystalline h-BN layers. (a) Schematic illustration of the heteroepitaxial growth of ZnO nanostructures on single crystalline h-BN film. (b) The photograph of the ZnO nanostructures heteroepitaxially grown on the single crystalline h-BN film. (c) Tilted-view FE-SEM image of ZnO nanostructures grown on h-BN and SiO₂.

5.6.2. Structural properties of ZnO nanowall network grown on large-scale h-BN layers

Structural properties of ZnO nanostructures depending on the substrates were investigated using x-ray diffraction (XRD) technique. To clarify the effect of the h-BN film as a growth template, diffractions from the ZnO nanostructures grown on amorphous SiO₂ layer was also compared at the same time. Figure 5.14a show the θ - 2θ scan of the ZnO nanostructures grown on (red) the single crystalline h-BN film and (black) the SiO₂ layer, measured in the 2θ range of 25° – 80°. Two strong diffractions appeared at the 2θ of 34.47° and 72.63° from the ZnO/h-BN (red curve), which corresponds to the Bragg reflections of the (002) and (004) planes of the ZnO. The full-width at half maximum (FWHM) of the ZnO(002) peak was 0.11°, indicating high quality of the grown ZnO nanostructures. Importantly, diffraction peaks corresponding to the other planes of ZnO nanostructures were indistinct compared to the background signal. In contrast, multiple peaks corresponding to the ZnO(100), ZnO(101), ZnO(102), ZnO(110) and ZnO(103) planes were observed from the ZnO/SiO₂ (black curve). This indicates that the c-axis orientation of the grown ZnO nanostructures was normal to the surface only if the h-BN film was used as a growth template, suggesting heteroepitaxial relationship of ZnO(002)||h-BN(002).

The in-plane crystal orientations of the ZnO nanostructure investigated by

the azimuthal (ϕ)-scans further reveals the role of h-BN film as an atomically thin epitaxial growth template. Figure 5.14b shows the ϕ -scans of ZnO(101), where ZnO nanostructures were grown on (red) a single crystalline h-BN film and (black) on the SiO₂ layer. The ϕ -scan curves from ZnO/h-BN exhibited six distinct XRD peaks which are separated from one another by 60°. This indicates that ZnO nanostructures grown on h-BN films have single in-plane orientation, due to heteroepitaxial relationship with h-BN. The large full width half maximum (FWHM) of 8.8° presumably resulted from weak interaction between ZnO and h-BN, a distinguished feature of van der Waals epitaxy. Both θ - 2θ and azimuthal scan data indicates that h-BN films served as growth template helped the crystal orientation of grown ZnO nanostructures to be aligned in a single direction, an indirect evidence of heteroepitaxial relationship between h-BN and ZnO.

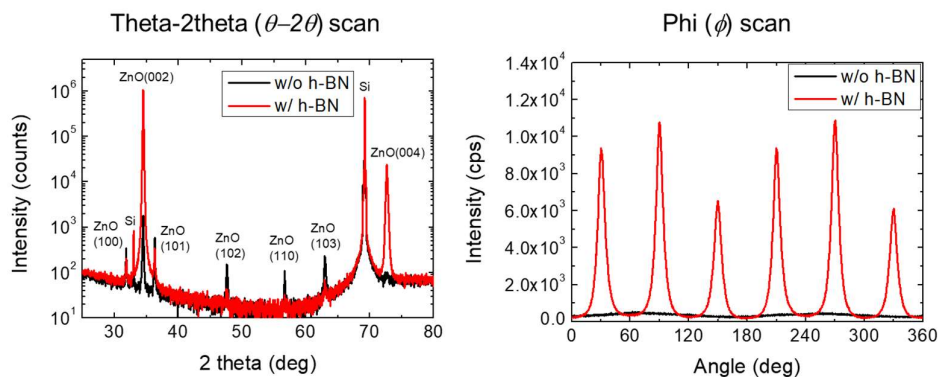


Figure 5.14 Structural properties of ZnO nanostructures grown on single crystalline h-BN film and the SiO₂ layer. (a) $\theta - 2\theta$ scan and (b) ϕ -scan of ZnO {10-11} of ZnO nanostructures grown on (red) the single crystal h-BN layer and (black) the SiO₂ layer.

5.7. Microstructure of GaN thin-film grown on h-BN layers

5.7.1. Introduction

A microstructure of semiconductor thin-films grown on h-BN is of great interest since thin-films can readily be fabricated into practical devices. Generally, defect structures such as grain boundaries or dislocations are known to be degrading the material quality and hence the device performance. Investigation on the microstructures of the thin-films grown on h-BN layers will allow us to understand the growth mechanism, giving an insight to further optimize the material quality. In this chapter, structural investigation and defect analysis of GaN thin-film grown on large-scale, epitaxial h-BN layers will be discussed.

5.7.2. Growth of GaN thin-film on h-BN layers

A transferrable GaN thin-film was grown on large-scale, epitaxial h-BN layers. First, the epitaxial h-BN layers grown on Ni(111) substrate was transferred onto quartz substrates. The growth of GaN thin film was performed using MOCVD system. By employing two-step growth with low-temperature buffer GaN layer, fully coalescent GaN thin-film with smooth surface morphology was grown directly on the h-BN layers. Detailed procedures and growth strategies are introduced somewhere else.^[88]

5.7.2. Microstructure of GaN thin-film grown on epitaxial h-BN

The microstructural properties of GaN on h-BN was first investigated by cross-sectional TEM. Figure 5.15a shows the low-magnification image of cross-sectional TEM specimen. As indicated by white dotted line, layer-by-layer grown high-quality GaN layers grown on the GaN buffer layer consists 400–600-nm-high GaN islands. The total thickness of the thin-film was measured to be 1300 nm. The crystallinity of both layer-by-layer grown area and buffer layer were further investigated. As shown in Figure 5.15b SAED pattern obtained from layer-by-layer grown GaN exhibited a clear array of diffractions with regular period, indicating high crystal quality. From the pattern, it is clear that the Wurtzite GaN is grown with its c-axis normal to the substrate. On the other hand, from the buffer layer we again able to observe Wurtzite structure, while orientations are slightly misaligned in this region. The overall results represent that upon the low-temperature buffer layer, high crystalline GaN thin-films are formed by coalescence of GaN islands under high growth temperature.

Further analysis on the defect structure of the GaN thin film was followed by two-beam dark-field (DF) cross-sectional TEM study. In the two-beam DF images, different types of dislocations are mainly visualized, depending on the orientations of zone-axis with respect to the Burgers vector. In the hexagonal GaN, screw-type and edge-type dislocations have different Burgers vector, i.e. $g = [0002]$ for pure screw dislocations and $[10-10]$ for pure edge dislocations. Mixed-type

dislocations can be seen in both direction^[89]. Figure 5.16a shows a two-beam DF image with $g = [0002]$, mainly showing screw-type dislocations. It is clearly shown that screw-type dislocations are propagating in parallel to the c-axis. Interestingly, majority of these dislocations lies above the islands of the buffer layer, in contrast to the island-free region. On the other hand, in Fig. 5.16b where the image was taken with $g = [10-10]$, edge dislocations can be found (with some mixed-type dislocations), but the density is lower than that of the screw-type dislocations. Laterally propagating edge-type dislocations were also found, which might be resulted from the lateral overgrowth of GaN. Overall, screw-type dislocation primarily contributes the vertical threading dislocations, while the minority are edge-type or mixed-type dislocations. The result contrasts with the case GaN on sapphire substrate, in which pure edge-type dislocations are dominant.^[90]

To determine the density of threading dislocations, plan-view TEM analysis was conducted using GaN films selectively thinned by the focused ion beam technique. Figure 5.17 shows a two-beam DF image of the planar GaN specimen. The cores of dislocations are clearly distinguished in the image, along with the low-angle grain boundaries. The image was taken with $g = [11-20]$ to maximize the visibility of the threading dislocations.^[91] The size of each individual grain ranged from 200 to 1000 nm. The density of threading dislocations was calculated from the single grain, where is green colored in Fig. 5.17. The density was calculated to be $1.0\text{--}4.4 \times 10^9 \text{ cm}^{-2}$, comparable to those of GaN thin-films

grown on MOCVD grown h-BN on sapphire, or on mechanically exfoliated graphene layers.^[21,24] Notably, the density of dislocation is comparable to those of GaN thin films grown on Si substrate, while one or two orders of magnitude larger than those of GaN thin films grown on sapphire or other single crystal substrates, as summarized in Table 5.1.

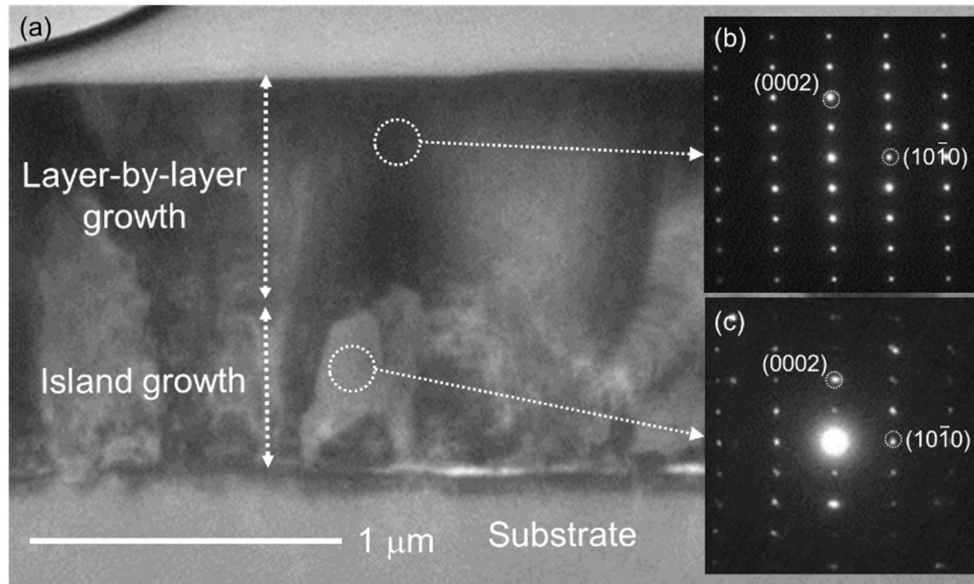


Figure 5.15 TEM analysis of the GaN films grown on large-scale epitaxial h-BN. (a) Low-magnification image of the cross-sectional GaN/h-BN. (b, c) SAED patterns obtained from the low-quality buffer and high-quality thin-film area marked by white dashed circles.

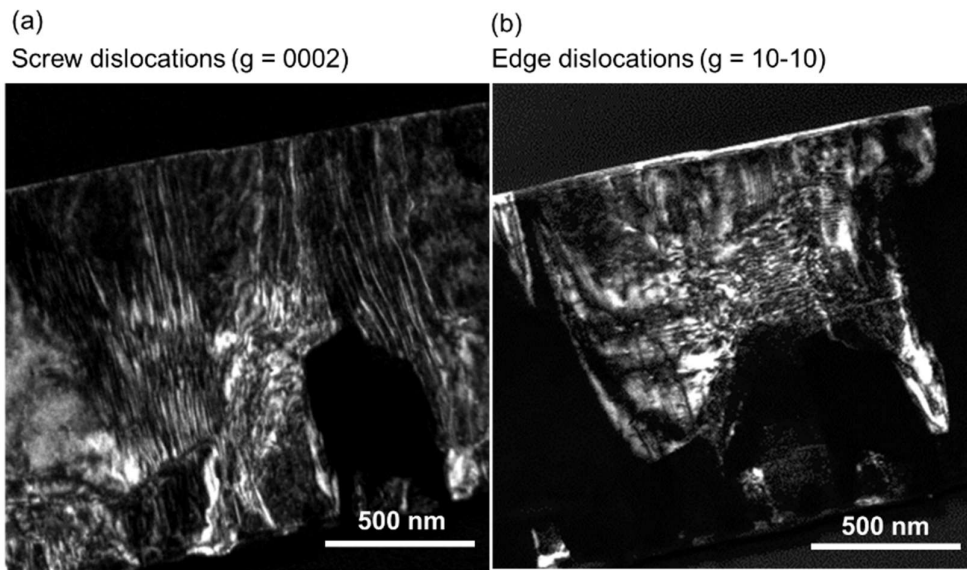


Figure 5.16 Two-beam dark-field images of the cross-sectional GaN thin-film on h-BN, with respect to the different burgers vector. (a) $g = (0002)$ which corresponds to the screw dislocations, and (b) $g = (10-10)$ which corresponds to the edge dislocations.

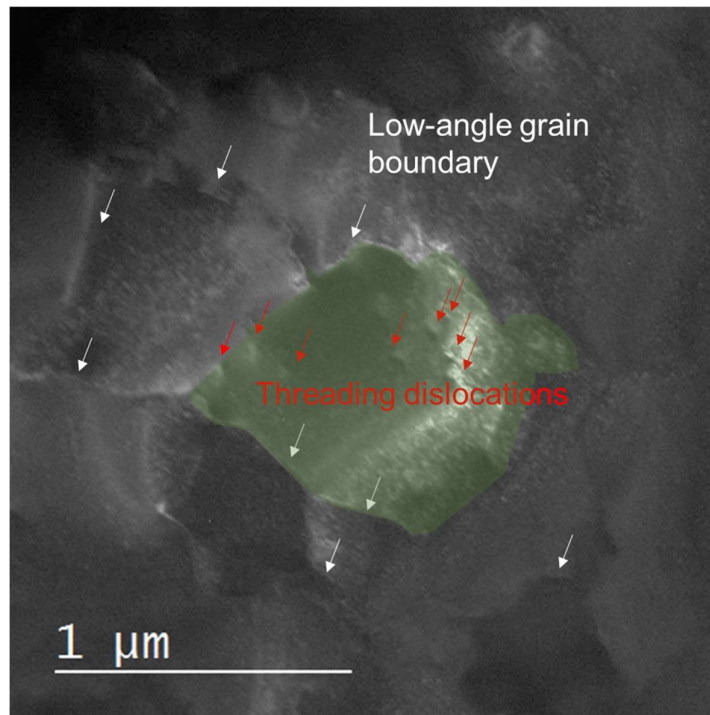


Figure 5.17 Two-beam dark field image of the planar GaN thin-film sample, showing low-angle grain boundaries and threading dislocations.

Table 5.1 Comparison of the density of threading dislocation of GaN thin-films grown on different substrates.

Substrate	TD density (cm ⁻²)	Note	Ref
Sapphire	1 * 10 ⁹	Commercialized	[92]
Patterned sapphire	1 * 10 ⁸		[93]
ELOG sapphire	3 * 10 ⁸		[94]
Si(111) (GaN-on-Si)	10 ⁹	Commercialized	[92]
SiC	5 * 10 ⁸	Commercialized	[92]
Bulk GaN	10 ³ to 10 ⁶	Commercialized	[92]
Multi-layer graphene (MLG) (Mechanically exfoliated)	1.2 – 2.4 * 10 ⁹	Transferrable film	[21]
Multi-layer graphene (MLG) (CVD grown)	1.3 * 10 ⁹ (Only in a single grain)	Transferrable film Average grain size 1 – 10 μm	[23]
Single crystalline CVD h-BN (This work)	1.0 – 4.4 * 10 ⁹ (Plan-view)	Transferrable film Average grain size 0.1 – 1 μm Misorientation angle < 3°	[88]

5.8. Summary

A new approach for fabricating nanoarchitected semiconductors on dielectric h-BN layers was demonstrated using the vdW epitaxy of ZnO nanostructures and selective-area plasma etching of h-BN. The electron microscopic observations exhibited homogeneous epitaxial formation of vertical, single-crystalline ZnO nanostructures on h-BN with abrupt and clean heterointerfaces. The theoretical investigations showed no primary chemical binding features of epitaxial ZnO/h-BN heterostructures with large interfacial spacing and small binding energy. Importantly, artificial atomic ledges of h-BN formed simply by selective plasma treatment enabled the formation of ZnO nanostructures with designed shapes and spatial arrangement. The electrical characterizations revealed excellent electrical insulation properties of h-BN substrates. Ultraviolet photosensor device of the ZnO nanowall networks/h-BN demonstrated the feasibility of h-BN substrate-based device applications. The ability of the vdW heteroepitaxy to allow shape-controlled vertical semiconductor nanostructures on insulating h-BN represents a significant advancement in integration of semiconductors on 2D nanomaterials. More generally, we believe that our route to integrating the semiconductor nanostructures epitaxially on h-BN might be readily expanded to create many other semiconductors/layered insulating (or dielectric) nanomaterials for diverse electronic and optoelectronic device applications.

6. Flexible optoelectronic devices using 1D-2D hybrid nanomaterials: Large-scale, single crystalline ZnO nanostructures on single-crystalline h-BN films and their flexible UV sensor applications

6.1. Introduction

The fabrication of optoelectronic devices on flexible substrates is of great interest for applications to wearable devices^[1,95]. Organic materials^[96,97] and amorphous inorganic films^[98] have been widely used for this purpose due to their low processing temperature and good scalability. These are important features with respect to the ability to employ flexible substrates such as plastic. While higher performance is expected when using single-crystalline inorganic semiconductor nanostructures, their high growth temperatures limit the use of flexible substrates.^[20,24,99–101] This problem can be overcome using 2D nanomaterials as substrates.^[19,56,102,103] These materials have high thermal and chemical stability, meaning that they can be utilized as templates for the growth of inorganic materials, which normally require high temperatures. Furthermore, the strong mechanical strength of 2D nanomaterials allows them to be used in flexible or stretchable applications. Consequently, hybrid heterostructures composed of inorganic

nanostructures on 2D nanomaterials constitute a new class of material systems for developing unconventional inorganic optoelectronic devices in transferable, flexible, or stretchable forms. The systems take full advantage of both inorganic nanostructures and 2D nanomaterials.

However, polycrystalline structures on 2D materials, which are common in large-area synthesized films, can introduce defects into both inorganic nanostructures or the films grown on them. ^[22,23] Such defects can degrade the electronic or mechanical properties of hybrid structures, such as by lowering the band gap energy, increasing the leakage current, or deteriorating the mechanical strength of heteroepitaxially grown nanostructures. Thus, single-crystalline 2D nanomaterials are needed that can fully realize the potential advantages of hybrid heterostructures.

In this study, we fabricated single-domain ZnO nanostructures heteroepitaxially grown on single-crystalline hexagonal boron nitride (h-BN) films. Flexible ultraviolet (UV) sensors were constructed from the as-grown films; these sensors exhibited good, reliable performance even under highly bent conditions.

6.2. Photocurrent characteristics of ZnO nanostructures on h-BN

The electrical properties of ZnO nanowall networks/h-BN heterostructure were investigated by measuring I - V characteristic curves of ZnO nanowall networks, ZnO/h-BN heterojunction, and bare h-BN layer. For the measurements, four Ti/Au bilayer electrodes were prepared, as depicted in Figure 6.1a. The I - V curves of Figure 6.1b show that ZnO nanowall networks with Ohmic Ti/Au electrodes exhibited linear I - V relationship, suggesting high conductivity of ZnO nanowall networks and good Ohmic contacts with Ti/Au electrodes. According to our previous work on thermoelectric power analyses, the carrier concentration of undoped ZnO nanostructures grown under the same MOVPE condition was measured to be $\sim 10^{18} \text{ cm}^{-3}$.^[104] Thus, the ZnO nanostructures grown on h-BN are also expected to exhibit the same background carrier concentration. In contrast, the bare h-BN layer and ZnO/h-BN heterostructure presented excellent insulating characteristics with typical electrical current of $\sim 10^{-12} \text{ A}$ under applied bias voltage range of -5 to 5 V (Figure 6.1a). The leakage current of h-BN layer and ZnO/h-BN heterojunction was quite lower than the typical current measured from the ZnO nanowall networks by 6 or 7 orders of magnitude under the same device dimension condition. This strongly implies that the use of h-BN substrates can be applied to individually operate the nanodevice arrays that are integrated on a piece of substrate for good electrical insulation from neighbor devices.

Based on the ZnO nanowall networks/h-BN heterostructures, the UV photoconductor devices were fabricated with three different electrode configurations, as shown in Figure 6.1a. The time-dependent photoresponses of ZnO nanowall/h-BN heterostructure devices were obtained at a bias of 1.0 V under duty-cycled on/off (20/20 sec) UV irradiation. The UV irradiation from a mercury lamp drastically increased the electrical current of ZnO nanowalls by 20 times (blue solid circles in Figure 6.1c). The mean on/off ratio of photocurrent-to-dark current of the ZnO nanowall photodetector was measured to be $\sim 4-5$, indicating sensitive UV detection of ZnO nanowall networks. In contrast, device configurations of both ZnO-h-BN heterojunction and bare h-BN layer exhibited no clear photoresponses (red and black lines in Figure 6.1c; Figure 6.2), suggesting that the h-BN is a good wide bandgap insulator sufficiently insensitive to the UV irradiation. Accordingly, the photogeneration occurred in ZnO nanowalls and conduction through the nanowall networks significantly contributed to the photocurrent in the UV photosensor of ZnO nanowall/h-BN heterostructure. It is also noted that no photoresponses were observed by indoor light illumination or white radiation from a halogen lamp, indicating that the UV photoconductor device of ZnO nanowall networks/h-BN is sensitive only to the UV light with photon energy higher than the bandgap energy of ZnO.

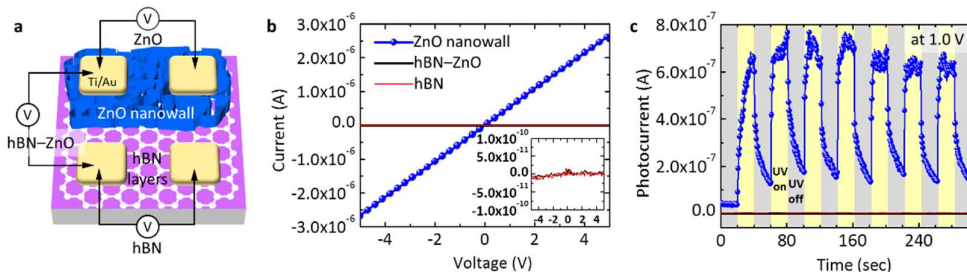


Figure 6.1 UV photoconductor device of ZnO nanowall/h-BN. (a) Schematics of ZnO nanowall network/h-BN photoconductor device with three different electrode configurations. (b) $I-V$ characteristic curves of ZnO nanowall networks, ZnO nanowall/h-BN heterojunction, and bare h-BN layer measured in dark room. Inset is the $I-V$ curves of ZnO nanowall-h-BN heterojunction (black solid line) and bare h-BN layer (red solid line). (c) Time response curve of photocurrent measured at applied bias voltage of 1.0 V.

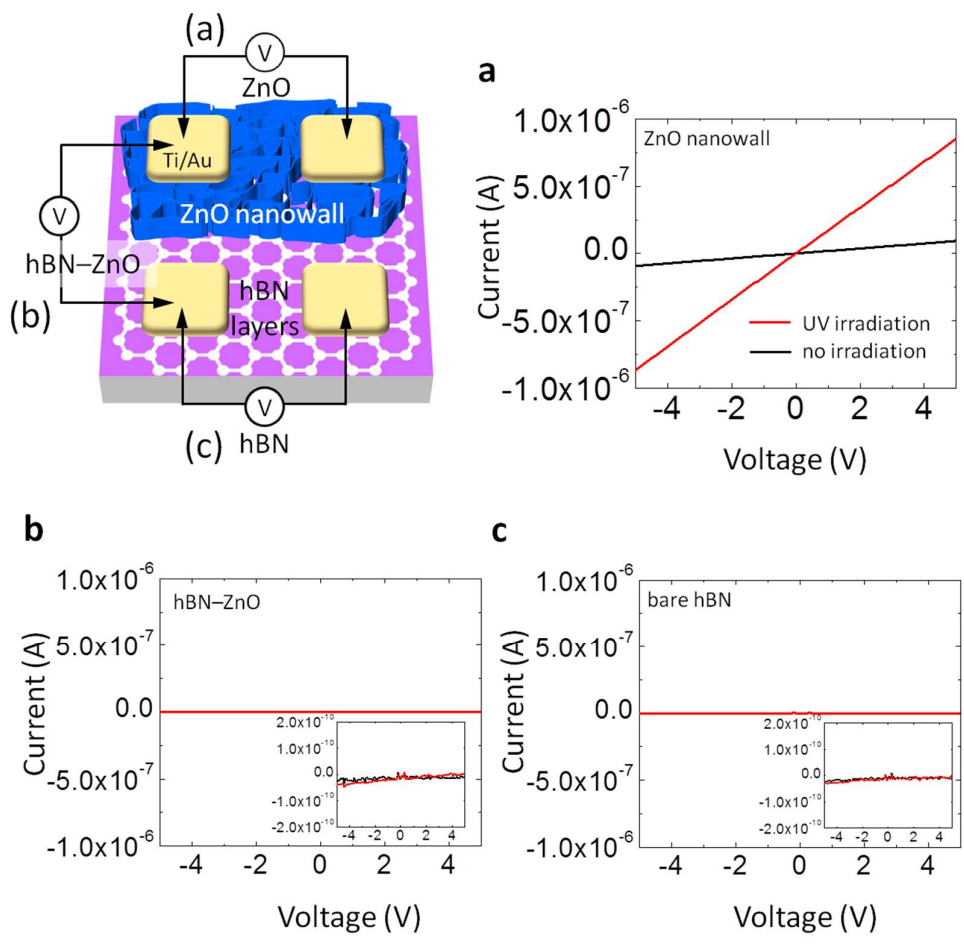


Figure 6.2 I - V characteristic curves of (a) ZnO nanowalls, (b) ZnO nanowall-h-BN heterojunction, and (c) bare h-BN layer measured under UV irradiation (red lines) and (black lines) dark room conditions.

6.3. Photoconductivity of ZnO nanostructures on large scale epitaxial h-BN

To get a better understanding on the potential of differently grown ZnO nanostructure as optoelectronic devices, we measured the current-voltage ($I-V$) characteristics of them under different light illumination. Figures 6.3a and b shows the $I-V$ curves of ZnO nanostructures grown on h-BN film and on a SiO₂ substrate, respectively, in the dark and under illumination of UV lights with different power. In both cases, the curves are symmetrical and linear, indicating that good Ohmic contacts were achieved. At a fixed bias of 1 V, the ZnO/h-BN sample (Figure 3a) exhibited a current level of 0.2 μ A without UV illumination. The current increased as the power of illuminated UV light increases and reached 6.5 μ A when 16.7 mW of UV was illuminated. The I_{UV}/I_{Dark} ratio was calculated to be 70. In contrast, for the ZnO/SiO₂ sample (Figure 3b), the dark current at 1 V under 16.7 mW of UV illumination was 15 μ A, which corresponds to a I_{UV}/I_{Dark} ratio of 10, smaller than that of the ZnO/h-BN. ZnO/h-BN sample exhibited smaller dark current and higher I_{UV}/I_{Dark} ratio compared to the ZnO/SiO₂ sample which indicates that employing the h-BN as substrates can improve the performance of grown ZnO as a UV sensor.

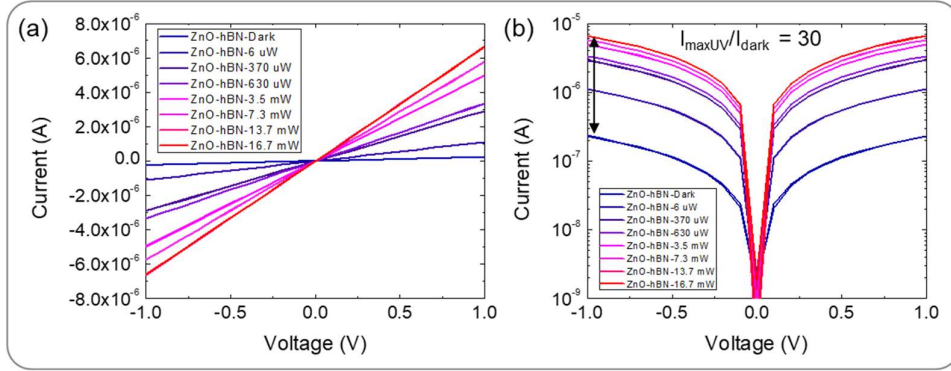
Figure 6.4d shows the spectral response of the device. The red and black curves correspond to the responsivities of ZnO/h-BN and ZnO/quartz, respectively. For the ZnO/h-BN (red curve), the responsivity under UV light (wavelengths: 300

and 350 nm) was about 10^{-1} A/W which then decreased rapidly to 10^{-3} A/W as the wavelength increased into the visible light range (wavelength: 400–550 nm). The responsivity under UV light was about two orders of magnitude larger than under visible light. The ZnO/quartz sample (the black curve) exhibited similar behavior. The UV and visible light responsivities were 10^0 and 10^{-2} A/W, respectively. The R_{UV}/R_{Vis} ratio was 90, which was slightly smaller than that of ZnO/h-BN. This result implies that MOCVD-grown ZnO nanostructures are suitable for the selective detection of UV light, while simultaneously minimizing the response to visible light.

Figure 6.5a shows the photoresponse switching behavior of the as-grown ZnO films on h-BN and quartz substrates, measured by periodically turning the UV light on and off for a period of 30 s, under an applied bias voltage of 1 V. In the case of the ZnO/h-BN sample (the red curve), the stationary current of ZnO/h-BN was on the order of 10^{-9} A. When illuminated with UV light, the photocurrent dramatically increased to the order 10^{-6} A and was then maintained at this level. When we turned the UV off, the current decreased rapidly to the level of 10^{-9} A again. The switching behavior was stable and reproducible over repeated operation. Recovery time, defined as the time required for the current to reduce to $1/e$ or 36.8% of its value, was 0.1 s. The high I_{ON}/I_{OFF} of 10^3 and small recovery time indicates that the ZnO/h-BN has excellent characteristics for photodetector applications. Meanwhile, the ZnO/quartz sample (the black curve) exhibited a higher off current

of 10^{-7} A, a smaller $I_{\text{ON}}/I_{\text{OFF}}$ of 50, and a longer recovery time of 0.4 s; the switching behavior was also stable and reproducible.

ZnO on h-BN



ZnO on SiO₂

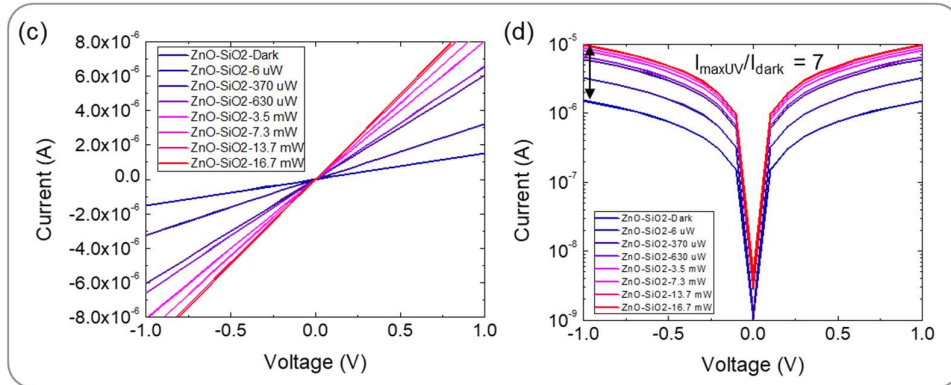


Figure 6.3 Power-dependent photocurrent characteristics of ZnO nanostructures grown on h-BN or SiO₂ substrates. (a) Linear and (b) semi-log plot of the I - V characteristics of ZnO/h-BN. (c) Linear and (d) semi-log plot of the I - V characteristics of ZnO/SiO₂.

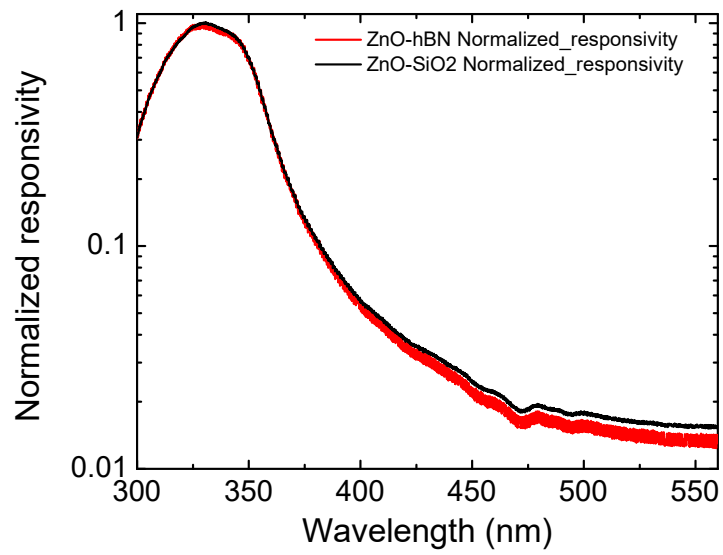
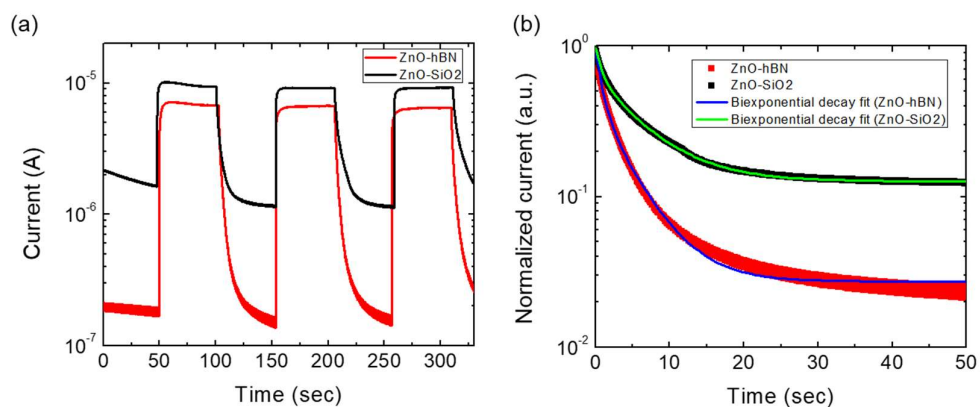


Figure 6.4 Normalized spectral response curves of ZnO nanostructures grown on h-BN and SiO₂ substrates.



(c)

	Dark current	A ₁ : Fast decay (electron-hole recombination)		A ₂ : Slow decay (O ₂ desorption)	
		y ₀	A ₁	t ₁	A ₂
ZnO/h-BN	0.02741	0.51051	0.93348	0.38345	4.39613
ZnO/SiO ₂	0.12637	0.33682	0.87805	0.50318	6.16932

$$y = y_0 - A_1 e^{-x/t_1} - A_2 e^{-x/t_2}$$

Figure 6.5 Temporal response and decay curve fitting of the photocurrent in ZnO/h-BN. (a) Temporal response of the ZnO nanostructures on h-BN and SiO₂ substrates. (b) Normalized decay behaviors of the ZnO nanostructures on h-BN and SiO₂ substrates, with biexponential decay fitting curves. (c) Factors of biexponential decay models of the photocurrent in ZnO/h-BN and ZnO/SiO₂, calculated from the fitting curves in (b).

6.4. Fabrication of the flexible UV sensor using ZnO/h-BN heterostructures

Further, the layered structure of the single-crystalline h-BN films enabled the fabrication of flexible UV sensors by a simple mechanical releasing process; the basic process is shown in Figure 6.6a. To avoid mechanical damage to the ZnO nanostructures as they are bent, we patterned continuous ZnO nanostructures on h-BN films onto a microdisk array. Thin Au inter-digit electrodes were deposited on the ZnO microdisk array, to electrically connect each individual ZnO microdisk by Schottky contacts. As an essential step for creating a flexible device, the fabricated sensors were transferred onto a polyimide (PI) substrate by a mechanical lift-off process. Figures 6.6b and c show optical microscopy images of the device on a rigid SiO₂/Si substrate (before transfer) and on the flexible substrate under a bending radius of 5 mm (after transfer). As shown in Figure 6.6c, even under the flexed configuration, the mechanical stress applied to each ZnO microdisk was sufficiently low for it to maintain its local structural integrity.

We then investigated the performance of the fabricated flexible UV sensor under different bending radii. Figure 6.6d shows the I - V characteristics of the device with and without UV illumination, under different bending radii. Under dark conditions, the current levels were on the order 10^{-10} A at an applied bias of 5 V for all bending conditions. When exposed to UV irradiation, the currents in the device

increased by 1.5 orders of magnitude, regardless of the bending radius. The linear plots shown in the inset confirm that currents increased nonlinearly as the voltage increased, due to the Schottky barriers formed at the junctions between the ZnO nanostructures and Au electrodes.

Figure 6.6e shows the time-dependent responses to UV light under different bending radii of infinity, 10, and 5 mm. The current increased rapidly when the UV light was switched on and decreased rapidly when the UV light was turned off. For all cases, the on-off ratio was more than 50. The recovery time ranged from 0.2–0.5 s, which is still faster than most other devices. The fact that similar results were observed under different bending conditions suggests that no significant damage was applied to the ZnO nanostructures and h-BN films under flexible conditions.

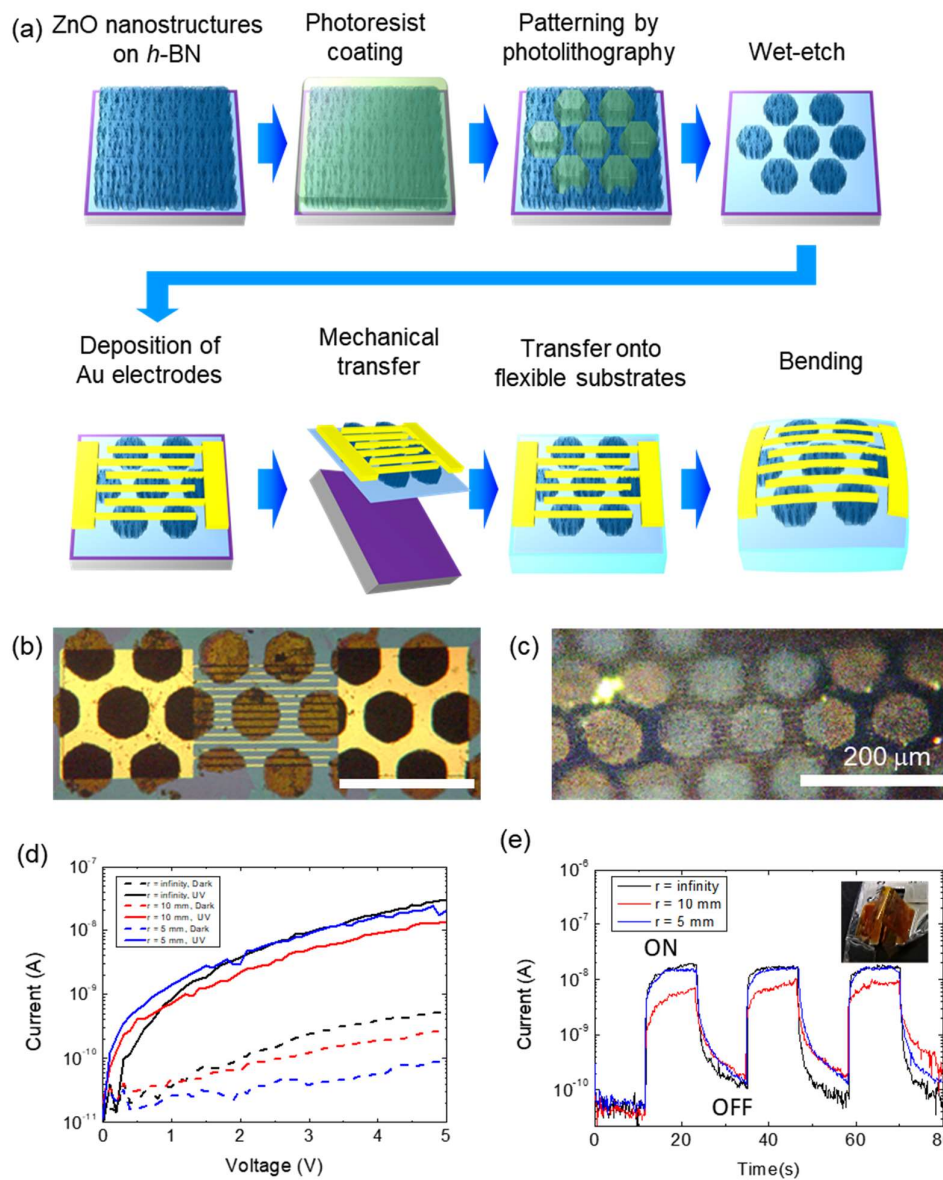


Figure 6.6 Schematic diagram of the process for fabricating flexible UV sensors using ZnO/*h*-BN heterostructures. (b, c) Photographs of the fabricated flexible UV sensor (b) as fabricated and (c) transferred onto flexible substrates and bent. (d) I-V characteristics of the flexible UV sensor

under dark and UV-illuminated conditions. (e) Time-dependent photocurrent behavior of the flexible UV sensors under different bending conditions.

6.5. Summary

In summary, we fabricated large-scale, single-crystalline ZnO nanostructures using heteroepitaxial growth on centimeter-scale, single-crystalline *h*-BN films. Vertically aligned ZnO nanowall networks were formed only on *h*-BN films, while randomly oriented nanoneedles were observed on amorphous SiO₂ substrates. The XRD study indicates that the as-grown ZnO nanostructures were single crystalline over a large area, with their *c*-axis normal to the surface. The photocurrent study under UV illumination revealed that the ZnO nanostructures grown on single-crystalline *h*-BN substrates exhibited a higher I_{\max}/I_{\min} ratio of 10^3 – 10^4 , which is two orders of magnitude higher than those from the ZnO grown without *h*-BN substrates. To demonstrate the functionality of the ZnO/*h*-BN hybrid material system, flexible inorganic UV sensors were fabricated by patterning the ZnO nanostructures, followed by a mechanical transfer process. The fabricated sensor exhibited a strong and stable response to UV illumination, even under a small bending radius of 5 mm. In general, we believe that the approach used in this study could be readily expanded to create high-performance, flexible optoelectronic devices based on inorganic material systems.

7. Flexible electronic devices using 1D-2D hybrid nanomaterials: Vertical field-effect transistor (VFET) using ZnO nanotubes on graphene layers

7.1. Introduction

Flexible electronic devices have recently attracted much attention for use in wearable displays, sensors, and biomedical devices.^[1] For the flexible devices, organic films have widely been employed due to their excellent scalability and flexibility.^[105,106] However, there are unresolved issues associated with organic material based electronic devices; their electrical characteristics and long-term stability are poor. Single crystalline inorganic materials have been used in a wide range of high-performance electronic devices. For example, semiconductor nanowire-based field-effect transistors exhibit excellent properties, such as high carrier mobility, a large I_{\max}/I_{\min} ratio, and a small subthreshold swing.^[69,107,108] However, these nanowires must be grown on a single crystalline substrate, such as silicon (Si) or silicon carbide (SiC), hindering their utility in applications where flexible substrates are required.^[109–111] Graphene films are used as substrates for inorganic materials when we wish to then transfer the materials onto another substrate, such as one that is suitable for use in a flexible device. Due to its layered structure, it is easy to transfer inorganic materials fabricated on graphene film onto

foreign substrates, such as metal or plastic.^[19,20,56] In this chapter, we report the fabrication of vertical field effect transistor (VFET) using ZnO nanotubes on a graphene film for flexible inorganic electronics.

7.2. Fabrication of the ZnO nanotube VFET on graphene layers

The position-controlled ZnO nanotubes grown on graphene films were employed for the fabrication of flexible inorganic VFETs. The graphene films were synthesized on copper (Cu) foils using chemical vapor deposition (CVD) and then transferred onto Si substrates.^[112,113] We obtained nanotube growth selectivity by depositing a silicon dioxide (SiO₂) growth mask layer onto the graphene film using plasma-enhanced CVD and then patterning a sub-micron hole array into the mask layer using conventional *e*-beam lithography and etching techniques. Catalyst-free CVD was used to grow the ZnO nanotubes on the patterned holes.^[104] The scanning electron microscopy (SEM) images in Figure 7.1(a) clearly show that the resulting regular hexagonal arrays of ZnO nanotubes had well-controlled diameters and spacings. In addition, we controlled the length of the ZnO nanotubes by varying the growth time and temperature. For instance, when the growth temperature was 650°C, the typical growth rate was approximately 34 nm/min. All of the dimensional parameters of the nanotubes can be controlled either by simply changing the lithographic pattern mask or adjusting the growth parameters of the metal organic CVD (MOCVD) process. In this work, ZnO nanotubes with an outer

diameter of 300 nm and a height of 5 μm were typically employed for the fabrication of VFET. More importantly, the nanotube array and devices could be very easily transferred onto foreign substrates for flexible electronic devices.

We used cross-sectional transmission electron microscopy (TEM) to evaluate the microstructural characteristics of the ZnO nanotubes grown on CVD-graphene films. For this analysis, cross-sectional TEM specimens for a ZnO nanotube/graphene film/SiO₂/Si samples were prepared using a focused-ion beam (FIB) technique. As shown in Figure 7.1b, the regular spots on the selected-area electron diffraction (SAED) pattern of the ZnO nanotubes indicate that the ZnO nanotubes are single crystals. In the SAED pattern, the (0001) planes are parallel to the direction of nanotube growth, indicating the ZnO[0001] growth direction. The high-resolution TEM (HRTEM) image in the inset also shows a highly ordered lattice structure. From the images, the lattice spacing between adjacent planes is estimated to be 0.52 nm, which corresponds to the *d*-spacing of the (0002) planes. Furthermore, we examined multiple HR-TEM images of all of the ZnO nanotubes, and found no crystal defects, such as dislocations or stacking faults. This indicates that these ZnO structures were very high quality single crystals.

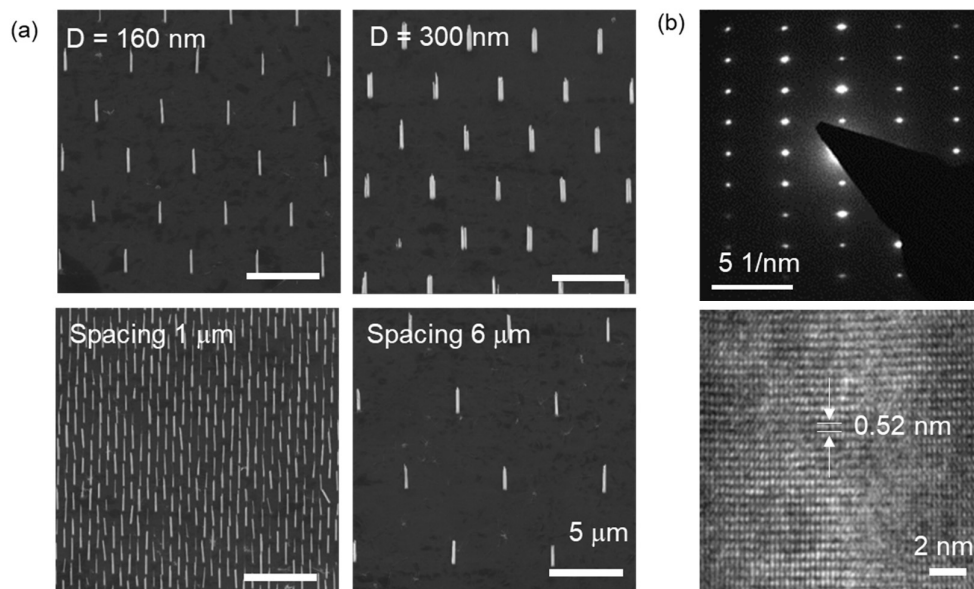


Figure 7.1. ZnO nanotubes grown on graphene layers and its structural properties. (a) Tilted-view scanning electron microscopy (SEM) images of the position- and dimension-controlled ZnO nanotube arrays. Hexagonal nanotube arrays with diameters of (top-left) 160 nm and (top-right) 300 nm and arrays with spacings of (bottom-left) $1 \mu\text{m}$ and (bottom-right) $6 \mu\text{m}$. (b) (top) Selective area electron diffraction (SAED) image of a ZnO nanotube. (bottom) High-resolution transmission electron microscopy image of a ZnO nanotube.

Figure 7.2a shows a schematic diagram of the strategy developed for fabricating VFETs from position-controlled ZnO nanotubes arrays grown on graphene films. First, a large CVD graphene film is placed on highly-doped Si; this acts as the bottom electrode. Then, catalyst-free CVD is used to grow position-controlled ZnO nanotubes on an SiO₂ film growth mask layer. The nanotube VFET consists of a vertical channel through a single ZnO nanotube, a surrounding silver (Au) gate electrode, and a thin polyimide (PI) layer that acts as the gate dielectric layer. The surrounding gate dielectric PI and Au electrode layers are the most critical parts of the VFET structure. We use spin-coating and thermal evaporation, respectively, to coat the ZnO nanotube with the PI and Au layers. Here, the first PI layer serves as both a spacer layer and a surrounding dielectric layer. We remove the upper part of the Au electrode, as shown in Figure 7.2b, and coat the VFET with a second layer of PI to ensure that the gate electrode is electrically separated from the drain electrode. The drain electrode is fabricated by exposing the tip of the ZnO nanotube to air by oxygen plasma etching, and then depositing a titanium (Ti)/Au bi-layer onto it by *e*-beam evaporation. Then, the second PI layer is removed from the gate electrode by oxygen plasma etching. This ensures that the gate electrode is exposed for easy probing, as shown in Figure 7.2c.

The microstructure of a nanotube VFET was investigated using cross sectional FE-SEM. The FE-SEM image in Fig. 7.2d shows that the ZnO nanotube grew on the graphene/Si substrate through a patterned hole with a diameter of 300

nm. The space between the ZnO nanotube and the Au gate layer is filled with the first PI layer. The first PI layer has an inverted funnel shape and surrounds the ZnO nanotube. The minimum distance between the nanotube and the gate electrode is 50 nm, as indicated by the arrow. The additional space between the drain and gate electrodes is filled with the second PI layer, which is 1- μm thick. The minimum distance between the drain and gate electrodes near the ZnO nanotube is 350 nm, which is thick enough to prevent a short circuit. The drain electrode is coated onto the surface of the tip of the ZnO nanotube, which protrudes from the second PI layer.

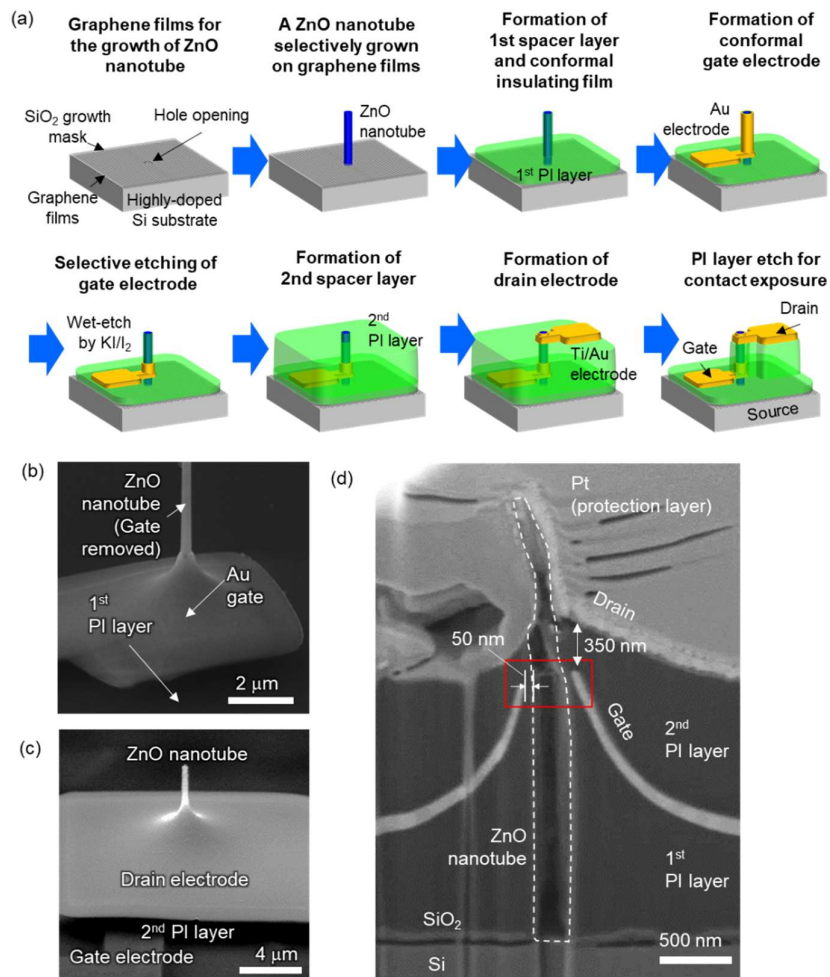


Figure 7.2. Fabrication of the ZnO nanotube VFET and its structure. (a) Schematic diagram of the process used to fabricate the vertical field effect transistor (VFET) arrays using the ZnO nanotube heteroepitaxially grown on graphene layers. Field-emission SEM (FE-SEM) images of a ZnO nanotube array on a graphene substrate (b) after formation of conformal gate electrodes, and (c) after fabrication of the VFET structure. (d) Cross-sectional FE-SEM image of the nanotube VFET.

7.3. Electrical characteristics of the nanotube VFET

We evaluated the electrical characteristics of the ZnO nanotube VFET by measuring the gate bias (V_{gs})-dependent current density (I_{ds}) characteristics. Figure 7.3a shows the V_{gs} - I_{ds} curves of the nanotube VFET for drain-source voltage (V_{ds}) values of 5 and 7.5 V. The current decreases continuously as the gate voltage increases negatively. These transfer characteristics indicate that the nanotube VFET behaves as a typical n -channel FET and operates in a depletion (normally on) mode. The current drops dramatically, to the order of 10^{-7} A/ μm , as V_{gs} decreases beyond -15 V, which is the threshold voltage (V_{th}) of the device. We observed a high I_{max}/I_{min} ratio of 10^6 ; this is an order of magnitude higher than the previously reported value.^[110] The minimum subthreshold swing is 110 mV/dec, which is smaller than the previously reported value (170 mV/dec) for a ZnO nanowire based n -channel VFET.^[110] The low subthreshold slope indicates that the device can be turned off without consuming a large amount of power. The transconductance, which is the derivative of the transfer curve ($g_m = dI_{ds}/dV_{gs}$), is another key indicator of transistor performance. The maximum values of the transconductance peaks near the subthreshold region are 75 and 170 nS μm^{-1} when V_{ds} is 5 and 7.5 V, respectively.

Figure 7.3b shows the current-voltage (I_{ds} - V_{ds}) characteristics (output characteristics) for V_{ds} ranging from 0 to 10 V for various values of V_{gs} : 0, -5, -10, and -15 V. The nanotube VFET is normally on, and I_{ds} decreases as V_{gs} increases negatively. The device turns off when V_{gs} is -15 V, which is the threshold voltage.

The leakage current is 10^{-4} $\mu\text{A}/\mu\text{m}$. The output characteristic clearly indicates that the nanotube VFET works as a typical n -channel FET^[104,114]. The depletion-mode operation of the device is attributed to the as-grown n -type ZnO^[115,116]. However, the $I_{\text{ds}}-V_{\text{ds}}$ curves show that I_{ds} increases rapidly with V_{ds} , which is similar to the output characteristics of catalyst-assisted ZnO nanowire FETs.^[110] The absence of I_{ds} saturation indicates that neither traditional channel pinch-off nor carrier velocity saturation are relevant to the operation of this nanotube VFET.

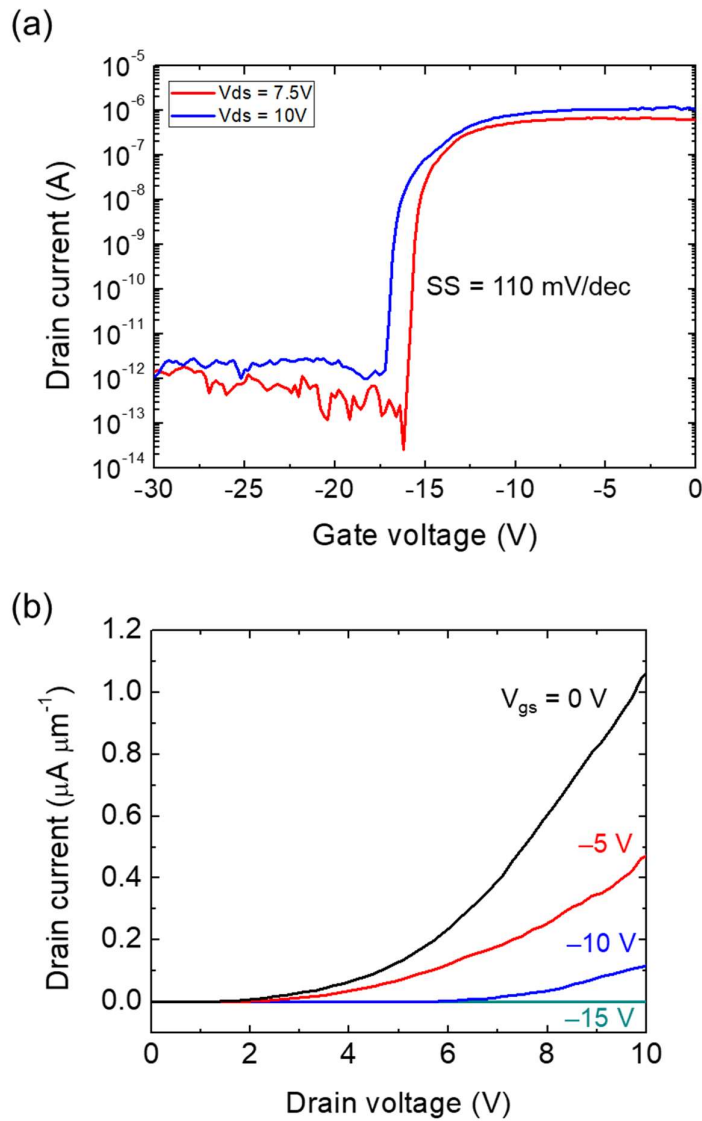


Figure 7.3 Electrical characteristics of the fabricated VFET. (a) $I_{ds} - V_{gs}$ transfer characteristic curves of the VFETs. (b) $I_{ds} - V_{ds}$ output characteristic curves of the VFET.

7.4. 3D device simulation

We investigated the electrical characteristics of the ZnO nanotube VFET in more detail by running three-dimensional (3D) simulations developed using Atlas (Silvaco), a commercially available software package. Figure 7.4a shows the model used in these simulations for the structure of the nanotube VFET. The ZnO nanotube is modeled as a hollow tube with a uniform diameter and shell thickness. The inside of the ZnO nanotube is filled with air, and the outer surface is covered with a uniform layer of PI. The two tips of the nanotube act as the source and drain electrodes. As the main contribution from the gate electrode to the total gate capacitance comes from the tip (marked by the red box in Figure 7.2) close to the channel, we simplify the gate electrode to a narrow ring. As shown in Figure 7.4b, there is very good agreement between the simulated transfer curves and the measured values. This high level of agreement between the simulated curves and experimental data validates our results concerning the nanotube VFET and provides strong evidence that it is possible to fabricate electronic devices using one-dimensional (1D) semiconductor nanostructures on two-dimensional (2D) nanomaterials.

Our simulation of the nanotube VFET provides a clear explanation for its transistor characteristics: the distribution of electron carriers changes when a gate bias voltage is applied. Figure 7.4c shows the 3D and 2D contour maps of the carrier concentrations for V_{gs} values of -8 , -12 , -13 , -14 and -15 V when V_{ds} is fixed at

5 V. The 3D contour maps show that the carrier concentration only changes in the region surrounded by the gate electrode (marked by a grey box), which is the channel region. According to the 2D contour maps, the carrier concentration is lowest at the outer surface and increases towards the inner surface. The carrier concentration in the channel region decreases rapidly with V_{gs} . In terms of electron accumulation and depletion, accumulation (or depletion) regions are indicated by the red-colored region representing $n > 10^{18}\text{cm}^{-3}$ (or violet-colored region representing $n < 10^{13}\text{cm}^{-3}$) in the contour plot in Figure 7.4c. The depletion region when V_{gs} is -8 V is 30% (inset of the 2D contour map). However, it increases dramatically, by 60 %, when V_{gs} is varied from -8 V to -12 V . The entire channel becomes depleted when $V_{gs}-V_{th}$ decreases to -15 V . These results show that the nanotube VFET has excellent transistor characteristics, *i.e.*, a small subthreshold swing and a high I_{max}/I_{min} ratio.

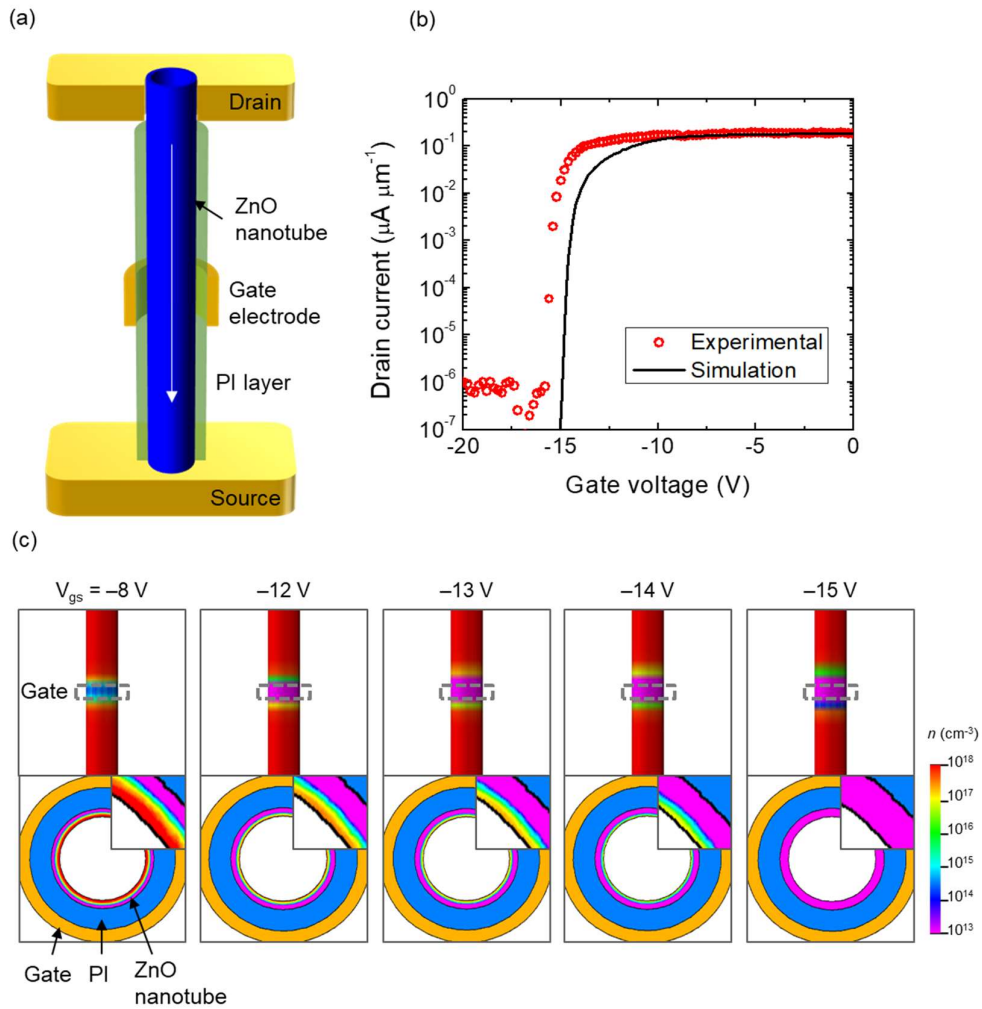


Figure 7.4 3D simulation of the ZnO nanotube VFET. (a) Simplified model of the nanotube VFET used in transport simulation. (b) Transport simulation of the nanotube VFET and comparison to experimental data. (c) Distribution of the carrier concentration in the ZnO nanotube at different gate biases, according to the results of our simulation.

7.5. Flexible device applications

We fabricated flexible VFETs by transferring the devices onto foreign plastic substrates. Figure 7.4a shows a schematic diagram of the device transfer process. A 5- μm -thick poly(methyl methacrylate) (PMMA) layer is spin-coated, then PI tapes are attached to each edge of the sample. The PMMA/PI(VFET)/graphene film can easily be mechanically peeled off the substrate. Cr and Au thin films with thicknesses of 10 and 20 nm were deposited at the graphene film side to reduce contact resistance of the source electrode. The device is then placed onto a foreign substrate, which in this case is a 25- μm thick polyethylene (PE) film. After transfer, the PMMA layer was removed in an acetone bath. Due to the transferability of graphene film, we can use any arbitrary substrate, including a flexible plastic film or human skin, as shown in Figure 7.4b. The device showed no signs of mechanical damage, even after bending and stretching.

We investigated the electrical characteristics of the nanotube VFET transferred onto the flexible substrate. Figure 7.4c shows the $I_{\text{ds}} - V_{\text{gs}}$ transfer curves of the VFET measured before (black) and after (red) transfer. The device maintains good transistor characteristics after transfer, such as high $I_{\text{max}}/I_{\text{min}}$ ratio of $\sim 10^6$. These are not significantly different to the pre-transfer values, although the threshold voltage shifted by -3 V and the subthreshold swing increased from 110 to 600 mV/dec. The device fabrication processes can be optimized to improve the characteristics of the flexible device. This result indicates that the nanotube VFET

remains operational as it is bent, so it can be used in flexible and wearable devices.

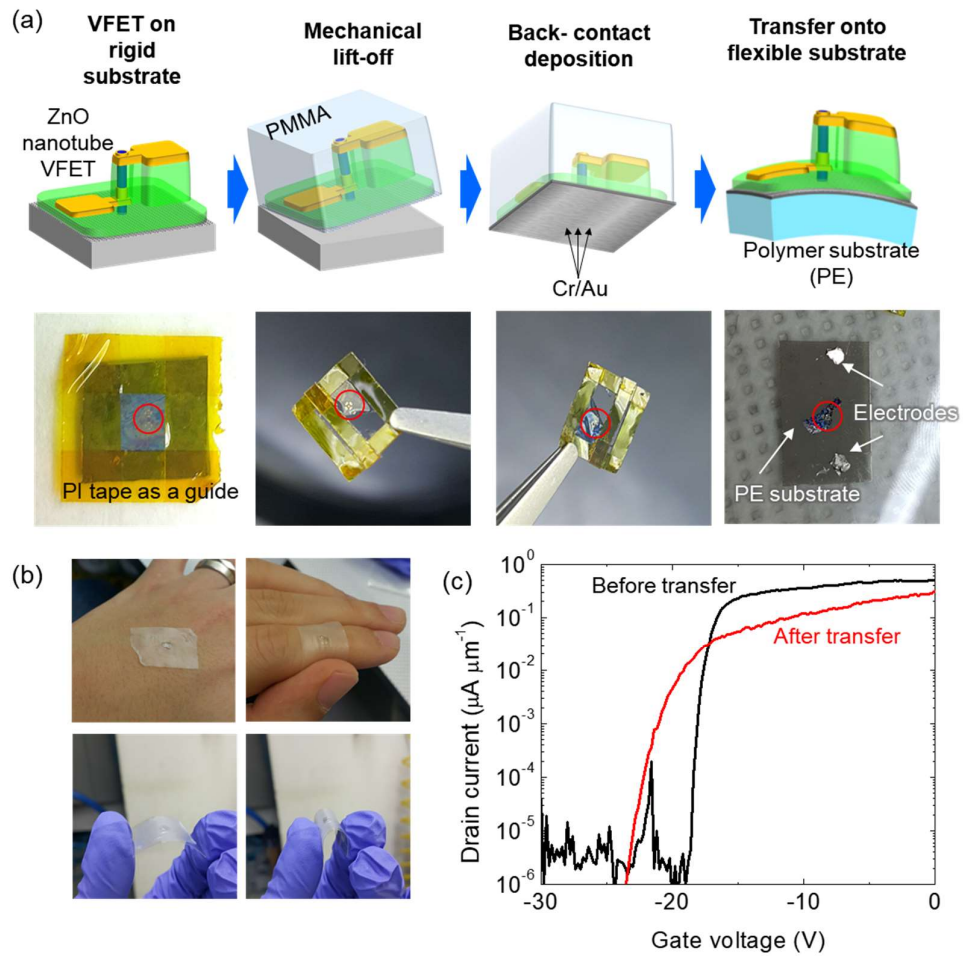


Figure 7.4 Mechanical transfer of the fabricated VFET onto flexible substrate. (a) Schematic diagram of the process used to fabricate flexible VFETs with mechanical lift-off. (b) Photographs of the device transfer process. (c) Transfer curves of the nanotube VFET before and after transfer.

7.6. Summary

In conclusion, we fabricated flexible nanotube VFETs using defect-free, single crystal ZnO nanotubes grown on graphene films. The resulting VFET exhibited excellent transistor performance, with a high I_{\max}/I_{\min} ratio of 10^6 and a small subthreshold slope of 110 mV/dec. The operation and excellent transistor characteristics of the nanotube VFET numerically were validated using a simulation based on a 3D model of the device. Furthermore, the layered structure of the graphene film enables us to transfer these devices onto arbitrary foreign substrates, such as a PE film or human skin. The device maintained excellent transistor characteristics after it was transferred onto a flexible substrate. More generally, we believe that the simple bottom-up integration of vertical 1D nanostructure devices on 2D nanomaterials can be readily expanded to develop many other flexible and wearable electronic devices.

8. Conclusion and outlook

8.1. Summary

The main objective of this dissertation is to study the hybrid nanomaterial system based on h-BN as a platform for functional electronic and optoelectronic devices with inorganic channels. In the beginning of the research, synthesis of single crystalline, large scale h-BN layer and its structural and physical characteristics were investigated. For the fundamental studies, thorough studies on the mechanism of heteroepitaxial growth on h-BN, as well as microstructural analysis were carried out using TEM and SR-XRD. For the applications, flexible UV sensor using ZnO/h-BN heterostructure was demonstrated, by utilizing the layered structure of the h-BN layers. Furthermore, as a novel electronic device, flexible vertical field effect transistor was fabricated using ZnO nanotubes grown on graphene layers. While graphene was used as a substrate, the work can be readily integrated with h-BN. The details of experimental achievements and their implications are summarized as follows.

(1) Repeatable synthesis of single-crystal, large-scale h-BN layers:

- While it was well known that single crystalline h-BN layers can be heteroepitaxially grown on Ni(111) substrates, separation of the grown

h-BN layers remained as a challenge. Due to the high-cost of the single crystalline Ni(111) substrates, conventional method to separate the grown 2D nanomaterials – dissolving the metal substrates – cannot be generally used. In this dissertation, by combining the electrochemical delamination method with the heteroepitaxial growth of h-BN on Ni(111), single crystalline, large scale h-BN layers can be repeatedly grown from the single Ni(111) substrate. The method allowed to re-use the substrate for more than 10 times, which significantly reduce the cost of experiment. Multiple characterizations including structural, chemical, optical and electrical characterization revealed that the grown film is of single crystalline over the entire area and exhibits typical properties of the h-BN including excellent insulating properties.

(2) Investigation on the heteroepitaxial growth on h-BN layers:

- The heteroepitaxial growth on the surface of h-BN layer is of great interest, since the surface of the h-BN has no dangling bonds in contrast to the conventional substrates. Due to the lack of dangling bonds, the principle of heteroepitaxial growth on h-BN is found to be different from that of conventional heteroepitaxy.
- In the dissertation, the heteroepitaxial growth of semiconductor nanostructures on h-BN layers were thoroughly investigated. Especially,

microstructural analysis on the heterointerface revealed the unique features such as atomically clean interface. In-plane analysis suggested that there is no rotation of crystal orientation, regardless of large lattice match. Supported by the first-principle simulation, these features are found to be resulted from the dangling bond free surface of the h-BN where heteroepitaxy is mediated by van der Waals force.

- For the thin-films (GaN) grown on h-BN layers, defect analysis using cross-sectional TEM revealed that most of the defect are screw dislocations, in contrast to the thin-film grown on conventional (sapphire) substrate in which edge dislocation dominates. Threading dislocation density of the GaN on h-BN was in the order of $10^9/\text{cm}^2$, which is one-two order higher those on sapphire and comparable to the case of GaN on Si. The result indicates that GaN thin films on h-BN is good enough for the device application, when further optimization is followed.

(3) Fabrication of flexible optoelectronic device using ZnO/h-BN heterostructure:

- Advantage of using h-BN as a substrate rather than graphene is that channels can be formed along to the lateral direction. However, most functional devices made of h-BN based hybrids are vertical structured, which does not fully utilize the insulating properties of h-BN. In this

dissertation, flexible UV sensors were fabricated using ZnO/h-BN heterostructure followed by mechanical transfer. The research demonstrated the way of utilizing unique features of h-BN based hybrids such as flexibility and transferability.

(4) Fabrication of flexible electronics using ZnO/graphene heterostructure:

- Most applications of 2D nanomaterial-based hybrids remained on optoelectronic devices such as LED, light sensor or solar-cell. Due to the complexity of device configuration – at least three electrodes including source, drain and gate – electronic devices using 2D nanomaterial-based hybrids were rarely researched yet. In this dissertation, flexible vertical FET was fabricated using the ZnO nanotube grown on graphene layers. Up to the best of the author’s knowledge, this work is the first demonstration of flexible vertical-channel nano-FET.
- The fabricated device exhibited excellent electronic characteristics, such as high I_{\max}/I_{\min} ratio of 10^6 and small leakage current from the gate. Especially, thanks to the 3D surrounding gate structure, the fabricated VFET exhibited small subthreshold swing of 110 mV/dec. The operation of a vertical nanotube channel was further investigated by 3D Silvaco simulation. From the simulation, it was found that the inner wall of the ZnO nanotube mostly contributes the on current of the device.

8.2. Future works and outlook

This research demonstrated the feasibility of h-BN based hybrid nanostructures for electronic and optoelectronic devices. However, still there is room for the improvement of the material quality, as well as and device performance to be used in practical applications. Several critical issues are remaining. Accordingly, to fully realize the potential of h-BN based hybrids, further studies should be followed. We also expect that the following research can be expanded to other material/device applications.

(1) Synthesis of single crystal h-BN layers with controlled number of layers:

- The combination of heteroepitaxial growth on h-BN on Ni(111) with electrochemical delamination has opened up a way to reliably produce single crystalline, large-scale h-BN layers. However, the number of h-BN layer was fixed to 8 – 10 layers and hard to be controlled. The study on the growth behavior revealed that multiple h-BN islands nucleated first then merge with each other to form a continuous film. To overcome the challenge, the growth condition should be thoroughly studied to find the desired condition for each number of layers.
- While the synthesized h-BN is ‘single crystalline’, it is difficult to say ‘single-crystal’ because of the existence of mirror domains. The h-BN crystal has a 3-fold symmetry, and therefore there is a possibility that

mirror domain exists. However, such a mirror domain is very difficult to be differentiated with each other, since they would result in same diffraction patterns when illuminated by x-ray or electron beam. On the other hand, these mirror domains can be distinguished at the nucleation stage, since the direction of unique triangular patch of h-BN differs by 180°. By careful investigation of the nucleation stage, it would be possible to find a specific growth parameter which would yield uniformly ordered, single crystal h-BN layers without mirror domains.

(2) Growth of different types of semiconductor materials:

- In this dissertation, ZnO and GaN was grown on h-BN layers to seek the feasibility of the h-BN based hybrids. As a result, functional electronic and optoelectronic devices were fabricated using ZnO/h-BN or GaN/h-BN. However, there is still a lot of material combinations and many types devices which were not tried yet. For example, narrow band-gap materials such as InAs or GaAs are one of the good candidate which can show synergetic effect with h-BN. Growth mechanisms and structural properties would be carried out first as a fundamental research. By utilizing the narrow band-gap, the heterostructure can be fabricated into solar-cell or infra-red (IR) ranged optoelectronics.

(3) Optimization of ZnO nanotube VFET on graphene layers:

- Despite the successful fabrication of flexible VFET using ZnO/graphene, which showed that high quality inorganic electronics can be integrated with flexible form factor, several challenges related to the performance optimization remain. Currently, spin-coated polyimide is used as a gate dielectric layer. If proper ceramic dielectrics such as Al_2O_3 is employed, the performance will be greatly improved. Since the ZnO is vulnerable to the most of etchant, it is difficult to find way to selectively etch and open the tip of the ZnO nanotube channel, to fabricate the drain electrode.
- Another challenge is to form a good ohmic contact at the tip of the ZnO nanotube. While Ti/Au metal stack was used, which is typically used as an Ohmic electrode to ZnO, in the work the device exhibited a barrier at the drain electrode side. Therefore, the overall performance of the device is limited by the potential drop at the drain electrode. Further study on the process optimization such as plasma pre-treatment or additional thermal annealing would resolve the challenge.

References

- [1] J. A. Rogers, T. Someya, Y. Huang, *Science* (80-.). **2010**, DOI 10.1126/science.1182383.
- [2] K. K. Kim, A. Hsu, X. Jia, S. M. Kim, Y. Shi, M. Hofmann, D. Nezich, J. F. Rodriguez-Nieva, M. Dresselhaus, T. Palacios, J. Kong, *Nano Lett.* **2012**, DOI 10.1021/nl203249a.
- [3] Y. Shi, C. Hamsen, X. Jia, K. K. Kim, A. Reina, M. Hofmann, A. L. Hsu, K. Zhang, H. Li, Z. Y. Juang, M. S. Dresselhaus, L. J. Li, J. Kong, *Nano Lett.* **2010**, DOI 10.1021/nl1023707.
- [4] L. Song, L. Ci, H. Lu, P. B. Sorokin, C. Jin, J. Ni, A. G. Kvashnin, D. G. Kvashnin, J. Lou, B. I. Yakobson, P. M. Ajayan, *Nano Lett.* **2010**, DOI 10.1021/nl1022139.
- [5] Q. Wu, J. H. Park, S. Park, S. J. Jung, H. Suh, N. Park, W. Wongwiriyan, S. Lee, Y. H. Lee, Y. J. Song, *Sci. Rep.* **2015**, DOI 10.1038/srep16159.
- [6] J. H. Park, J. C. Park, S. J. Yun, H. Kim, D. H. Luong, S. M. Kim, S. H. Choi, W. Yang, J. Kong, K. K. Kim, Y. H. Lee, *ACS Nano* **2014**, DOI 10.1021/nn503140y.
- [7] L. Wang, B. Wu, J. Chen, H. Liu, P. Hu, Y. Liu, *Adv. Mater.* **2014**, DOI 10.1002/adma.201304937.
- [8] G. Lu, T. Wu, Q. Yuan, H. Wang, H. Wang, F. Ding, X. Xie, M. Jiang, *Nat. Commun.* **2015**, DOI 10.1038/ncomms7160.
- [9] R. Y. Tay, M. H. Griep, G. Mallick, S. H. Tsang, R. S. Singh, T. Tumlin, E. H. T. Teo, S. P. Karna, *Nano Lett.* **2014**, DOI 10.1021/nl404207f.
- [10] W. Auwärter, H. U. Suter, H. Sachdev, T. Greber, *Chem. Mater.* **2004**, DOI 10.1021/cm034805s.

- [11] A. Goriachko, H. Over, *Zeitschrift fur Phys. Chemie* **2009**, DOI 10.1524/zpch.2009.6030.
- [12] L. Gao, W. Ren, H. Xu, L. Jin, Z. Wang, T. Ma, L. P. Ma, Z. Zhang, Q. Fu, L. M. Peng, X. Bao, H. M. Cheng, *Nat. Commun.* **2012**, DOI 10.1038/ncomms1702.
- [13] G. Kim, A. R. Jang, H. Y. Jeong, Z. Lee, D. J. Kang, H. S. Shin, *Nano Lett.* **2013**, DOI 10.1021/nl400559s.
- [14] Y.-J. Kim, J.-H. Lee, G.-C. Yi, *Appl. Phys. Lett.* **2009**, DOI 10.1063/1.3266836.
- [15] Y. J. Hong, T. Fukui, *ACS Nano* **2011**, DOI 10.1021/nn2025786.
- [16] Y. Tchoe, J. Jo, M. Kim, G.-C. Yi, *NPG Asia Mater.* **2015**, DOI 10.1038/am.2015.88.
- [17] Y. J. Hong, W. H. Lee, Y. Wu, R. S. Ruoff, T. Fukui, *Nano Lett.* **2012**, DOI 10.1021/nl204109t.
- [18] Y. J. Kim, H. Yoo, C. H. Lee, J. B. Park, H. Baek, M. Kim, G. C. Yi, *Adv. Mater.* **2012**, DOI 10.1002/adma.201201966.
- [19] J. B. Park, H. Oh, J. Park, N. J. Kim, H. Yoon, G. C. Yi, *APL Mater.* **2016**, DOI 10.1063/1.4964490.
- [20] K. Chung, C. H. Lee, G. C. Yi, *Science (80-.)*. **2010**, DOI 10.1126/science.1195403.
- [21] H. Yoo, K. Chung, Y. S. Choi, C. S. Kang, K. H. Oh, M. Kim, G. C. Yi, *Adv. Mater.* **2012**, DOI 10.1002/adma.201103829.
- [22] K. Chung, S. In Park, H. Baek, J.-S. Chung, G.-C. Yi, *NPG Asia Mater.* **2012**, DOI 10.1038/am.2012.45.
- [23] H. Yoo, K. Chung, S. In Park, M. Kim, G. C. Yi, *Appl. Phys. Lett.* **2013**, DOI 10.1063/1.4790385.

- [24] Y. Kobayashi, K. Kumakura, T. Akasaka, T. Makimoto, *Nature* **2012**, DOI 10.1038/nature10970.
- [25] J. Y. Park, G. H. Lee, J. Jo, A. K. Cheng, H. Yoon, K. Watanabe, T. Taniguchi, M. Kim, P. Kim, G. C. Yi, *2D Mater.* **2016**, DOI Artn 035029r10.1088/2053-1583/3/3/035029.
- [26] C. H. Lee, T. Schiros, E. J. G. Santos, B. Kim, K. G. Yager, S. J. Kang, S. Lee, J. Yu, K. Watanabe, T. Taniguchi, J. Hone, E. Kaxiras, C. Nuckolls, P. Kim, *Adv. Mater.* **2014**, DOI 10.1002/adma.201304973.
- [27] P. K. Mohseni, A. Behnam, J. D. Wood, X. Zhao, K. J. Yu, N. C. Wang, A. Rockett, J. A. Rogers, J. W. Lyding, E. Pop, X. Li, *Adv. Mater.* **2014**, DOI 10.1002/adma.201305909.
- [28] G. Kresse, J. Furthmüller, *Comput. Mater. Sci.* **1996**, DOI 10.1016/0927-0256(96)00008-0.
- [29] J. P. Perdew, K. Burke, M. Ernzerhof, *Phys. Rev. Lett.* **1996**, DOI 10.1103/PhysRevLett.77.3865.
- [30] S. Grimme, *J. Comput. Chem.* **2006**, DOI 10.1002/jcc.20495.
- [31] K. Watanabe, T. Taniguchi, H. Kanda, *Nat. Mater.* **2004**, DOI 10.1038/nmat1134.
- [32] I. Jo, M. T. Pettes, J. Kim, K. Watanabe, T. Taniguchi, Z. Yao, L. Shi, *Nano Lett.* **2013**, DOI 10.1021/nl304060g.
- [33] A. Pakdel, Y. Bando, D. Golberg, *Chem. Soc. Rev.* **2014**, DOI 10.1039/c3cs60260e.
- [34] G.-H. Lee, Y.-J. Yu, X. Cui, N. Petrone, C.-H. Lee, M. S. Choi, D.-Y. Lee, C. Lee, W. J. Yoo, K. Watanabe, T. Taniguchi, C. Nuckolls, P. Kim, J. Hone, *ACS Nano* **2013**, DOI 10.1021/nn402954e.
- [35] H. Oh, Y. J. Hong, K. S. Kim, S. Yoon, H. Baek, S. H. Kang, Y. K. Kwon, M. Kim, G. C. Yi, *NPG Asia Mater.* **2014**, DOI 10.1038/am.2014.108.

- [36] N. Petrone, T. Chari, I. Meric, L. Wang, K. L. Shepard, J. Hone, *ACS Nano* **2015**, DOI 10.1021/acsnano.5b02816.
- [37] Y. Liu, X. Zou, B. I. Yakobson, *ACS Nano* **2012**, DOI 10.1021/nn302099q.
- [38] Z. Wang, *J. Nanoparticle Res.* **2012**, DOI 10.1007/s11051-012-0756-1.
- [39] N. Ding, C.-M. L. Wu, H. Li, *Phys. Chem. Chem. Phys.* **2014**, DOI 10.1039/c4cp02521k.
- [40] Q. Li, X. Zou, M. Liu, J. Sun, Y. Gao, Y. Qi, X. Zhou, B. I. Yakobson, Y. Zhang, Z. Liu, *Nano Lett.* **2015**, DOI 10.1021/acs.nanolett.5b01852.
- [41] L. Brown, E. B. Lochocki, J. Avila, C. J. Kim, Y. Ogawa, R. W. Havener, D. K. Kim, E. J. Monkman, D. E. Shai, H. I. Wei, M. P. Levendorf, M. Asensio, K. M. Shen, J. Park, *Nano Lett.* **2014**, DOI 10.1021/nl502445j.
- [42] W. Auwärter, M. Muntwiler, J. Osterwalder, T. Greber, *Surf. Sci.* **2003**, DOI 10.1016/j.susc.2003.08.046.
- [43] C. Oshima, A. Itoh, E. Rokuta, T. Tanaka, K. Yamashita, T. Sakurai, *Solid State Commun.* **2000**, DOI 10.1016/S0038-1098(00)00268-4.
- [44] Y. Wang, Y. Zheng, X. Xu, E. Dubuisson, Q. Bao, J. Lu, K. P. Loh, *ACS Nano* **2011**, DOI 10.1021/nn203700w.
- [45] K. K. Kim, A. Hsu, X. Jia, S. M. Kim, Y. Shi, M. Dresselhaus, T. Palacios, J. Kong, *ACS Nano* **2012**, DOI 10.1021/nn301675f.
- [46] Y. H. Lee, K. K. Liu, A. Y. Lu, C. Y. Wu, C. Te Lin, W. Zhang, C. Y. Su, C. L. Hsu, T. W. Lin, K. H. Wei, Y. Shi, L. J. Li, *RSC Adv.* **2012**, DOI 10.1039/c1ra00703c.
- [47] H. Cho, S. Park, D. Il Won, S. O. Kang, S. S. Pyo, D. I. Kim, S. M. Kim, H. C. Kim, M. J. Kim, *Sci. Rep.* **2015**, DOI 10.1038/srep11985.
- [48] S. M. Kim, A. Hsu, M. H. Park, S. H. Chae, S. J. Yun, J. S. Lee, D. H. Cho, W. Fang, C. Lee, T. Palacios, M. Dresselhaus, K. K. Kim, Y. H. Lee, J. Kong,

Nat. Commun. **2015**, DOI 10.1038/ncomms9662.

- [49] W. Auwärter, T. J. Kreuz, T. Greber, J. Osterwalder, *Surf. Sci.* **1999**, DOI 10.1016/S0039-6028(99)00381-7.
- [50] Z. Yan, J. Lin, Z. Peng, Z. Sun, Y. Zhu, L. Li, C. Xiang, E. L. Samuel, C. Kittrell, J. M. Tour, *ACS Nano* **2012**, DOI 10.1021/nm303352k.
- [51] R. Galand, G. Brunetti, L. Arnaud, J. L. Rouvière, L. Clément, P. Waltz, Y. Wouters, in *Microelectron. Eng.*, **2013**.
- [52] Y. Xue, Q. Liu, G. He, K. Xu, L. Jiang, X. Hu, J. Hu, *Nanoscale Res. Lett.* **2013**, DOI 10.1186/1556-276X-8-49.
- [53] R. V. Gorbachev, I. Riaz, R. R. Nair, R. Jalil, L. Britnell, B. D. Belle, E. W. Hill, K. S. Novoselov, K. Watanabe, T. Taniguchi, A. K. Geim, P. Blake, *Small* **2011**, DOI 10.1002/sml.201001628.
- [54] X. Blase, A. Rubio, S. G. Louie, M. L. Cohen, *Phys. Rev. B* **1995**, DOI 10.1103/PhysRevB.51.6868.
- [55] H. Peng, W. Dang, J. Cao, Y. Chen, D. Wu, W. Zheng, H. Li, Z. X. Shen, Z. Liu, *Nat. Chem.* **2012**, DOI 10.1038/nchem.1277.
- [56] C. H. Lee, Y. J. Kim, Y. J. Hong, S. R. Jeon, S. Bae, B. H. Hong, G. C. Yi, *Adv. Mater.* **2011**, DOI 10.1002/adma.201102407.
- [57] D. Choi, M. Y. Choi, W. M. Choi, H. J. Shin, H. K. Park, J. K. Seo, J. Park, S. M. Yoon, S. Chae, Y. H. Lee, S. W. Kim, J. Y. Choi, S. Y. Lee, J. M. Kim, *Adv. Mater.* **2010**, DOI 10.1002/adma.200903815.
- [58] M. Osada, T. Sasaki, *Adv. Mater.* **2012**, DOI 10.1002/adma.201103241.
- [59] S. Z. Butler, S. M. Hollen, L. Cao, Y. Cui, J. A. Gupta, H. R. Gutiérrez, T. F. Heinz, S. S. Hong, J. Huang, A. F. Ismach, E. Johnston-Halperin, M. Kuno, V. V. Plashnitsa, R. D. Robinson, R. S. Ruoff, S. Salahuddin, J. Shan, L. Shi, M. G. Spencer, M. Terrones, W. Windl, J. E. Goldberger, *ACS Nano* **2013**, DOI 10.1021/nm400280c.

- [60] C. R. Dean, A. F. Young, I. Meric, C. Lee, L. Wang, S. Sorgenfrei, K. Watanabe, T. Taniguchi, P. Kim, K. L. Shepard, J. Hone, *Nat. Nanotechnol.* **2010**, DOI 10.1038/nnano.2010.172.
- [61] H. Wang, T. Taychatanapat, A. Hsu, K. Watanabe, T. Taniguchi, P. Jarillo-Herrero, T. Palacios, *IEEE Electron Device Lett.* **2011**, DOI 10.1109/LED.2011.2160611.
- [62] Y. Gong, G. Shi, Z. Zhang, W. Zhou, J. Jung, W. Gao, L. Ma, Y. Yang, S. Yang, G. You, R. Vajtai, Q. Xu, A. H. Macdonald, B. I. Yakobson, J. Lou, Z. Liu, P. M. Ajayan, *Nat. Commun.* **2014**, DOI 10.1038/ncomms4193.
- [63] M. P. Levendorf, C. J. Kim, L. Brown, P. Y. Huang, R. W. Havener, D. A. Muller, J. Park, *Nature* **2012**, DOI 10.1038/nature11408.
- [64] A. Koma, *J. Cryst. Growth* **1999**, DOI 10.1016/S0022-0248(98)01329-3.
- [65] M. I. B. Utama, Z. Peng, R. Chen, B. Peng, X. Xu, Y. Dong, L. M. Wong, S. Wang, H. Sun, Q. Xiong, *Nano Lett.* **2011**, DOI 10.1021/nl1034495.
- [66] Y. J. Hong, J. W. Yang, W. H. Lee, R. S. Ruoff, K. S. Kim, T. Fukui, *Adv. Mater.* **2013**, DOI 10.1002/adma.201302312.
- [67] M. I. B. Utama, F. J. Belarre, C. Magen, B. Peng, J. Arbiol, Q. Xiong, *Nano Lett.* **2012**, DOI 10.1021/nl300554t.
- [68] Y. Zhu, Y. Zhou, M. I. Bakti Utama, M. D. La Mata, Y. Zhao, Q. Zhang, B. Peng, C. Magen, J. Arbiol, Q. Xiong, *Nanoscale* **2013**, DOI 10.1039/c3nr01984e.
- [69] K. Tomioka, M. Yoshimura, T. Fukui, *Nature* **2012**, DOI 10.1038/nature11293.
- [70] J. Wallentin, N. Anttu, D. Asoli, M. Huffman, I. Åberg, M. H. Magnusson, G. Siefer, P. Fuss-Kailuweit, F. Dimroth, B. Witzigmann, H. Q. Xu, L. Samuelson, K. Deppert, M. T. Borgström, *Science (80-.)*. **2013**, DOI 10.1126/science.1230969.
- [71] P. Das Kanungo, H. Schmid, M. T. Björk, L. M. Gignac, C. Breslin, J. Bruley,

- C. D. Bessire, H. Riel, *Nanotechnology* **2013**, DOI 10.1088/0957-4484/24/22/225304.
- [72] X. Dai, B. M. Nguyen, Y. Hwang, C. Soci, S. A. Dayeh, *Adv. Funct. Mater.* **2014**, DOI 10.1002/adfm.201400105.
- [73] Y. J. Hong, C. H. Lee, A. Yoon, M. Kim, H. K. Seong, H. J. Chung, C. Sone, Y. J. Park, G. C. Yi, *Adv. Mater.* **2011**, DOI 10.1002/adma.201100806.
- [74] F. A. Ponce, J. S. Major, W. E. Plano, D. F. Welch, *Appl. Phys. Lett.* **1994**, DOI 10.1063/1.112724.
- [75] N. Grandjean, J. Massies, P. Vennéguès, M. Laügt, M. Leroux, *Appl. Phys. Lett.* **1997**, DOI 10.1063/1.118205.
- [76] J. Narayan, K. Dovidenko, A. K. Sharma, S. Oktyabrsky, *J. Appl. Phys.* **1998**, DOI 10.1063/1.368440.
- [77] A. M. Munshi, D. L. Dheeraj, V. T. Fauske, D. C. Kim, A. T. J. Van Helvoort, B. O. Fimland, H. Weman, *Nano Lett.* **2012**, DOI 10.1021/nl3018115.
- [78] J. Wallentin, D. Kriegner, J. Stangl, M. T. Borgström, *Nano Lett.* **2014**, DOI 10.1021/nl403411w.
- [79] A. B. Djurišić, Y. H. Leung, A. B. Djurišić, Y. H. Leung, *Small* **2006**, DOI 10.1002/smll.200600134.
- [80] W. Il Park, G. C. Yi, M. Kim, S. J. Pennycook, *Adv. Mater.* **2002**, DOI 10.1002/adma.200290015.
- [81] X. Wang, S. Yang, J. Wang, M. Li, X. Jiang, G. Du, X. Liu, R. P. H. Chang, *J. Cryst. Growth* **2001**, DOI 10.1016/S0022-0248(01)01367-7.
- [82] S. Kim, H. Park, G. Nam, H. Yoon, J. S. Kim, J. S. Kim, J. S. Son, S. H. Lee, J. Y. Leem, *Bull. Korean Chem. Soc.* **2013**, DOI 10.5012/bkcs.2013.34.11.3335.
- [83] O. Pierre-Louis, M. R. D'Orsogna, T. L. Einstein, *Phys. Rev. Lett.* **1999**, DOI

10.1103/PhysRevLett.82.3661.

- [84] O. Trushin, K. Kokko, P. Salo, *Phys. Rev. B - Condens. Matter Mater. Phys.* **1997**, DOI 10.1103/PhysRevB.56.12135.
- [85] Y. J. Hong, H. S. Jung, J. Yoo, Y. J. Kim, C. H. Lee, M. Kim, G. C. Yi, *Adv. Mater.* **2009**, DOI 10.1002/adma.200703168.
- [86] H. Li, J. Cao, W. Zheng, Y. Chen, D. Wu, W. Dang, K. Wang, H. Peng, Z. Liu, *J. Am. Chem. Soc.* **2012**, DOI 10.1021/ja3021395.
- [87] M. Lin, D. Wu, Y. Zhou, W. Huang, W. Jiang, W. Zheng, S. Zhao, C. Jin, Y. Guo, H. Peng, Z. Liu, *J. Am. Chem. Soc.* **2013**, DOI 10.1021/ja406351u.
- [88] K. Chung, H. Oh, J. Jo, K. Lee, M. Kim, G.-C. Yi, *NPG Asia Mater.* **2017**, DOI 10.1038/am.2017.118.
- [89] *Nature* **1963**, DOI 10.1038/197438d0.
- [90] J. L. Rouvière, M. Arlery, B. Daudin, G. Feuillet, O. Briot, *Mater. Sci. Eng. B50* **1997**, DOI 10.1016/S0921-5107(97)00169-4.
- [91] D. M. Follstaedt, N. A. Missert, D. D. Koleske, C. C. Mitchell, K. C. Cross, *Appl. Phys. Lett.* **2003**, DOI 10.1063/1.1632540.
- [92] I. C. Kizilyalli, P. Bui-Quang, D. Disney, H. Bhatia, O. Aktas, *Microelectron. Reliab.* **2015**, DOI 10.1016/j.microrel.2015.07.012.
- [93] M. Liang, G. Wang, H. Li, Z. Li, R. Yao, B. Wang, P. Li, J. Li, X. Yi, J. Wang, J. Li, *J. Semicond.* **2012**, DOI 10.1088/1674-4926/33/11/113002.
- [94] H. Hirayama, S. Fujikawa, J. Norimatsu, T. Takano, K. Tsubaki, N. Kamata, *Phys. Status Solidi Curr. Top. Solid State Phys.* **2009**, DOI 10.1002/pssc.200880958.
- [95] Z. Fan, H. Razavi, J. W. Do, A. Moriwaki, O. Ergen, Y. L. Chueh, P. W. Leu, J. C. Ho, T. Takahashi, L. A. Reichertz, S. Neale, K. Yu, M. Wu, J. W. Ager, A. Javey, *Nat. Mater.* **2009**, DOI 10.1038/nmat2493.

- [96] G. Gustafsson, Y. Cao, G. M. Treacy, F. Klavetter, N. Colaneri, a J. Heeger, *Nature* **1992**, DOI Doi 10.1038/357477a0.
- [97] K. D. Harris, A. L. Elias, H. J. Chung, *J. Mater. Sci.* **2016**, DOI 10.1007/s10853-015-9643-3.
- [98] K. Nomura, H. Ohta, A. Takagi, T. Kamiya, M. Hirano, H. Hosono, *Nature* **2004**, DOI 10.1038/nature03090.
- [99] A. Carlson, A. M. Bowen, Y. Huang, R. G. Nuzzo, J. A. Rogers, *Adv. Mater.* **2012**, DOI 10.1002/adma.201201386.
- [100] M. K. Kelly, O. Ambacher, B. Dahlheimer, G. Groos, R. Dimitrov, H. Angerer, M. Stutzmann, *Appl. Phys. Lett.* **1996**, DOI 10.1063/1.117473.
- [101] E. Yablonovitch, T. Gmitter, J. P. Harbison, R. Bhat, *Appl. Phys. Lett.* **1987**, DOI 10.1063/1.98946.
- [102] H. Baek, J. B. Park, J. W. Park, J. K. Hyun, H. Yoon, H. Oh, J. Yoon, *Appl. Phys. Lett.* **2016**, DOI 10.1063/1.4954798.
- [103] K. Chung, H. Yoo, J. K. Hyun, H. Oh, Y. Tchoe, K. Lee, H. Baek, M. Kim, G. C. Yi, *Adv. Mater.* **2016**, DOI 10.1002/adma.201601894.
- [104] C.-H. Lee, G.-C. Yi, Y. M. Zuev, P. Kim, *Appl. Phys. Lett.* **2009**, DOI 10.1063/1.3067868.
- [105] S. R. Forrest, *Nature* **2004**, DOI 10.1038/nature02498.
- [106] T. Sekitani, U. Zschieschang, H. Klauk, T. Someya, *Nat. Mater.* **2010**, DOI 10.1038/nmat2896.
- [107] W. Il Park, J. S. Kim, G.-C. Yi, M. H. Bae, H.-J. Lee, *Appl. Phys. Lett.* **2004**, DOI 10.1063/1.1821648.
- [108] T. Bryllert, L. E. Wernersson, L. E. Fröberg, L. Samuelson, *IEEE Electron Device Lett.* **2006**, DOI 10.1109/LED.2006.873371.

- [109] K. Tomioka, J. Motohisa, S. Hara, T. Fukui, *Nano Lett.* **2008**, DOI 10.1021/nl802398j.
- [110] H. T. Ng, J. Han, T. Yamada, P. Nguyen, Y. P. Chen, M. Meyyappan, *Nano Lett.* **2004**, DOI 10.1021/nl049461z.
- [111] Q. Gao, D. Saxena, F. Wang, L. Fu, S. Mokkaapati, Y. Guo, L. Li, J. Wong-Leung, P. Caroff, H. H. Tan, C. Jagadish, *Nano Lett.* **2014**, DOI 10.1021/nl5021409.
- [112] X. Li, W. Cai, J. An, S. Kim, J. Nah, D. Yang, R. Piner, A. Velamakanni, I. Jung, E. Tutuc, S. K. Banerjee, L. Colombo, R. S. Ruoff, *Science (80-.)*. **2009**, DOI 10.1126/science.1171245.
- [113] K. S. Kim, Y. Zhao, H. Jang, S. Y. Lee, J. M. Kim, J.-H. Ahn, P. Kim, J.-Y. Choi, B. H. Hong, *Nature* **2009**, DOI 10.1038/nature07719.
- [114] Y. W. Heo, L. C. Tien, Y. Kwon, D. P. Norton, S. J. Pearton, B. S. Kang, F. Ren, *Appl. Phys. Lett.* **2004**, DOI 10.1063/1.1794351.
- [115] D. P. Norton, Y. W. Heo, M. P. Ivill, K. Ip, S. J. Pearton, M. F. Chisholm, T. Steiner, *Mater. Today* **2004**, DOI 10.1016/S1369-7021(04)00287-1.
- [116] C. Jagadish, S. Pearton, *Zinc Oxide Bulk, Thin Films and Nanostructures*, **2006**.
- [117] Y. Liu, N. O. Weiss, X. Duan, H.-C. Cheng, Y. Huang, X. Duan, *Nat. Rev. Mater.* **2016**, DOI 10.1038/natrevmats.2016.42.
- [118] K. S. Novoselov, A. Mishchenko, A. Carvalho, A. H. Castro Neto, *Science (80-.)*. **2016**, DOI 10.1126/science.aac9439.
- [119] Z. Lin, A. McCreary, N. Briggs, S. Subramanian, K. Zhang, Y. Sun, X. Li, N. J. Borys, H. Yuan, S. K. Fullerton-Shirey, A. Chernikov, H. Zhao, S. McDonnell, A. M. Lindenberg, K. Xiao, B. J. Le Roy, M. Drndić, J. C. M. Hwang, J. Park, M. Chhowalla, R. E. Schaak, A. Javey, M. C. Hersam, J. Robinson, M. Terrones, in *2D Mater.*, **2016**.
- [120] J. Lee, J.-H. Shin, G.-H. Lee, C.-H. Lee, *Nanomaterials* **2016**, DOI

10.3390/nano6110193.

- [121] Q. Li, M. Liu, Y. Zhang, Z. Liu, *Small* **2016**, DOI 10.1002/sml.201501766.
- [122] Z. Liu, L. Song, S. Zhao, J. Huang, L. Ma, J. Zhang, J. Lou, P. M. Ajayan, *Nano Lett.* **2011**, DOI 10.1021/nl200464j.
- [123] Y. B. Zhang, Y. W. Tan, H. L. Stormer, P. Kim, *Nature* **2005**, DOI 10.1038/nature04235.
- [124] J. H. Lee, E. K. Lee, W. J. Joo, Y. Jang, B. S. Kim, J. Y. Lim, S. H. Choi, S. J. Ahn, J. R. Ahn, M. H. Park, C. W. Yang, B. L. Choi, S. W. Hwang, D. Whang, *Science (80-.)*. **2014**, DOI 10.1126/science.1252268.
- [125] Y.-J. Kim, Y. Kim, K. Novoselov, B. H. Hong, *2D Mater.* **2015**, DOI 10.1088/2053-1583/2/4/042001.
- [126] R. Dahal, J. Li, S. Majety, B. N. Pantha, X. K. Cao, J. Y. Lin, H. X. Jiang, *Appl. Phys. Lett.* **2011**, DOI 10.1063/1.3593958.
- [127] A. R. Jang, S. Hong, C. Hyun, S. I. Yoon, G. Kim, H. Y. Jeong, T. J. Shin, S. O. Park, K. Wong, S. K. Kwak, N. Park, K. Yu, E. Choi, A. Mishchenko, F. Withers, K. S. Novoselov, H. Lim, H. S. Shin, *Nano Lett.* **2016**, DOI 10.1021/acs.nanolett.6b01051.
- [128] Z. Liu, L. Ma, G. Shi, W. Zhou, Y. Gong, S. Lei, X. Yang, J. Zhang, J. Yu, K. P. Hackenberg, A. Babakhani, J. C. Idrobo, R. Vajtai, J. Lou, P. M. Ajayan, *Nat. Nanotechnol.* **2013**, DOI 10.1038/nnano.2012.256.
- [129] Y. J. Shin, Y. Wang, H. Huang, G. Kalon, A. T. S. Wee, Z. Shen, C. S. Bhatia, H. Yang, *Langmuir* **2010**, DOI 10.1021/la100231u.
- [130] M. M. Rozhavskaya, W. V. Lundin, S. I. Troshkov, A. F. Tsatsulnikov, V. G. Dubrovskii, *Phys. Status Solidi Appl. Mater. Sci.* **2015**, DOI 10.1002/pssa.201431912.
- [131] A. Tanaka, R. Chen, K. L. Jungjohann, S. A. Dayeh, *Sci. Rep.* **2015**, DOI 10.1038/srep17314.

- [132] A. Ismach, H. Chou, D. A. Ferrer, Y. Wu, S. McDonnell, H. C. Floresca, A. Covacevich, C. Pope, R. Piner, M. J. Kim, R. M. Wallace, L. Colombo, R. S. Ruoff, *ACS Nano* **2012**, DOI 10.1021/nn301940k.
- [133] M. Xu, D. Fujita, H. Chen, N. Hanagata, *Nanoscale* **2011**, DOI 10.1039/c1nr10294j.
- [134] C. Zhang, L. Fu, S. Zhao, Y. Zhou, H. Peng, Z. Liu, *Adv. Mater.* **2014**, DOI 10.1002/adma.201304301.
- [135] A. Gibaud, R. A. Cowley, D. F. McMorrow, R. C. C. Ward, M. R. Wells, *Phys. Rev. B* **1993**, DOI 10.1103/PhysRevB.48.14463.

Abstract (Korean)

국문요약문

층상구조를 갖는 2차원 나노소재는 원자 단위의 얇은 두께로 인해 투명, 유연할 뿐만 아니라 뛰어난 기계적 강도, 높은 열전도도, 물질에 따라 다양한 전기적 특성을 보이기 때문에 차세대 소재로 각광받고 있다. 반면, 2차원 나노소재는 도핑 후 전기적 성능이 현저히 저하되고, 두께에 따라 밴드갭이 변화하는 등의 한계를 보이고 있어 현재까지 층상구조 2차원 나노소재 만으로는 광/전자소자 제작에 어려움이 많다. 따라서 이러한 2차원 나노소재 위에 반도체 나노소재 기반 고효율 광전소자 제조 기술을 접목하여 복합차원 나노소재 및 이를 이용한 소자를 제조하면 2차원 소재의 유연하면서 강한 물리적 특성을 이용한 부드럽고 유연한 형태의 소자 제작이 용이하며, 2차원 소재의 독특한 전기적 성질을 기존의 반도체 나노소재와 결합하여 두 소재의 장점을 합친 새로운 기능성의 소자를 구현할 수 있다.

본 학위논문에서는 우수한 물리적 특성과 더불어 유연성, 투명성 등 다양한 기능성을 가지는 질화붕소 및 2차원 나노소재 상에, 고성능 소자의 기본 소재로 활용되는 무기 반도체를 결합한 복합 소재 및 이를 이용한 기능성 광/전자 소자의 제조를 다룬다.

먼저 대면적 질화붕소 기반 복합구조물 제조의 기본 연구로서, 센티미터 크기를 가지는 수 원자층 두께의 질화붕소 필름을 제조하였다. 본 연구에서는 상압화학기상증착법을 이용하여 단결정 금속인 Ni(111) 기판 위에 에피택셜 성장한 후, 전기화학적 방법으로 제조된 h-BN 필름을 임의의 기판으로 전사하는 한편 Ni(111) 기판을 재사용하였다. 방사광가속기를 이용한 X-선 산란 분석 및 투과전자현미경으로 분석한 결과 제조된 질화붕소 필름은 Ni(111)과 강한 에피택셜 관계를 가지고 있으며, 마이크로 미터 수준에서도 결정구조가 한 방향으로 정렬되어 있음을 확인할 수 있었다. 이와 같은 고품질의 질화붕소 필름을 제조하기 위해서는 전구체인 Ammonia-borane의 승화 온도를 조절하는 것이 매우 중요하였으며, 그 외 다양한 방법으로 질화붕소 특유의 물성 역시 확인할 수 있었다. 본 연구는 고품질의 절연성 2차원 나노소재를 대면적으로 제조/전사하는 방법을 제시하여 기존의 질화붕소 기반 광전소자 연구의 응용성을 크게 높일 수 있을 것으로 기대된다.

질화붕소 상 반도체 구조물의 형성 원리를 분석하기 위해, 고품위의 산화아연 나노구조물을 반데르발스 에피택시(van der Waals epitaxy) 방법으로 성장하고 그 특성을 분석하였다. 플라즈마를 이용한 기판 처리를 통하여 산화아연 나노막대 및 나노벽 구조물을 질화붕소층

위에 형성하였으며, 제조된 산화아연/질화붕소 이중구조의 구조적 특성을 전자투과현미경과 전산모사로 분석 및 검증하였다. 특히 플라즈마 처리로 산화아연 나노구조의 밀도가 조절됨을 이용하여 위치와 형상이 조절된 산화아연 나노구조물을 제조하는데 성공하였다. 한편, 질화붕소 기반 복합 구조물의 보다 넓은 활용 가능성을 알아보기 위해 반도체 소자에 널리 활용되는 박막 구조물(질화갈륨)을 대면적 질화붕소에 형성 후 그 결합구조를 분석하였다. 분석 결과 제조된 질화갈륨 박막의 결합 농도는 타 2차원 나노소재 상 혹은 실리콘 단결정(Si(111))위 형성된 박막과 비슷한 수준을 보여주어 향후 광전소자 및 전자소자로 활용이 가능함을 보여주었다.

질화붕소 기반 복합 구조물의 기능성을 보여주는 소자의 한 예시로 산화아연 나노구조물을 채널로 하는 대면적 산화아연/질화붕소 기반의 유연한 자외선 센서를 제조하였다. 광전류 측정을 통해 질화붕소가 기판으로 사용될 경우 그렇지 않은 경우에 비해 우수한 센서 특성을 보임을 확인하였다. 대면적 산화아연 나노구조물을 패터닝한 후 본래 기판에서 기계적으로 박리하여 유연성 자외선 소자를 제조할 수 있었으며, 제조된 소자는 다양한 굽힘 환경에서도 우수한 성능을 보여주었다. 이를 통해 질화붕소가 광전소자를 위한 기능성 기판으로 활용될 수 있음을 시연하였다.

질화붕소 기반의 복합구조물 및 이를 이용한 광전소자에서 나아가, 본 학위논문에서는 1차원 반도체 나노소재와 2차원 나노소재가 결합된 하이브리드 나노소재를 이용한 수직형 전계효과 트랜지스터(VFET)를 제조하고 그 특성을 분석하였다. 대면적으로 제조된 그래핀 필름 위 위치와 형상이 조절되어 성장된 단결정 산화아연 나노튜브를 채널로 이용하였으며, 그래핀 필름은 또한 산화아연 나노튜브의 소스 전극으로도 활용되었다. 단결정으로 성장된 산화아연 나노튜브의 우수한 물리적 특성과 수직형 소자구조가 가지고 있는 장점으로 말미암아, 제조된 VFET은 탁월한 전기적 특성을 보여주었다. 제조된 VFET의 sub-threshold swing은 110 mV/dec, 최대/최소 전류비는 10^6 , 상호컨덕턴스는 170 nS/um 으로, 이는 기존의 산화아연 나노소재 기반 VFET에 비해 우수한 것이다. 본 소자의 작동 메커니즘은 3차원 시뮬레이션을 이용하여 보다 자세히 분석되었다. 특히, 그래핀을 기판으로 사용하였기 때문에 제조된 소자를 기계적으로 박리 후 다른 임의의 기판에 전사하는 것이 가능하였다. 이를 이용하여 제조된 소자를 유연한 플라스틱 기판위에 전사한 후, 소자의 전기적 특성이 크게 변화하지 않음을 확인하여 향후 웨어러블 디바이스의 전자소자로 활용이 가능함을 입증하였다.

주요어: 질화붕소, 유연소자, 나노구조, 전자소자, 광전소자

학번: 2011-20409

Appendix.

Selective area heteroepitaxial growth of h-BN micropatterns on graphene layers

A.1. Introduction

Two-dimensional (2D) layers and their heterostructures have great potential for novel electronic and optoelectronic devices due to their remarkable physical properties and interesting behaviors^[117–122]. For example, graphene and hexagonal boron nitride (h-BN) are 2D materials that are highly conducting and insulating, respectively^[2,33,48,123–127]. Accordingly, these 2D nanomaterials have been used in transferable and flexible optoelectronic and electronic devices^[20,24,63,88,128]. Additionally, stacked heterostructures of h-BN and graphene have enabled the fabrication of high-performance electronic devices^[34,60]. Nevertheless, these stacked configurations are still limited by the ability to fabricate h-BN and graphene heterostructures at specific positions. It is crucial for this to be resolved to enable such heterostructures to be exploited as building blocks for fabricating integrated devices. Herein, we report selective-area heteroepitaxial growth of h-BN micropatterns on graphene for controlling the position of the heterostructure.

A.2. Selective growth of h-BN on micropatterned graphene layers

The strategy for the fabrication of position-controlled heterostructures is illustrated schematically in Figure A.1. Graphene layers used as the substrate were prepared by mechanical exfoliation and transferred onto SiO₂/Si substrates (Figure 1a). The inert graphene surface does not have chemical reactivity, which provides both challenges and opportunities for growing position-controlled h-BN micropatterns directly on graphene layers^[129]. To precisely localize the growth sites on the graphene layers without a catalyst, the FIB was applied only to specific regions and thermal annealing was carried out under an ammonia flow. Hexagonal-shaped micropatterns were clearly observed (Figure A.1b). The typical size and depth of the micropatterns were 300 and 40 nm, respectively (inset of Figure A.1b). Then, to grow h-BN on the micropatterns, borazine, ammonia, and nitrogen were introduced into the cold-wall CVD reactor in the absence of any metal catalyst film. Highly selective growth of micropatterns with flat surface morphology was achieved by optimizing the growth parameters (e.g., temperature, pressure and gas flow rate, not shown here). Field-emission scanning electron microscopy (FE-SEM) images (Figure A.1c and its inset) revealed regularly ordered h-BN micropatterns.

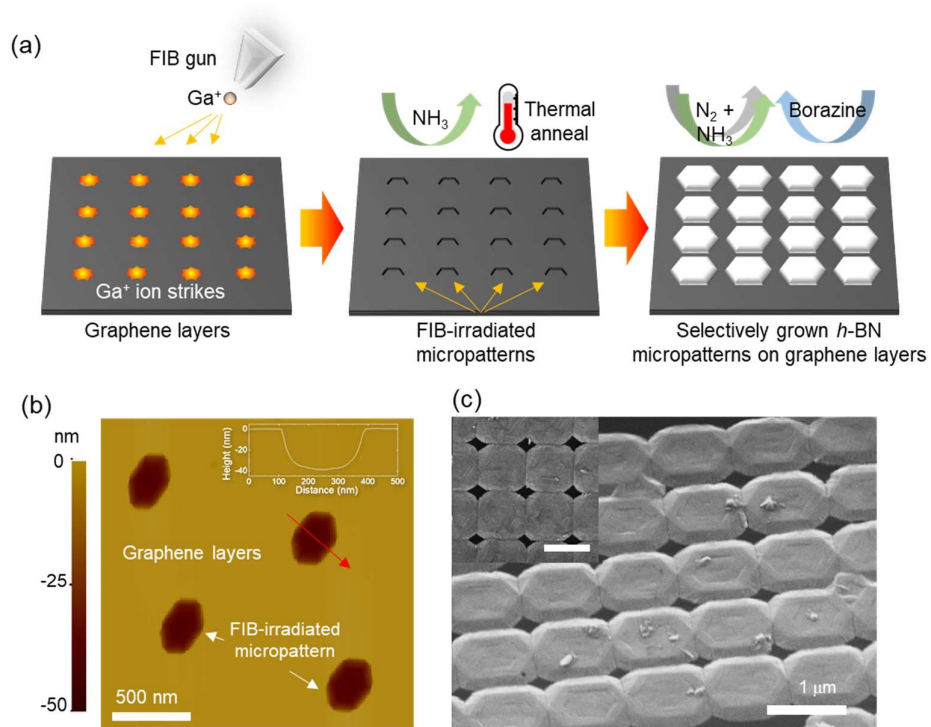


Figure A.1. (a) Schematic diagram of the process used to fabricate the position-controlled h-BN/graphene heterostructure. (b) Atomic force microscopy (AFM) topographic image and height profile (inset) of patterned graphene layers after focused ion beam (FIB) irradiation and thermal annealing in ammonia. (c) Tilt-view field-emission scanning electron microscopy (FE-SEM) image of selectively grown h-BN on the micropatterned graphene layers. Top-view FE-SEM image (inset) of the same.

A.3. Morphology of h-BN micropatterns on graphene layers

The morphology of the h-BN micropattern array was further investigated using AFM; the h-BN micropattern array had a hexagonal morphology (Figure A.2a). The hexagons were oriented parallel to each other, implying heteroepitaxial growth of *h*-BN on graphene, which will be discussed later. Note that the lateral size (1 μm) of the *h*-BN micropatterns was much greater than the size (0.3 μm) of the hexagonal FIB patterns formed on the graphene layers (marked by the red hexagon), indicating that lateral overgrowth occurred during the growth.

Figure A.2b presents the height profile of an h-BN micropattern. This profile reveals that the h-BN micropattern had a truncated hexagonal pyramid shape with a thickness of 50 nm. Interestingly, a slightly concave surface morphology was observed: its edges were 10 nm higher than its center. The concave profile can be described by the following^[130,131]:

$$\frac{H(x)}{H_{max}} = \frac{\sinh(R/\lambda) + (\lambda_0/\lambda) \cosh[(R-x)/\lambda]}{\sinh(R/\lambda) + (\lambda_0/\lambda) \cosh[R/\lambda]}, \quad (1)$$

where $H(x)$ is the height of the h-BN micropatterns with respect to the position, H_{max} is the maximum height of the micropattern at the edges, R is the radius of the micropattern, and λ and λ_0 are the diffusion lengths of the adatoms on the top surface and sidewall of the micropattern, respectively. Figure A.2b shows that the height profile of the h-BN micropattern was well fit with Eq. (1). From the

fitting curve, the diffusion length (200 nm) of h-BN adatoms was extracted. For simplicity, we assumed that the diffusion length at the top surface and sidewall were identical; *i.e.*, $\lambda = \lambda_0$.

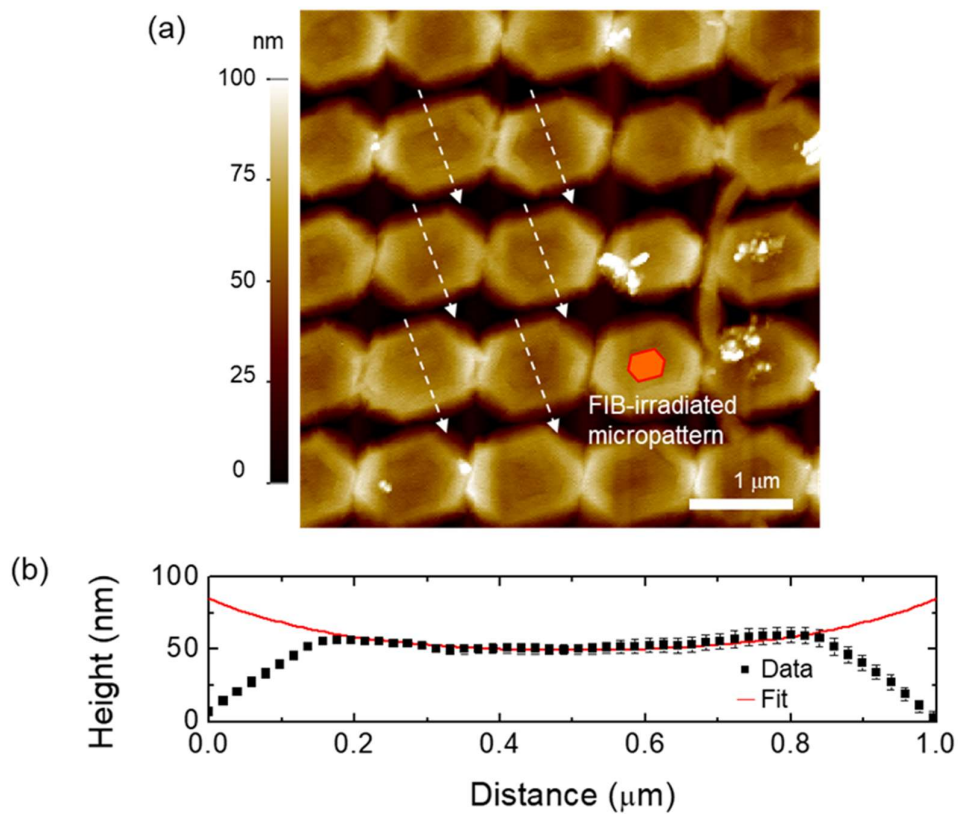


Figure A.2. (a) Surface topography of selectively formed *h*-BN investigated by atomic force microscopy (AFM). (b) The height profiles (black) and theoretical expectation of the surface profile with a diffusion length of 200 nm (red).

A.4. The growth scenario

We propose a growth scenario for the selective growth of h-BN micropatterns with concave surface morphology in terms of diffusion length. At the initial stage of growth, adatoms nucleate only on the FIB-irradiated micropatterns that presumably have step edges and defects; nucleation would not occur on a non-irradiated region of a pristine graphene surface (Figure A.3a). As the nuclei grow, they merge, forming a very thin, small h-BN micropattern (Figure A.3b). Once the h-BN micropattern forms, adatom diffusion occurs on the surface of the h-BN, as well as on the graphene. That is, the adatoms adsorbing on the surfaces of the h-BN micropattern and graphene can move freely and reach the edges, which increases the lateral size of the h-BN micropattern (Figure A.3c). Meanwhile, the micropattern enlarges vertically and laterally, yielding a truncated pyramid-shaped h-BN micropattern. When the lateral size of the h-BN micropattern is smaller than the surface diffusion length of adatoms on the micropattern, the h-BN micropattern has a nearly flat surface. However, as growth continues and when the size of the micropattern is greater than the surface diffusion length of the h-BN micropattern, adatoms adsorbed or located at the edge cannot reach the center of the micropattern. The greater incoming flux of atoms to the edge compared with that to the center results in the formation of a concave surface profile (Figure A.3d). This scenario suggests that diffusion of the adatoms plays a critical role in determining catalyst-

free growth, which is different from the catalyst-assisted growth of 2D materials on metal films where surface dissolution and segregation govern the growth^[132–134].

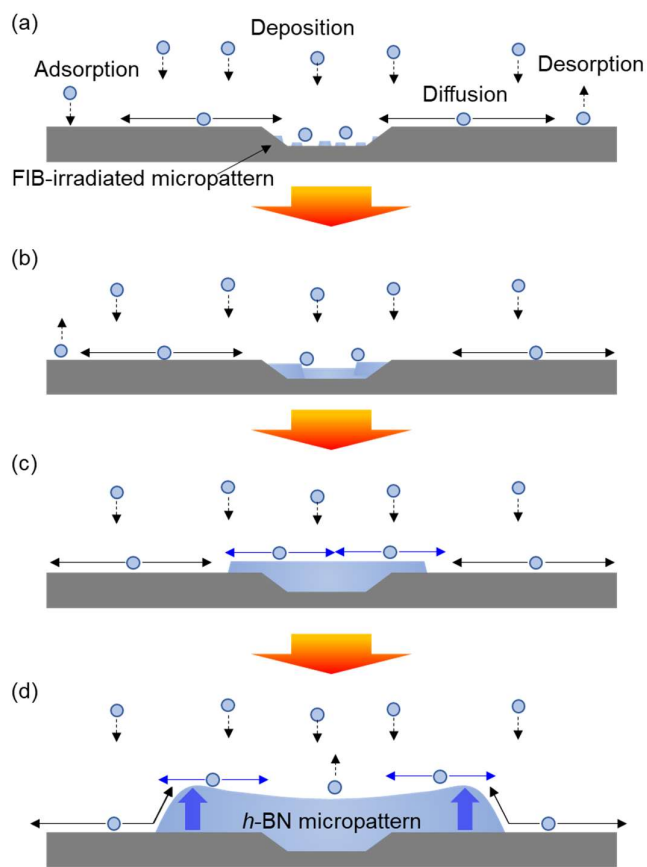


Figure A.3. Growth scenario of *h*-BN on focused ion beam (FIB)-patterned graphene layers, illustrating the mechanism of position-selective nucleation and side-wall thickening.

A.5. Structural properties of h-BN micropatterns on graphene layers

We used high-resolution SR-XRD to investigate the structural properties of h-BN grown on graphene. Figure A.4a shows the strong central diffraction peak and its satellite peaks that were observed in the θ - 2θ scan near the (0002) diffraction of h-BN grown on graphene layers. The uniformly separated satellite peaks resulted from Laue oscillations, which is a set of fringes resulting from the interference of Bragg reflections from coherently scattering lattice planes. The observation of Laue oscillations implies that the h-BN micropatterns consisted of coherently scattering crystalline layers with clean, smooth heterointerfaces^[135]. Because Laue oscillations result from Bragg reflections from coherently scattering lattice planes, the thicknesses of the h-BN layers contributing to the coherent scattering can be extracted from the curve. The thickness of h-BN estimated from the curve was 44 nm.

RSM using SR-XRD was used to investigate the detailed crystallographic structure of h-BN. Figure 4b presents an HL-mesh contour map around the (0002) diffraction of h-BN and graphene. The diffractions from $(0002)_{\text{h-BN}}$ and their satellite peaks (indicated by red arrows) are located along the constant $H = 0$ line, demonstrating that the c -axis of the h-BN was well oriented along the normal direction of the graphene surface. Additionally, the crystallinity of h-BN was investigated by measuring the full-width at half maximum (FWHM) of an h-BN

peak along the $Q_{//}$ direction. The second-order satellite peak of h-BN was used for this measurement because the (0002) diffraction of h-BN overlapped with diffraction from the (0002) plane of the graphene layers due to their similar lattice constants. As shown in the inset, the second-order satellite peak marked by the red arrow exhibited a small FWHM value of 0.00283 \AA^{-1} (or 0.0869°), indicating high h-BN crystallinity.

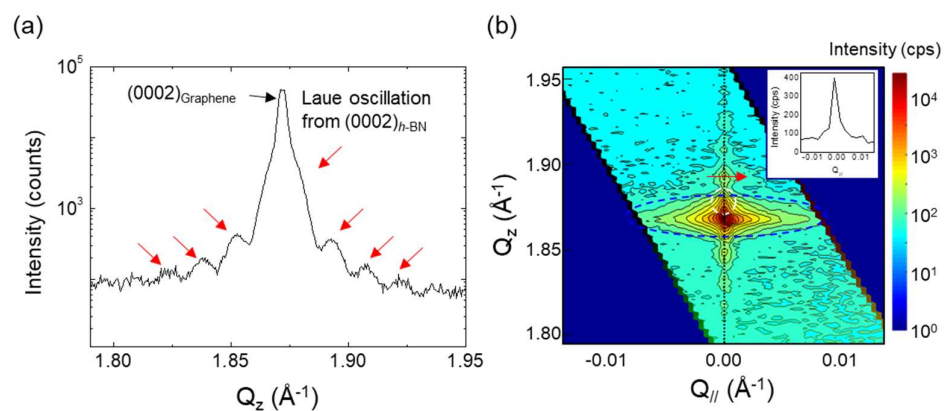


Figure A.4. High-resolution synchrotron radiation X-ray diffraction analysis (SR-XRD) of the selectively formed h-BN micropatterns on graphene layers. (a) θ - 2θ scan near the (0002) diffraction of h-BN on the graphene layers. (b) Reciprocal space mapping around the diffraction of $(0002)_{\text{h-BN}}$ and $(0002)_{\text{graphene}}$. The inset shows the detailed profile of the diffraction indicated by the red arrows.

The microstructural characteristics of the h-BN micropatterns and their heteroepitaxial relationship to the graphene layers were examined by TEM. The SAED pattern of the selectively grown h-BN micropattern is shown in the inset of Figure A.5a. Notably, each diffraction was resolved into two diffractions with slightly different lattice constants, along with two satellite peaks. The lattice spacings of h-BN and graphene corresponding to each diffraction were estimated at $d = 2.15$ and 2.11 Å from the $(10\bar{1}0)$ diffractions, and $d = 1.25$ and 1.22 Å from $(\bar{1}2\bar{1}0)$ diffractions, respectively. The calculated d -values are similar to those in the literature for h -BN and graphene, in which $d = 2.17$ and 2.13 Å for the $(10\bar{1}0)_{h\text{-BN}}$ and $(10\bar{1}0)_{\text{graphene}}$ planes, respectively, and $d = 1.25$ and 1.23 Å for the $(\bar{1}2\bar{1}0)_{h\text{-BN}}$ and $(\bar{1}2\bar{1}0)_{\text{graphene}}$ planes, respectively. The multiple spots in the SAED pattern indicated that the h-BN and graphene had the same crystallographic orientation, *i.e.*, $(10\bar{1}0)_{h\text{-BN}} \parallel (10\bar{1}0)_{\text{graphene}}$.

The interface between the h-BN and the graphene substrate was also investigated using cross-sectional TEM. Figure A.5b displays a bright field (BF) cross-sectional image of an edge part of an h-BN micropattern. The boundary of the h -BN micropattern and the interface between the h-BN and the graphene substrate are indicated by the blue and white dashed lines, respectively. High-resolution TEM (HR-TEM) (Figure A.5b) revealed a highly ordered atomic

arrangement at the h-BN region. Fast Fourier transform (FFT) images of the h-BN and graphene layers are shown in the inset, which detail their crystal structures. The clear spots along the vertical direction observed from the FFT image of the h-BN region resulted from a layered structure with a uniform interlayer distance and single orientation. The spot corresponds to the periodicity of the $(0002)_{\text{h-BN}}$ planes. The cross-sectional investigation indicated that both the h-BN and graphene layers had a layered structure with their c -axis directions parallel to each other and did not have differently oriented domains or amorphous regions.

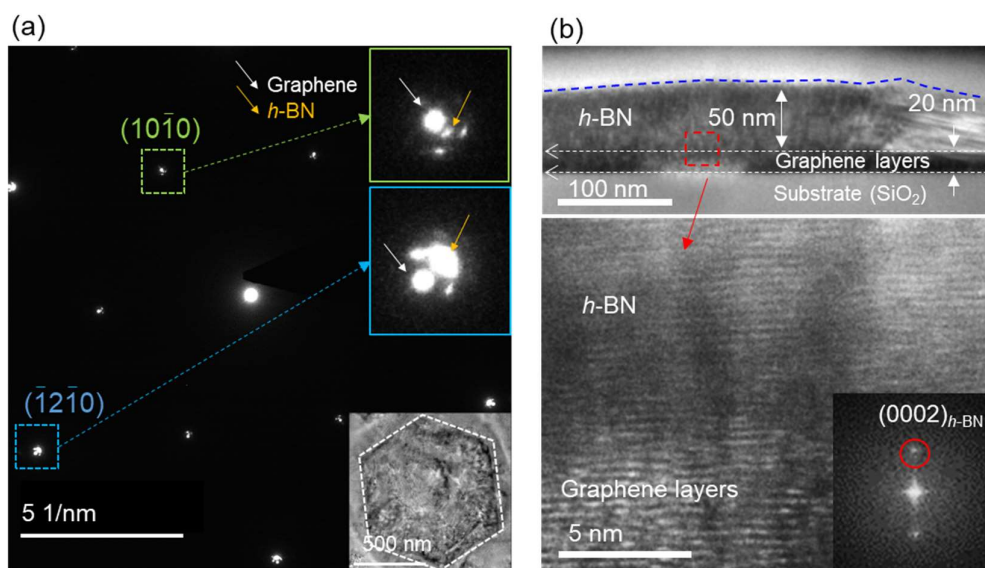


Figure A.5. Microstructural properties of h-BN selectively formed on graphene layers investigated by transmission electron microscopy (TEM). (a) Selective-area electron diffraction (SAED) patterns obtained from a single h-BN micropattern. Top and middle inset: Magnified images of diffraction from the $(10\bar{1}0)$ and $(\bar{1}2\bar{1}0)$ planes of h-BN and graphene. Bottom inset: Plan-view image of an h-BN micropattern on the graphene layers. (b) Cross-sectional image of h-BN/graphene and high-resolution TEM (HR-TEM) images of the enclosed area. Inset: Fast Fourier transform (FFT) images of h-BN.

A.6. Summary

Summarizing, position-controlled h-BN micropattern arrays were heteroepitaxially grown on graphene layers by FIB and catalyst-free CVD. High-quality, ultrathin h-BN micropattern arrays were selectively nucleated only on the FIB-irradiated micropatterns. The morphology and surface profile of the h-BN micropatterns strongly suggest that lateral overgrowth was dominant during the growth of the h-BN micropatterns. A scenario for the catalyst-free selective growth was also suggested in terms of a surface diffusion model of the adatoms. More importantly, both high-resolution SR-XRD and TEM analyses revealed the excellent crystalline quality of the h-BN micropatterns. In particular, RSM using high-resolution SR-XRD exhibited an extremely small FWHM value of 0.00283 \AA^{-1} (0.0869°) for the second-order satellite peak, which confirmed the excellent crystallinity of the h-BN micropatterns. Both high-resolution SR-XRD and TEM analyses also revealed that the h-BN micropatterns had the heteroepitaxial relationships of $(0002)_{\text{h-BN}} \parallel (0002)_{\text{graphene}}$ and $(10\bar{1}0)_{\text{h-BN}} \parallel (10\bar{1}0)_{\text{graphene}}$. More generally, we believe that the selective-area heteroepitaxial growth of h-BN on graphene using a FIB surface treatment could be readily expanded to create many other position-controlled 2D heterostructures.